AN ABSTRACT OF THE DISSERTATION OF

Jackson R. Harter for the degree of Doctor of Philosophy in Nuclear Engineering presented on October 29, 2019.
Title: Advanced Deterministic Phonon Transport Techniques for Predicting Spectral Thermal Conductivity in Homogeneous and Heterogeneous Media

Abstract approved: _____

Todd S. Palmer

We present a deterministic spectral method to predict equilibrium temperature distributions, heat flux, and thermal conductivity in homogeneous and heterogeneous media. We solve the Boltzmann transport equation in a second order spatial, self-adjoint angular flux formulation. We implemented this method into the radiation transport code Rattlesnake, built using the MOOSE (Multiphysics Object Oriented Simulation Environment) framework. The spatial variable is discretized using the continuous finite element method with unstructured meshes, and the angular variable is discretized with the discrete ordinates method.

We implemented the diffuse mismatch model in a general geometry to simulate phonon interfacial resistance, using the grey approximation of the Boltzmann transport equation. Using material properties generated by density functional theory and molecular dynamics methods, we were able to elucidate properties of xenon (Xe) at temperatures and pressures experienced in irradiated nuclear fuel. We found Xe to undergo phase change from liquid to solid, and were able to compute coefficients of phonon transmission and reflection at the Xe-UO_2 interface. We found κ to decrease by about a factor of 4 with increasing temperature, agreeing with other trends and research in the open literature.

We developed a new method for simulating deterministic, spectral phonon transport to predict heat flux, thermal conductivity, and equilibrium temperature distributions in homogeneous and heterogeneous materials. All the spectral phonon groups are coupled through a local average material temperature, and a new term, β, is derived and is used as a closure term in the phonon transport equation. β acts to redistribute the fraction of total energy which is exchanged between the transport system and equilibrium distribution of phonons. This method predicts thermal conductivity trends in materials spanning geometric domain sizes from nanometers to micrometers, and exhibits the correct asymptotic heat flux behavior as domain size increases. We observed β to be the most influential at smaller domain sizes, where equilibrium is difficult to establish due to the proximity of the boundary phonon sources; as domain size increased, β diminished in size, and nearly vanished at the maximum domain size of 10 μm. This further makes the case to perform BTE simulations for nanometer to micrometer heat transfer, as Fourier's law will not accurately capture the heat transfer in such small domain sizes, e.g., thermoelectric devices, heat transfer around defects and heterogeneities in reactor fuel. Additionally, we developed a novel material property discretization scheme which is consistent with the discretization of the angular variable in the transport equation.

We performed convergence studies to test the efficiency of the spectral method, which used a modified source iteration (MSI) to solve the linear system of equations. We compare the performance of traditional source iteration (SI) of the uncoupled self-adjoin angular flux method we previously implemented to the new method and comment on the iterative performance of each. We capture ballistic and diffusive phonon scattering, and are able to make comparisons between the accuracy and efficiency of both methods. We find that MSI outperforms SI in most cases,

especially as the spatial domain becomes acoustically thick.

Advanced Deterministic Phonon Transport Techniques for Predicting Spectral
Thermal Conductivity in Homogeneous and Heterogeneous Media

by

Jackson R. Harter

A DISSERTATION

submitted to

Oregon State University

in partial fulfillment of
the requirements for the
degree of

Doctor of Philosophy

Presented October 29, 2019
Commencement June 2020

Doctor of Philosophy dissertation of Jackson R. Harter presented on October 29, 2019.

APPROVED:

_____

Major Professor, representing Nuclear Engineering

_____

 Head of the School of Nuclear Science and Engineering

_____

Dean of the Graduate School

I understand that my dissertation will become part of the permanent collection of Oregon State University libraries. My signature below authorizes release of my dissertation to any reader upon request.

_____

Jackson R. Harter, Author

ACKNOWLEDGEMENTS

Anyone who knows me will realize that this part of my dissertation may be longer than the abstract. Also please know that even though I have a "major" and "minor" professor, the roles of these two individuals should be known as "co-advisors".

Thank you, Dr. Todd Palmer, for being an incredible advisor and mentor, but also a friend. Over our long history, I have wholeheartedly appreciated all the attention and care you have given me with both my professional work and personal life. Whether it was a chance encounter at a Steven Wilson concert and seeing your air guitar in action, or your critical reviews of my work and writing, please know your guidance has meant, and will continue to mean so much to me. I hope to continue to know you and collaborate with you for a long time to come.

Thank you, Dr. Alex Greaney. I realize this dissertation marks you as my "minor advisor", but without your leadership and attention, I would not have been successful in these endeavors. You helped unsheathe my interest in materials science and the associated physics; you are also a very talented cook and *gastronome*. Our discussions over the years have kept me accessing the parts of my past career life as a cook, and inspire me to keep cooking elaborately at home and for my friends. Part of the passion I felt for that industry is instilled in my work now, and for that I thank you.

I could not have made it this far without the support and encouragement from all of my family and friends. The community I was a part of at the Radiation Center these past 10 years has profoundly changed me; I would have never guessed that my life would take me down this path. I am both privileged and extremely lucky to have been in the right places at the right times, and applied the appropriate amount

of effort. It took me a longer time to learn my lessons than most, I attribute this to my refusal to grow up; this is the component of me that keeps asking questions and continues to bring new perspectives to established institutions. I look forward to every day of my life and what I can be a part of, and how I can help.

Rob, thanks for being a great friend to me. I really value our relationship and the advice you give, and the kindness you've extended me. Of all things in Corvallis, one of them I missed the most is being able to stop by your office for a chat about whatever, go to lunch, or out on some nighttime karaoke adventure ("Love Shack Baby").

Tony, I've appreciated being your friend and cohort. It meant a lot to have a good roommate and friend those summers in Idaho, when we were both far away from home. I'm glad we got the chance to practice some cooking together. Continue to work hard and keep in touch, and I'm glad you finally know what a phonon is.

And Doug, I sure miss your presence, you were a fantastic human being. I was looking forward to being your friend and colleague for the rest of my life, and I'm always going to think about that as I perform my own work and try to make a difference; just like you did.

Laura de Sousa Oliveira is an extremely talented computational scientist who I have had the good fortune to know as a friend and collaborator. She has persevered and flourished in the physics and engineering community, which has always been male-dominated with far too masculine a gender-culture. This culture needs to make way for people like her, and she is a role model and inspiration for me.

Thanks to the entire cohort of RTRP (Radiation Transport and Reactor Physics) over the years; I hope to see all of you doing great things! Thanks for your support for the Type 1 Diabetes walks we've had in Corvallis.

"You are never given a wish without also being given the power to make it true.

You may have to *work* for it, however." – Richard Bach

CONTRIBUTION OF AUTHORS

Dr. Laura de Sousa Oliveira prepared material properties of uranium dioxide for Chapter 3.

Dr. Agnieszka Truszkowska prepared molecular dynamics data for xenon at various temperature and pressure for Chapter 3.

Aria Hosseini prepared material property data using density functional theory simulations for Chapter 4.

TABLE OF CONTENTS

TABLE OF CONTENTS (Continued)

LIST OF FIGURES (Continued)

Advanced Deterministic Phonon Transport Techniques for Predicting Spectral Thermal Conductivity in Homogeneous and Heterogeneous Media

1   Introduction

1.1   Motivation

The advent of nuclear reactors signaled the beginning of a new era in the realms of power generation and scientific research. The prospect of a power source that can contribute vast quantities of baseload power while emitting no carbon or combustion byproducts, combined with safe, stable operation and minimal waste products is a technology worthy of much consideration and continuous research. Myriad complexities exist in nuclear power reactors and in the nuclear power cycle; heat generation through nuclear fission, heat transfer to coolant, circulation of this coolant around the reactor core, steam generation to drive turbines which produce electricity, and the massive equipment which drives these processes [4–7].

A critical element in the entire process of nuclear power generation is the mechanism of heat transfer from the nuclear fuel, which is typically uranium dioxide (UO_2) for all water-moderated nuclear reactors in the United States [8–10]. Heat must be dissipated from the fuel into the coolant, such that it can perform work and generate steam to drive the turbines. At the macroscopic scale, heat transfer through a surface can be expressed through the empirical law of Fourier [7, 11–14]:

$$\mathbf{q} = -\kappa \nabla T, \tag{1}$$

where $\mathbf{q}$ is heat flux in units of $W \cdot m^{-2}$, κ is thermal conductivity, a second order directionally dependent tensor, with units of $W \cdot m^{-1} \cdot K$, and ∇T is a temperature

gradient, with units of $K \cdot m^{-1}$. The minus sign signifies the transfer of heat from a hot body to a cold body, in accordance with the second law of thermodynamics.

In Fourier's law (Eq. (1.1)), κ, the thermal conductivity, is a measure of how well a material conducts heat. Thermal conductivity is of critical interest to research scientists and nuclear reactor operators because it dictates the rate of conduction heat transfer through various structures in a reactor [8, 9, 15–17]. As an example, when heat is generated through nuclear fission in UO_2 it must then be dissipated through the cladding and then into the coolant. Thermal conductivity drives this process, and each material's κ dictates how much heat is allowed to transfer through the various components.

Historically, thermal conductivity for nuclear fuel has been obtained through experiments [10, 15, 16]. Fuel is irradiated for a predetermined duration based on the cycle of fuel in a power reactor – as the uranium undergoes fission, it generates fission products which accumulate and potentially disrupt the ability of the fuel to transfer heat. This process is known as 'burnup' [4, 8, 15]. Measurements to determine burnup and thermal conductivity are destructive in nature – they involve the physical sectioning of the fuel after time to allow for radioactive decay, and thermal resistance measurements of the fuel are taken at various temperatures mimicking operating conditions to determine the thermal conductivity at measured concentrations of fission products and temperature [8–10]. This approach is sufficient as it yields accurate measurements of κ for a variety of isotopic concentrations and temperature, but the experimental data points can be limited to specific operating conditions. Figure 1.1 [15] exhibits the dependence of κ on temperature and theoretical density of UO_2, but does not reflect the changing concentration of isotopes in the fuel, which affect κ. Many of the older measurements of reactor
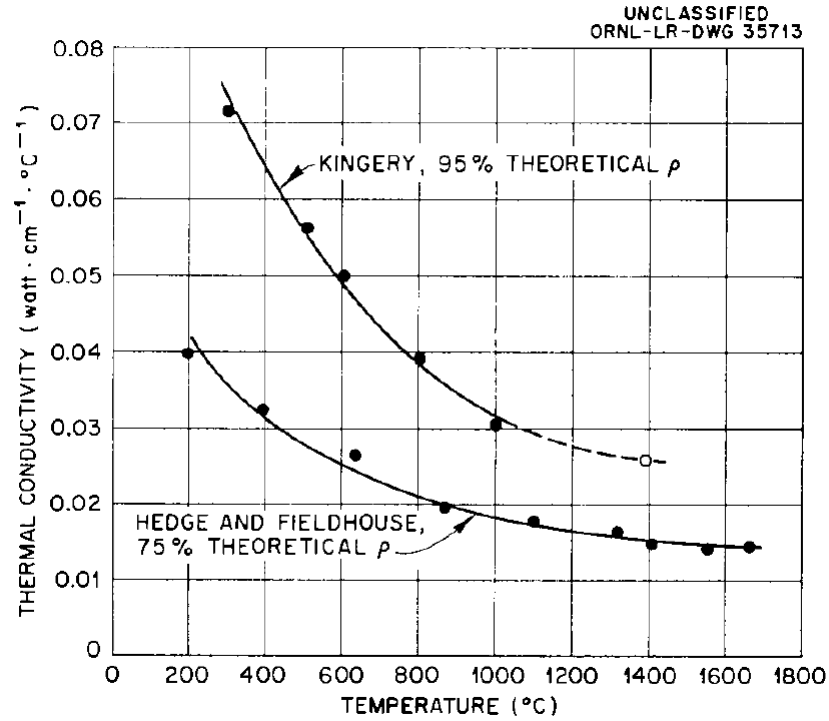
Figure 1.1: Temperature dependent κ in UO_2 (solid dots: experimental, solid line: theoretical prediction)

fuel thermal conductivity do not properly reflect the influence of fission product concentrations, and may not account for any non-standard operating conditions such as reactor SCRAMs or low power operation and thus are subject to significant interpolation error. In addition, uncertainty in experimental measurements of κ also contribute to inconsistencies in the data [10, 15]. Reactor designers and operators rely on interpolation to fill in the gaps, and this approach can generate significant uncertainty in the predictions of reactor performance. Nuclear reactors are built with this in mind, and inherently have a significant conservatism and safety margin [4, 5, 18]. Safety margins are important, and the nuclear industry prides itself on an excellent safety record. If reactor designers and operators could

be better informed as to how thermal conductivity will behave inside an operating reactor, uncertainties in the data could be reduced. This combination of metrics could lead to improved reactor designs with possibly less required material, different operating protocols, and an overall boost in efficiency.

The changes in fission product (defect) concentration in UO_2 affects its *microstructure* – its elemental constituency and spatial structure. As the fission products are continually generated during irradiation, they coalesce, migrate, transmute, and change the microstructure of UO_2. These products can form concentration zones, voids (from the generation of gaseous species) and defect centers. This 'zoo' of microstructure defects can have a profound impact on the fuel performance, and thermal conductivity of UO_2 can decrease by up to a factor of four in light water reactors over the fuel lifecycle. This degradation of fuel demands a more sophisticated approach to the prediction and simulation of thermal conductivity.

In addition to accurate representation of κ, determination of the temperature distribution inside nuclear fuel is also critical. Temperature dictates many different phenomena within nuclear fuels, but one of the most important physics is that of the Doppler broadening effect on neutron cross sections, which is a highly temperature dependent phenomenon [4,5,19]. Heavy mass isotopes may have many lower energy excited states known as resonances, where neutron capture is preferential [4,5,19]. This is shown in Fig. 1.2 for $^{238}_{92}U$ [20], where the excited states resemble singular points in the continuum. Neutrons born from fission are energetic (neutron energy typically ≥ 2 MeV), and in order to cause additional fission and maintain the chain reaction which keeps the reactor critical, they must thermalize to an energy range orders of magnitude lower than their initial energy. However, as these neutrons slow down, it is possible for their capture and absorption to take place in the

resonances. These resonances (which can physically thought of as a "capture area") are affected by changes in temperature, which widens the resonance as temperature increases (though maintaining the same capture area) and affects the amount of absorption, scattering, or fission of neutrons in a reactor. This effect can have a significant impact on the control of an operating reactor if not properly understood or predicted; Fig. 1.3 [5] shows the dependence of the resonance on increasing temperature [4, 5, 19].
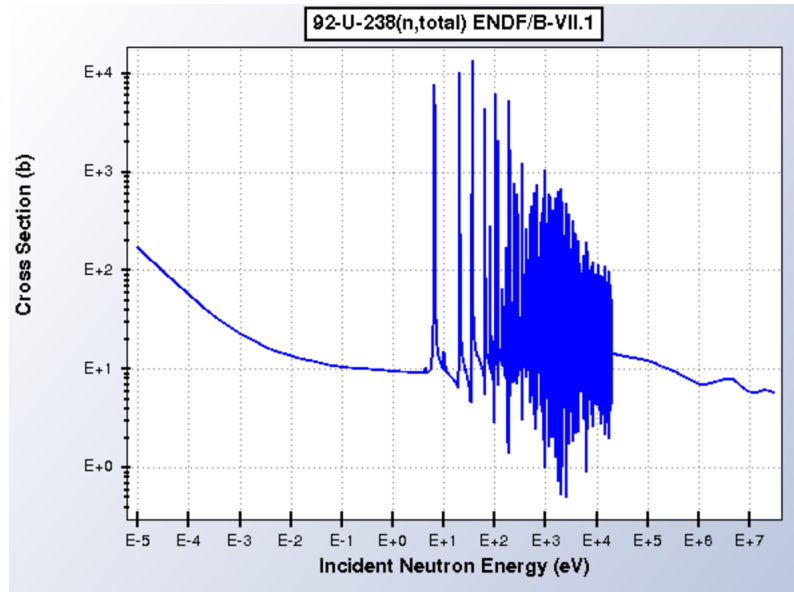
Figure 1.2: Resonances in the total cross section of $^{238}_{92}$U
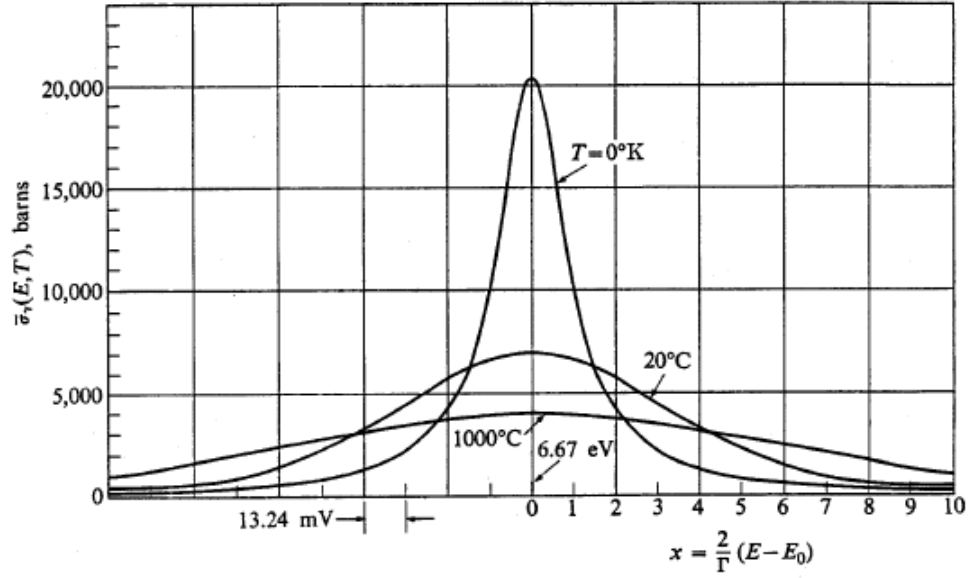
Figure 1.3: Doppler broadening effect on the 6.67 eV resonance in $^{238}_{92}$U

Thermal conductivity, historically being used as a parameter in reactor physics calculations, has not had any intrinsic connection to the elemental disposition of the fuel material. Aside from being taken as a temperature dependent parameter gleaned from experiments performed at specific conditions and then interpolated with significant uncertainty, κ has no dependence on any of the unique traits that nuclear fuel develops as it ages and evolves during under irradiation. Thermal conductivity of a material depends on both the material's innate ability to transport heat, and resistive effects caused by defects in the material. Processes which occur at the atomic scale affect the behavior of heat transport at the microscale, which leads to a shift in κ at the macroscale. An *ab initio* prediction of macroscopic κ (which can be used in engineering calculations) requires simulating detailed processes of heat transport at the nanoscale, and then calculating an *effective* κ in the simulated material from the heat flux and temperature gradient. As geometric domains shrink, a materials response to an applied temperature gradient changes as

well; the systemic interference of heat sources causes a departure from Fourier's law of heat transport, and the Boltzmann transport equation is necessary to adequately describe thermal transport in these reduced length scale environments.

UO_2 fuel is classified as a ceramic (dielectric), despite the presence of uranium metal [8–10, 15]. As a result, the dominant portion of heat conduction in UO_2 is not described by electrons, as it would be in a metallic substance [11–14]. This is due to the types of chemical bonds which form the crystalline lattice structure. Electrons are tightly bound in an insulator and do not carry a majority of the energy, as opposed to the "sea" of valence electrons present in conducting materials [11, 12]. In dielectric materials at the nanoscale, the continual evolution of the microstructure affects the way heat is transported, and in order to resolve an image of the physics which reflect reality, one must resolve the full population of heat carrying *phonons*. Phonon transport dominates heat transfer in UO_2 fuels, and is the primary heat transfer mechanism in semiconductors, insulators, and thermoelectric devices. Phonon transport is complicated with diverse, challenging physics; we will discuss and address some of those aspects in the proceeding sections, which will motivate our research objectives.

In the atomic lattice of dielectrics, the dominant carriers of energy are vibrational modes described by wave vectors and frequencies, generated by atoms oscillating at an equilibrium frequency. When a temperature difference is applied, the atoms generating these waves are displaced from their equilibrium position. The quantization of a packet of vibrational modes is called a phonon, and their behavior (transport) may be described by the Boltzmann transport equation. Transport and scattering of phonons is highly influenced by the dispersion relation (relating a phonons' frequency to its' wavevector), group velocities, and density of states in

the first Brillouin zone. Phonons are also highly sensitive to temperature, which affects mean free path and phonon-phonon collisions; they are tightly coupled to each other and to the total internal energy of the material.

The equilibrium statistical distribution of phonons can be described by the Bose-Einstein (Planck) distribution:

$$\langle n_{\mathrm{BE}} \rangle = \frac{1}{e^{\frac{\hbar\omega}{k_B T}} - 1}. \tag{2}$$

Here, T is the average material temperature, ω is the angular frequency, $\hbar$ and k_B are the reduced Planck's constant and Boltzmann constant, respectively [11, 13, 14]. When a temperature difference is induced in a material, atoms vibrating at their lattice sites are displaced from their equilibrium position, and these displacements give rise to planar waves which transport energy through the material. Though these lattice waves are generated over a range of wavelengths, the dominant energy transport takes place at lower wavelengths, and therefore the waves can be interpreted as sound waves in the material [11, 12]. Physically, a crystalline lattice can be thought of as an array of harmonic oscillators, chains of atoms connected by springs. The motion of phonons results in the divergence of the lattice system from thermodynamic equilibrium. Phonon-phonon scattering, such as normal or Umklapp processes, are restorative and aid in reestablishing thermal equilibrium [14, 21–24].

Although Fourier's law can characterize heat transport at the macroscopic length scale (distances greater than 10^{-3} m), it does not accurately describe thermal transport processes in the microscopic length domain (distances less than 10^{-3} m) [11, 14]. After startup, it is desired that nuclear reactors achieve a steady-state condition for stable operation [4,6]. However, the fuel microstructure is dynamic and constantly changes during the fission process [8,9,15]. The steady creation of fission product and material defects alters the fuel microstructure, impacts the scattering

behavior of phonons and degrades heat flux and thermal conductivity [4, 7–11, 13].

Bai *et al.* performed simulations of thermal conductivity in UO_2 fuels in order to characterize thermal diffusivity in regions of the fuel where high burnup structures formed [25]. High burnup structure (HBS) is a fuel restructuring phenomenon which takes place near the pellet rim region of UO_2 pellets. Fresh UO_2 fuel contains grains about 10 μm in size, and pores may also be present due to the manufacturing process. During fission, UO_2 microstructure undergoes redistribution and formation of new defects, fuel grains, and voids; near the pellet rim, as HBS forms, fuel grain size becomes much smaller, fission gas bubbles and pores also form. The local bubble and pore size is large compared to these grains. Thermal diffusivity and thermal conductivity are both lowered in these regions. From their analysis, Bai *et al.* determined heat transport from phonons were essential to include in the simulation of thermal conductivity; scattering off large grain boundaries in the non-HBS structure, and scattering against Xe reduced overall thermal conductivity [25].

The need for better characterization of reactor fuels using multiscale, hierarchical modeling has been outlined as a directive in the Nuclear Energy Advanced Modeling & Simulation (NEAMS) program [26, 27]. Including the effects of a material's microstructure to better understand UO_2 fuel performance – that is, UO_2 under irradiation with a dynamic microstructure changing due to the fission process – is one goal of the MARMOT and BISON codes [28, 29]. These codes are coupled software designed to integrate separate effects, such as neutron transport and heat conduction, or fission gas migration through grain boundaries. By simulating phonon transport to characterize temperature distributions, heat flux and thermal conductivity, better predictive results for thermal transport modeling may be obtained, and the effect of material microstructure on heat transport could be realized. For

example, if thermal conductivity as a function of defect concentration in UO_2 could be predicted, the resulting data could be coupled to BISON thermomechanical simulations which characterize stress, strain, and thermal expansion in UO_2 [29]. In UO_2 undergoing fission, the microstructure is constantly evolving and altering the behavior of thermal transport; the capability to model this dynamic process instead of relying upon empirical fits for thermal conductivity may provide a benefit to reactor operators [8, 9, 15].

Given the motivation to improve data used in reactor physics simulations, the development of a computational framework to model phonon transport would allow researchers to more accurately characterize processes affecting heat transport in UO_2 fuel in nuclear reactors. This framework would allow the modeling of phonon transport in any material where phonons are the dominant mechanism of heat transfer, such as graphite, semiconductors, thermoelectric devices, or new types of fuel under development for Generation IV nuclear reactors [30–34], and would not be restricted only to nuclear fuels.

This framework would involve a variety of existing methods – in fact, one method is not enough to capture the entire scope of the problem, and a multi-physics, multi-software approach must be considered to obtain results usable at the engineering scale [26–28, 35–42]. For example, if the discretized Boltzmann transport equation (a deterministic method) is used, material data would be necessary and could be produced from molecular dynamics (MD). Molecular dynamics is a technique which simulates systems of atoms based on the numerical integration of Newton's equation of motion, and describes interactions between atoms using a large array of interatomic potential models [41, 42]. Density functional theory (DFT) is another such computational method of *ab initio* data prediction, quantum mechanical in

nature, which is used to investigate the electronic structure in many-body systems, by solving the Schrödinger equations for electron probability densities. In this method, electronic potentials are leveraged and only the atomic structure and composition is necessary to predict its electronic properties, from which data for phonon transport simulations can be elucidated.

It becomes clear that a computational framework should be developed in order to rapidly provide predictions of thermal conductivity in nuclear fuel, independent of the operating history of the reactor and dependent only on the properties of the fuel and its burnup history. This method of prediction must consider processes which occur on an atomistic scale, the production of fission products, the formation of defects in the microstructure of the fuel [4,5,11,13,14], the evolution of burned-in plutonium [8–10,15], and the formation and migration of gas bubbles due to fission or alpha decay of plutonium [43–46]. It is important to understand these phenomena and model them accurately.

1.2   Elements of Phonon Transport

1.2.1   Interface Physics

Phonons encounter resistance when attempting to translate through a material discontinuity. If two dissimilar materials are conjoined, as phonons transmit across the border they encounter a resistive effect, known as thermal boundary resistance [47, 48]. This is due to the difference in material properties (group velocity, density of states and specific heat capacity). At this interface phonons have a probability of being reflected or transmitted, determined by the available and occupiable states. Two primary models have been developed to describe this behavior, the acoustic mismatch model (AMM) and the diffuse mismatch model

(DMM) [47]. These models have been applied to both deterministic and Monte Carlo methods of phonon transport. A boundary physics model is essential to describe phonon scattering and transmission at intra-material interfaces, which is especially useful in simulating phonon transport in materials with defects [49, 50]. As phonons flow across the interface they encounter a resistance which is due to the availability of states for phonons to occupy and the change in lattice spacing and phonon speed in the respective materials. Currently, researchers have developed deterministic methods to simulate TBR in 1D and 2D spatial domains [51–53], but to our knowledge there is no existing capability which simulates TBR in 3D, general geometries.

In order to induce a heat flow $\dot{Q}$ in a material, a temperature gradient ∇T must be imposed. The radio of the heat flux per unit area A to the temperature gradient is the definition of thermal conductivity

$$\kappa = \frac{\dot{Q}}{A\nabla T}. \tag{3}$$

For a heat flow to exist across a boundary between two materials, there must be a temperature difference between the two sides of the interface, in addition to the temperature gradients in the adjoining materials. This effect is subtle, and the presence of the interface in addition to a heat flow presents a challenge in defining a temperature [47]. A thermal boundary conductivity due to a temperature discontinuity across an interface can be defined in a similar way to Eq. (3)

$$\kappa_{\mathrm{Bd}} = \frac{\dot{Q}_{\mathrm{Bd}}}{A_{\mathrm{int}}\Delta T_{\mathrm{Bd}}}. \tag{4}$$

The calculation of κ_{Bd} is very similar to κ, κ_{Bd} is determined by the number of phonons incident on the surface, the energy carried by the phonon, and the probability the phonon is transmitted across the interface. Difficulties arise for each

quantity in that it is a challenge to accurately determine a mean free path Λ for κ, and difficult to quantify the transmission probability for phonons contributing to κ_{Bd}.

Thermal boundary conductivity is a geometrically independent quantity, such that doubling the area of an interface doubles the thermal boundary conductance, but not the thermal boundary conductivity [47].
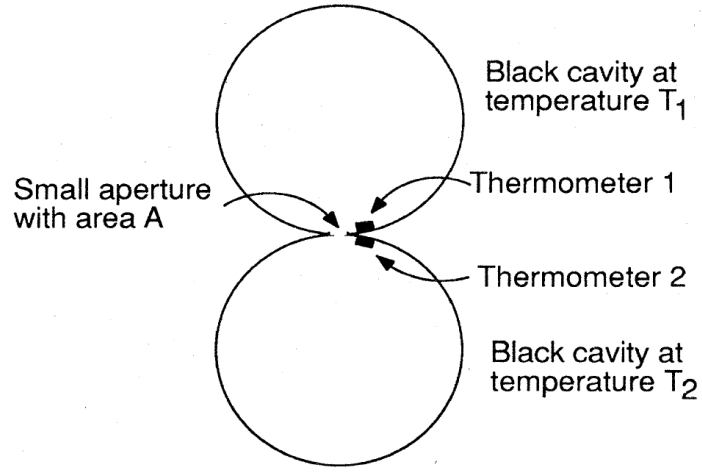
Figure 1.4: Black-body cavity experiment

Figure 1.4 shows two black-body cavities connected by a small orifice with an area A [47]. One cavity is held at T_2 and the other is at a lower temperature T_1. The heat flow between the two cavities is

$$\dot{Q} = \sigma A \left(T_2^4 - T_1^4 \right) , \tag{5}$$

where σ is the Stefan-Boltzmann constant. In Fig. 1.4 there is no interface except an imaginary one in between the cavities, and there is no temperature discontinuity at that interface. However, the photons incident on the interface from above have a frequency distribution characteristic of the temperature T_1, and the photons

incident from below have a frequency distribution characteristic of temperature T_2. The temperature difference used in the definition of thermal boundary conductivity (or resistance) is that between photons (or phonons) incident on respective sides of the interface.

The complexity of TBR lies in determining the transmission probability of phonons, which generally depends on the side from which the phonon hits the interface, the angle of incidence, its frequency and polarization, and the temperature of both sides of the interface. In thermodynamic equilibrium, the number of phonons of a given phonon state (at polarization p and wave vector $\mathbf{k}$) leaving one side is the same as the number of phonons returning from the other side into that state, which is one of the principles of detailed balance.

Figure 1.5 [48] shows an Si/Ge interface, and in the absence of scattering within the junction, the TBR is equal. However, with the inclusion of TBR, we see a temperature discontinuity occur at the interface, shown in Fig. 1.6 [48].
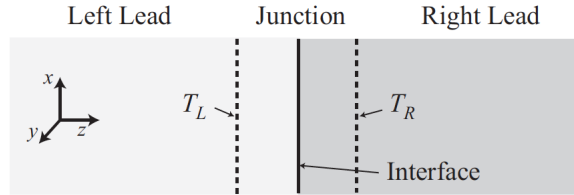
Figure 1.5: Dissimilar material interface, no boundary scattering
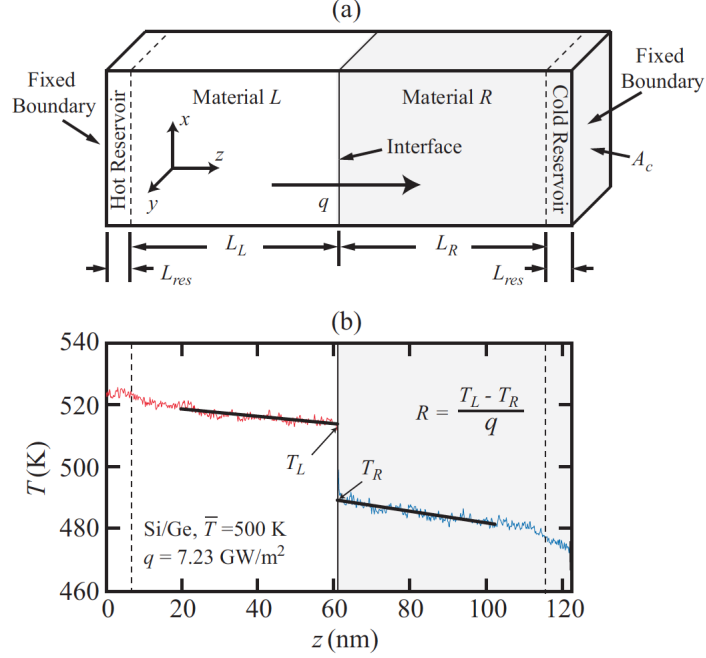
Figure 1.6: Si/Ge interface with inclusion of boundary scattering showing temperature slip

1.2.1.1   Acoustic Mismatch Model

Under the assumptions of the acoustic mismatch model (AMM), phonons are governed by continuum acoustics, and the interface is treated as a plane. Phonons are treated as planar waves and the materials that the phonons propagate through assume no lattice (continuum). For phonons with a wavelength much greater than the lattice constant, this approximation can be accurate [47]. The most simple model for AMM is for an isotropic material, where each material is assigned an acoustic impedance, which is the product $Z_i = \rho_i c_i$ of the mass density ρ_i and phonon velocity c_i. To determine the transmission probability $\alpha_{1\to2}$ of phonons transmitted from material 1 into material 2

$$\alpha_{1\to2} = \frac{4Z_1 Z_2}{(Z_1 + Z_2)^2}.$$ (6)

The crystalline solids considered for this approach are assumed to be isotropic, with phonon velocities differing in longitudinal and transverse directions. This approach also ignores effects of elastic anisotropic scattering and the phonon dispersion relation. The AMM is generally only considered for simulations and experiments far below 300 K [47–49].

1.2.1.2 Diffuse Mismatch Model

The diffuse mismatch model (DMM) is typically employed for most phonon transport simulations in real materials due to the temperatures of interest being at 300 K or higher [48, 51, 52, 54]. DMM assumes all phonons are assigned a probability of transmission or reflection at an interface and have no memory of their origin, thus becoming a diffuse flux which has contributions from the phonon flux on either side of the interface [47, 54]. Energy conservation and detailed balance are enforced, and these coefficients are prescribed by

$$T_{\alpha \to \beta} = \frac{U_\beta v_{g,\beta}}{U_\alpha v_{g,\alpha} + U_\beta v_{g,\beta}}, \qquad R_{\alpha \to \beta} = 1 - T_{\alpha \to \beta}. \tag{7}$$

Where U is internal energy, and we are simulating a phonon flux at an interface, flowing from material α into material β. These coefficients are defined in a similar way for phonons flowing from β into α. This approach has been taken by researchers using deterministic and MD methods and results from these simulations tend to be in good agreement with each other [48, 51, 52, 54].

1.2.2 Spectral Phonon Transport

Phonon scattering and transport change drastically at different frequencies, as a vibrational *spectrum* is generated by displacements to the atoms' equilibrium

harmonics. Method development is sometimes performed using the *grey* approximation [17], which is an effective development strategy but lacks the robustness to characterize phonon behavior across a broad range of frequencies which would be present in a real material under an imposed temperature difference. Harter *et al.* [55,56] have previously predicted thermal conductivity in materials by simulating phonon transport, integrating the entire dispersion relation and density of states into one lumped term and prescribing phonon intensity using heat capacities and an average group velocity. This approach is adequate initially, as it is computationally inexpensive and allows for rapid development. In homogeneous, isotropic materials, the grey approximation can appropriately predict bulk properties given a sufficiently large spatial domain. However, if the derivatives of the curves in the dispersion relation (which yield phonon group velocities) are rapidly changing, the grey model will fall short.

Simulating phonon transport using the full range of dispersion and density of states can finely characterize the phonon behavior and gives a unique perspective into the primal coupling between phonon modes. The central limitation of the grey approach is its inability to model transport in anisotropic materials or across strongly frequency selective boundaries. The next level of approximation that can address this is to model frequency dependent transport across the phonon spectrum, including contributions from anharmonic phonon processes. Simulating frequency dependent phonon transport is an effective way to characterize different scattering mechanisms and understand the intrinsic coupling of temperature to the internal energy in materials [11,13,57]. The phonon equilibrium radiance is connected to temperature via the Bose-Einstein distribution, and simulating frequency dependent transport can effectively introduce temperature feedback into its solution [57–59].

The frequency spectrum can be partitioned into discrete groups, similar to the multi-group treatment in neutron transport [4, 5, 57, 59]; Rattlesnake could be leveraged to perform this task.

Allu [57] investigated frequency dependent phonon transport in 3D silicon slabs with heat sources. Because phonons from different frequencies have different mean free paths, they altered the Knudsen number (the mean free path divided by the domain length) of a material; phonons fall into different transport 'regimes' – ballistic and diffuse. Allu wrote a solver which determines which regime the mean free path is in, and chooses to either solve a diffusion equation or a transport equation, and this can provide a speed increase by solving a less computationally expensive problem. By applying a frequency dependent formulation, they were able to include effects from the phonon dispersion and polarization. This approach gives a more holistic description, as phonon velocities are derived from the dispersion relation and change with frequency. The polarization of a phonon is its orientation as it travels through the lattice in the transverse or longitudinal direction. Polarization should be included as was in Mazumder and Majumder [60], where transitions between polarization and branches were included. This occurs in both phonon scattering in host materials as well as in anharmonic interactions [21].

Other researchers have given attention to frequency dependent transport. Hua derived the time and frequency dependent phonon transport equation using the method of degenerate kernels in an attempt to increase efficiency compared to traditional integral discretization methods [58]. They found they could reduce required size of their matrix to an $N \times N$, $N = 20$ system compared to an $N = 1000$ matrix for the same problem, and obtain a drastic increase in efficiency. However, this was only done in 1-D, and they did not provide any spatial discretization, the

solution method was primarily analytical [58]. As simulating frequency dependent phonon transport allows for the characterization of the frequency spectra, it allows for mode dependent contributions to the specific heat capacity and phonon velocity. Minnich *et al.* [54] showed this effect in their simulations of aluminum and silicon and calculated the spectral heat capacity from each frequency interval, explicitly calculating their contributions to thermal conductivity. Zhang *et al.* [61] recently developed a coupled approach using a reference temperature formulation which efficiently simulates temperature distribution and thermal conductivity over the nano- to micro-scale length range. However, they did not consider optical phonons with short mean free paths in their simulations.

The true characterization of the phonon spectrum in materials relies on simulating frequency dependent phonon transport with the inclusion of thermal boundary resistance effects and anharmonic phonon scattering. Temperature differences disrupt the equilibrium frequency spectrum in the host material, and phonon velocities, polarization, relaxation times, other material and transport properties change with respect to frequency [57–59]. Simulating frequency dependent phonon transport is an accepted approximation to the way a real frequency spectrum behaves under a temperature difference [57–60, 62].

Chernatynskiy and Phillpot developed PhonTS, a code which uses the BTE to predict thermal conductivity in solids and interfaces with MD and DFT methods to obtain data to aid in the transport simulation [63]. PhonTS is effective in predicting lattice thermal conductivity and other phonon properties, but these simulations are based on very small geometries, systems of approximately 10^4 atoms and are very resource intensive. PhonTS works well with prediction of thermal conductivity in pure crystals without defects, but has difficulties when simulating materials with

real microstructures and isotopic defects. The code solves the linear form of the BTE under the RTA. Anharmonic oscillations are approximated by considering anharmonicity to be a perturbation of the harmonic term in the Hamiltonian. Interatomic force constants (IFCs) are required for the anharmonic model, these are third derivatives of the interatomic potential which PhonTS can calculate. The authors state their solution methods are variational and iterative in nature, but do not give any details. The code uses LAPACK as a linear algebraic solver system, which solves matrices in the forms of SPD, symmetric, Hermitian, etc. Some of the drawbacks with PhonTS are the physical size of the system itself; as PhonTS seeks to reproduce MD results very exactly, material systems are Brillouin zones must be chosen to be the exact same size and order as MD studies, which are limited. Their transport regimes are unreliable for temperatures as high as $\frac{1}{3}T_m$ or $\frac{1}{2}T_m$, which a limiting feature when considering the operating conditions of nuclear fuel. The authors also note their approach not appropriate in modeling phonon scattering off material impurities. Because of the variation in the BTE and MD approaches, PhonTS requires a careful match of transport data to MD data. Specifically, thermal expansion: the phonon modes are extremely sensitive to the volume and shape of the primitive cell; the same primitive cell geometry must be used in both BTE and MD simulations. ShengBTE is another package which solves the BTE and takes input from third party codes; the code computes three phonon scattering rates using the RTA, and certain types of isotopic disorder, but this is heavily dependent on the materials being simulated and has its own set of limitations [64]. Both ShengBTE and PhonTS are composed of subroutines which handle particular aspects of phonon transport, but neither is a pristine transport engine optimized for solving the phonon BTE efficiently.

Phonons are neutral 'quasiparticles', and phase space distributions may be used to describe their population density [11, 13, 65]. Neutrons are also neutral particles, represented by the same phase space distributions. As a result, we are able to simulate their transport in real media through application of the Boltzmann transport equation (BTE) [11, 65]. We have previously demonstrated the effectiveness of a neutron transport code, Rattlesnake [66, 67], which we had modified to simulate phonon transport [55, 56, 68]. Rattlesnake solves the Self-Adjoint Angular Flux [69] (SAAF) form of the BTE for neutrons, written in the Multiphysics Object Oriented Simulation Environment (MOOSE) [70] framework. MOOSE is is a powerful C++ oriented framework for solving coupled systems of partial differential equations using unstructured continuous finite element grids, is massively parallel, and leverages state of the art numerical solvers. The SAAF form of the BTE yields a transport equation with an elliptic, second order operator which generates systems of linear equations upon discretization, which can be solved via the GMRES [71] solver, an efficient numerical method for solving linear systems of equations.

The numerical procedures for computing the contribution from each frequency group in reciprocal space to the total thermal conductivity in phonon transport are similar to the procedures used for multi-group neutron or radiation transport [4, 72]. With neutron or radiation transport, the energy spectrum is partitioned into discrete groups and considers within-group and group to group scattering based on the interaction cross sections. Rattlesnake [73] employs a multi-group energy discretization scheme, solves the BTE for neutrons and allows for simple construction of particle group scattering profiles. This approach can, and has been adapted to simulate multi-group phonon transport [57, 59, 61].

1.2.3 Convergence Acceleration

The development of methods to solve a spectrally-dependent phonon transport simulation have led to high-fidelity outputs which compare well with experimental results, heralding an era of improved heat transport predictions for many devices used in engineering applications. The drawback of these high-fidelity simulations is the requirement of large amounts of computational resources to converge the problem. To *converge* a simulation, we require that the error between iterations to be reduced by a certain amount, generally on the order of 10^{-6} or less. The *convergence properties* of a simulation imply how rapidly the error between iterations is reduced. In a quickly convergent simulation, the error is reduced rapidly between iterations, and in a slowly convergent simulation, it may take hundreds or thousands of iterations to converge, as the error is not reduced appreciably between iterations. The generation and discretization of material properties within the first Brillouin zone for a simple, isotropic material such as silicon is relatively trivial, as the dispersion relation of Si has symmetries which allow for simplifications and a relatively coarse wave vector group discretization. However, as materials gain in complexity, e.g., multi-atomic systems such as $LiAlO_2$, anisotropy (simulating Jahn-Teller distortions in oxygen [30]), or acoustic thickness (simulation of large sections of a UO_2 fuel pin, or a micrometer scale thermoelectric device). All of these phenomena may degrade the convergence properties of phonon transport simulations, but the critical offender is generally the "acoustic thickness" of the problem, ζ, defined as

$$\zeta = \frac{\mathcal{D}}{\Lambda},\tag{8}$$

where $\mathcal{D}$ is the length of the geometric domain. When the Λ is discretized into groups, certain groups are ballistic or diffuse, and the diffuse groups are generally

optically thick; phonons undergo many collisions before reaching a boundary.

The history of numerical acceleration methods for particle transport is a diverse and rich one. One of the earliest techniques used to solve the neutron transport equation is known as "source iteration" (SI) [74], which is described by the following iteration scheme

$$\hat{\mathbf{\Omega}} \cdot \nabla \psi^{(\ell+1/2)} + \sigma_t \psi^{(\ell+1/2)} = \frac{1}{4\pi} \sigma_s \phi^{(\ell)}, \tag{9a}$$

$$\phi^{(\ell+1/2)} = \int_{4\pi} \psi^{(\ell+1/2)} d\Omega, \tag{9b}$$

$$\phi^{(\ell+1)} = \phi^{(\ell+1/2)}. \tag{9c}$$

In the SI algorithm, the angular flux from the previous iteration is used to calculate a new source for the next iteration, and so on. This algorithm used by myriad software to solve the neutron transport equation, but breaks down when problems are diffusive (and therefore "optically thick", the neutron analog of acoustic thickness). This can lead to inordinately high computation times.

One of the most difficult classes of neutron transport problems are those where no absorption exists, e.g., pure scattering cases in which the total cross section σ_t equals the scattering cross section σ_s, and the *scattering ratio c* is equal to 1.

It can be shown that the reduction in error from one iteration to the next one using source iteration is characterized by ρ, the spectral radius [75].

Traditionally, the majority of phonon transport simulations and predictions are done on relatively small geometric domains (sub 500 nm) and computational efficiency was not a primary consideration, rather the correct answer was. However, as more researchers and research directives are recognizing and leveraging the benefits of performing phonon transport to simulate heat transport in dielectrics, the geometric domain sizes considered are increasing. As these domains become

more acoustically thick, acceleration techniques could be applied to drive efficiency in parallel with accuracy. Other researchers have applied acceleration techniques; a popular choice is a hybrid "ballistic-diffuse" solver, where a predetermined tolerance on acoustic thickness is chosen [57, 59, 76, 77]. If phonons have a mean free path which falls within this tolerance, a diffusion, rather than transport, equation is solved; this is an attempt to limit the influence of diffuse modes, which generally carry much less heat than their ballistic counterparts. Lei *et al.* [78] derived a synthetic iterative scheme dependent on the method of moments for the steady state phonon BTE, which is rapidly convergent. However, their heat flux was not conserved and parabolic, suffering from edge effects; temperature profiles did not show the full temperature slip. Acceleration is a very new facet of phonon transport methods and has much potential for development.

1.3   Research Objectives

Each of the three components of phonon transport we discussed in Sec. 1.2 play an integral role in phonon transport simulations; in order to develop an accurate and efficient method for predicting materials properties (thermal conductivity), temperature distributions and heat flux, a phonon transport framework must possess all of these components, at a minimum. Therefore, this dissertation is concerned with the work performed, motivated by the necessity of including each of these components. To achieve a goal in predicted thermal conductivity in nuclear fuels with isotopic defects, an interface physics model must be developed for the transport software, which allows for the accurate representation and conservation of particle flow at internal material interfaces. In order to capture the detailed physics contained in the phonon frequency-wavevector spectrum, a spectral transport

method must be developed which allows for the simulation of both an angular flux intensity and an equilibrium phonon radiance, which are coupled through temperature. Finally, as the physical domains which we desire to predict these properties on can be large compared to a phonon's mean free path, and because the standard choice of iterative method used to solve these equations drastically slows down in large domains, some form of convergence acceleration must be introduced to speed up these calculations, while maintaining solution accuracy.

In light of these goals, distilled from our motivation to better predict material properties in nuclear fuels, our objective is thus: to use deterministic, frequency dependent phonon transport simulations to characterize heat flux, thermal conductivity, and temperature distributions in heterogeneous structures in an efficient manner. We plan to use data generated by *ab-initio* methods to inform our mesoscale BTE simulations to generate thermal conductivity distributions which may eventually be used in engineering-scale reactor physics calculations. Due to the physical size of the materials we simulate, and the desire to have an efficient transport engine, we must also include some form of convergence acceleration, to reduce the computational burden of our spectral transport method. Therefore, our research objectives are as follows:

1. Develop, implement, and test a interface physics model for general geometries

2. Develop, implement, and test a spectral, implicitly coupled phonon transport method for general geometries

3. Develop, implement, and test a convergence acceleration scheme for phonon transport for general geometries

1.4 Dissertation Overview

The remainder of this dissertation is organized as follows: Chapters 2 to 4 are each self contained journal papers composing one of the elements of phonon transport theory contained in Sec 1.2. Chapters 2 and 3 are published, whereas Chapter 4 is a draft. Each of these chapters is separate from the other, e.g., the equations, figures, and tables in Chapter 2 are independent of similar items in Chapter 3, and so on.

I. Chapter 2 contains the journal paper presenting the SAAF equations in a grey formulation as applied to a heterogeneous system of UO_2 and xenon, develops and implements a 3D interface physics model to capture phonon scattering effects at a xenon bubble interface. The material properties were generated via *ab-initio* methods.

II. Chapter 3 contains the journal paper presenting a spectral method for solving deterministic, fully coupled, temperature dependent phonon transport in 2D grids of silicon, and introduces a closure term to conserve energy lost between the angular phonon intensity and equilibrium phonon radiance. Silicon material properties are generated via *ab-initio* methods, and we develop a new discretization scheme which gives the material properties angular dependence inside the first Brillouin zone. We perform angular and spatial mesh refinement studies and leverage adaptive mesh refinement techniques to address boundary scattering effects.

III. Chapter 4 contains the draft paper which presents a convergence study. In this paper, we compare the efficiency and performance of the new method (modified source iteration) with the traditional method of source iteration. We

performed these convergence studies for a 2- and 4- group phonon transport problem with various angular and spatial discretization refinements.

IV. Chapter 5 is where we make some concluding remarks and establish direction and motivation for future research.

2   Deterministic Phonon Transport Predictions of Thermal Conductivity in Uranium Dioxide With Xenon Impurities

Jackson R. Harter, Laura de Sousa Oliveira, Agnieszka Truzkowska, Todd S. Palmer,

P. Alex Greaney

2.1 Abstract

We present a method for solving the Boltzmann transport equation (BTE) for phonons by modifying the neutron transport code Rattlesnake which provides a numerically efficient method for solving the BTE in its Self-Adjoint Angular Flux form. Using this approach, we have computed the reduction in thermal conductivity of uranium dioxide (UO_2) due to the presence of a nanoscale xenon bubble across a range of temperatures. For these simulations, the values of group velocity and phonon mean free path in the UO_2 were determined from a combination of experimental heat conduction data and first principles calculations. The same properties for the Xe under the high pressure conditions in the nanoscale bubble were computed using classical molecular dynamics. We compare our approach to the other modern phonon transport calculations, and discuss the benefits of this multiscale approach for thermal conductivity in nuclear fuels under irradiation.

2.2 Introduction

One of the fundamental quantities of interest in the safe and efficient operation of nuclear reactors is thermal conductivity (κ) of the fuel, which greatly influences heat transfer throughout the structure of the nuclear core and into the coolant [6, 79]. In addition to heat transfer, thermal conductivity is coupled to many other processes in the reactor core. Shifting thermal gradients have a strong influence on the macroscopic cross sections of interaction for neutrons [79]. These cross sections are of high importance since they dictate rates of nuclear fission, neutron absorption and scattering within the fuel. As temperatures increase, so do the effects of Doppler broadening, which alter neutron scattering and absorption. While this is not a new phenomenon, reactor operators must be keenly aware of the effect temperature has

on the absorption and scattering behavior of neutrons. The focus of our work is to develop a predictive computational tool which simulates thermal transport in heterogeneous nuclear fuel in service and under irradiation, with fission product defects.

Thermal conductivity in nuclear fuel is currently obtained through empirical relationships which have been experimentally determined from measurements made during the past 60-70 years [15]. Thermal resistance measurements are performed on nuclear fuel with operating histories, i.e. irradiated fuel and values are obtained at specific temperatures and isotope concentrations. This approach does not consider the constantly changing concentration of isotopic byproducts in the fuel, nor has it historically provided appropriate values across a wide range of reactor operating conditions without significant interpolation error [10, 15]. Reactor designers and operators, however, rely on interpolation to fill in the gaps which can be a significant source of uncertainty in predictions of reactor performance. Nuclear reactors are constructed conscious to this attribute and thus have a significant conservatism and safety margin [6].

A better predictive approach to the computation of thermal conductivity could reduce these margins, creating improved performance and economics without compromising safety. A predictive simulation tool could also reduce the reliance on experiment for the development of new fuels for advanced reactors.

Development of nuclear reactors is an ongoing process. The current generation of power reactors are light water moderated and use uranium dioxide (UO_2) fuel. In the future, generation IV nuclear reactors will continue to use solid fuel. Uranium-based TRISO particles are used in prismatic block high temperature gas reactors (HTGRs), while other fuels such as uranium-molybdenum (UMo) and uranium-

carbide (UC) are in development for a plate or pellet based application [80, 81]. Experimental measurements of thermal conductivity will likely be performed on these new fuels, and could result in more empirical correlations used to predict their performance under irradiation. The need for a predictive computational tool to reduce the reliance on destructive thermal conductivity measurements is steadily increasing.

We are developing a deterministic computational framework for simulating phonon transport. When supplied with appropriate information (temperature, isotopic concentration of fission products, material properties) this framework would predict thermal conductivity in heterogeneous nuclear fuel with an operating history. The fission product significantly hindering thermal transport in UO_2 is widely accepted as xenon [3], a noble gas which accumulates in UO_2 over its operational life-cycle. The bulk of thermal conductivity characterization is done with MD methodology, which models energy flow explicitly through atomic motion. MD is effective in predicting thermal conductivity, but is only able to model small systems of atoms due to the significant computational cost of the method.

To this end we leverage the code Rattlesnake, which solves a second-order form of the BTE using the Self-Adjoint Angular Flux (SAAF) formulation [82] using continuous or discontinuous finite element (CFEM and DFEM) spatial discretization [83]. Rattlesnake is a member of the Multi-physics Object Oriented Simulation Environment (MOOSE) [70] architecture developed and maintained by Idaho National Laboratory. We have shown Rattlesnake may be adapted to simulate phonon transport, and demonstrates promise in connecting transport phenomena at the nanoscale to properties which may be used at the macroscale [84]. We motivate the use of the SAAF formulation of the transport equation and discuss the advantages

and disadvantages of the numerical solution of this equation in comparison with solvers for the traditional first-order integro-differential form of the equation.

Our numerical solution technique involves traditional source iteration (SI, a Richardson iteration) methods combined with a robust linear algebraic solver to solve the systems of discretized equations generated by the second-order BTE. With the application of preconditioning we are able to rapidly solve these systems with tremendous savings in computational cost relative to traditional methods. Additionally we have the capability to apply nonlinear diffusion acceleration (NDA) as these simulations become very acoustically thick to yield an even greater convergence acceleration. As such this approach opens the door for BTE simulation to model heat transport in relatively large systems that contain realistic and statistically representative material microstructures. This approach can potentially become a truly practical and predictive tool to nuclear engineers and material scientists.

2.3 Methods

The generalized Boltzmann transport equation is used widely by the transport community. Phonons follow Bose-Einstein statistics in thermodynamic equilibrium and are uncharged like neutrons, which greatly simplifies the mathematical description of their behavior. The BTE for a frequency dependent phonon distribution f_ω is

$$\frac{\partial f_\omega}{\partial t} + v_g \mathbf{\Omega} \cdot \nabla f_\omega = \dot{f}_{\omega|\text{scatt}}. \tag{1}$$

For brevity, we have suppressed the independent variables in many of the terms of the equations. The phonon phase space density is $f_\omega = f(\mathbf{r}, \mathbf{\Omega}, \omega, p)$, $\mathbf{r}$ is the spatial coordinate $\mathbf{r} \equiv (x, y, z)$, $\mathbf{\Omega}$ is the unit vector denoting the direction of travel $\mathbf{\Omega} = (\phi, \theta)$, and ω is angular frequency. p is polarization; the geometrical orientation

of phonon travel and is transverse in two directions (T) or longitudinal (L). Group velocity v_g is related to the propagation speed of phonons, which can have either acoustic (A) or optic (O) modes. However, for this work we assume a single phonon speed averaged over the acoustic modes and polarizations at varying temperatures, an assumption for the transport of gray phonons which is addressed in Sec. 2.4.2.

In a steady state nuclear heat generation environment (nuclear fuel at operating temperatures) we assume no external electrical or magnetic field and Eqn. (1) simplifies to

$$v_g \mathbf{\Omega} \cdot \nabla f_\omega = \dot{f}_{\omega|\text{scatt}}. \tag{2}$$

The scattering kernel $\dot{f}_{\omega|\text{scatt}}$ contains nonlinear operators and includes contributions from processes such as anharmonic phonon interactions or material defect scattering. Other contributions to Eqn. (2) can include thermal boundary resistance (TBR) or defect scattering. We use a weak formulation of the phonon transport equation, in which we include upwinding terms to describe the interface condition of TBR, which we develop later.

We apply the single mode relaxation time approximation (SMRTA) to simplify the scattering kernel in Eqn. (2) – we assume phonons to occupy a single mode, with their scattering contributions collected into a single, effective "relaxation" time, τ_{eff} which is on the order of 10^{-12} s, and describes the response time between phonon scattering events. The kernel is now effectively a measure of the displacement about equilibrium of the phonon distribution function f_ω [11]

$$\dot{f}_{\omega|\text{scatt}} = \frac{f_\omega^0 - f_\omega}{\tau_{\text{eff}}}, \tag{3}$$

here $f_\omega^0 = f_\omega^0(\mathbf{r})$ has been shown to be purely spatially dependent [84]. For small deviations of the phonon distribution function the scattering term may be expressed by Eqn. (3). If a temperature gradient is not present, $f_\omega^0 - f_\omega = 0$ and the scattering

term vanishes. In solving for the phonon distribution f_ω at spatial location $\mathbf{r}$, f_ω only shifts a small amount from its local equilibrium distribution f_ω^0, fixed by the local temperature at $\mathbf{r}$. Substituting Eqn. (3) into the right hand side of Eqn. (2) yields

$$\boldsymbol{\Omega} \cdot \nabla f_\omega = \frac{f_\omega^0 - f_\omega}{\Lambda}, \tag{4}$$

where v_g has been brought to the right hand side to obtain Λ, the phonon mean free path (the product of group velocity and relaxation time).

2.3.1 Transport of Gray Phonons

We apply an isotropic gray approximation to the BTE for phonons, yielding a frequency independent formulation. This approach combines the contribution to transport from all phonon frequencies and polarizations, and can be averaged into a single effective radiant energy intensity of phonons with a single effective mean free path that accounts for all scattering processes across the phonon frequency spectrum. This is the simplest approach for capturing the ballistic nature of phonon transport over short distances, and provides an adequate description of heat transport physics providing there is no strong heterogeneity in frequency selective scattering. Equation (5) defines the phonon radiant intensity operator

$$\mathcal{M} = \frac{1}{4\pi} \int_0^{\omega_{\text{limit}}} \sum_p v_g \hbar \omega \mathcal{D}(\omega) d\omega, \tag{5}$$

and can be applied to a phonon frequency distribution to yield phonon radiant intensity $I(\mathbf{r}, \hat{\Omega})$ which has units of $\text{W} \cdot \text{m}^{-2} \cdot \text{sr}^{-1}$. The phonon frequency distribution is multiplied by $v_g \hbar \omega \mathcal{D}(\omega)$, summed over all phonon branches and polarizations and integrated over all possible frequencies (limited by the vibrational frequency of the medium). Here, $\hbar$ is the reduced Planck's constant, and $\mathcal{D}(\omega)$ is phonon density of states.

Operating on Eqn. (4) with $\mathcal{M}$ yields

$$\Lambda \boldsymbol{\Omega} \cdot \nabla I\left(\mathbf{r}, \boldsymbol{\Omega}\right) = I^0\left(\mathbf{r}, \boldsymbol{\Omega}\right) - I\left(\mathbf{r}, \boldsymbol{\Omega}\right). \tag{6}$$

Equation (6) is the equation of phonon radiative transfer (EPRT) [85]. The allure of the gray phonon EPRT is that the consequences of ballistic transport between geometric scattering features are determined explicitly but the entirety of the local intrinsic and extrinsic scattering physics is lumped into a single parameter that may be obtained empirically, from first principles, or some hybrid mixture of both. The next level of approximation is to model transport explicitly including the spectrum of participating phonon frequencies.

The central limitation of the gray approach is its inability to model transport in anisotropic materials or across strongly frequency selective boundaries. The next level of approximation that can address this is to model frequency dependent transport across the phonon spectrum, but to still treat collision terms through the single relaxation approximation. From the point of view of our efficient SAAF solution method the two approaches are numerically identical with independent equations coupled only through a single integral term. For simplicity of demonstrating the SAAF approach we limit the scope of this work to the gray phonon model. While we have chosen to demonstrate the effectiveness and efficiency of our numerical approach in the context of frequency-independent transport, the extension to the solution of the frequency-dependent BTE with the relaxation time approximation is trivial since frequency appears as a parameter in the equation; i.e. the solution in each frequency group is decoupled from all other groups.

2.3.2 Self-Adjoint Form of the Phonon BTE

Morel and McGhee [82] outline an algebraic technique for the derivation of the self-adjoint form of the neutron transport equation. From a computational perspective the SAAF formulation is advantageous, since the full angular flux becomes the unknown. Using reflecting boundary conditions becomes easier with the availability of the full angular flux, as the incoming and outgoing directions are coupled in the same manner as the first order form of the transport equation. Through the application of a continuous finite element (CFEM) spatial discretization, the matrices are symmetric positive definite (SPD), which allows for the use of solution techniques such as the preconditioned Krylov family of solvers [70]. The MOOSE framework uses CFEM as a spatial discretization and by default employs Jacobian-free Newton Krylov (JFNK) [86] with preconditioning as a nonlinear iterative solution method.

Through a straightforward algebraic technique, the phonon BTE may be manipulated into the SAAF formulation. Solving Eqn. (6) for $I(\mathbf{r}, \hat{\Omega})$ yields

$$I\left(\mathbf{r}, \mathbf{\Omega}\right) = I^0\left(\mathbf{r}, \mathbf{\Omega}\right) - \Lambda \mathbf{\Omega} \cdot \nabla I\left(\mathbf{r}, \mathbf{\Omega}\right). \tag{7}$$

Substituting Eqn. (7) back into Eqn. (6), distributing and collecting like terms gives the SAAF form of the EPRT. The self-adjoint component of Eqn. (8) is the second term, which contains a second-order operator and is symmetric positive definite:

$$-\mathbf{\Omega} \cdot \nabla\left[\Lambda \mathbf{\Omega} \cdot \nabla I\left(\mathbf{r}, \mathbf{\Omega}\right)\right] + \frac{1}{\Lambda} I\left(\mathbf{r}, \mathbf{\Omega}\right) = -\mathbf{\Omega} \cdot \nabla I^0\left(\mathbf{r}, \mathbf{\Omega}\right) + \frac{1}{\Lambda} I^0\left(\mathbf{r}, \mathbf{\Omega}\right). \tag{8}$$

From Eqn. (8), the change in the phonon intensity at a point has two contributions: a streaming term from the spatial variation in intensity, and a collision term due to

the deviation of the radiance from the equilibrium phonon radiance $I^0(\mathbf{r})$. Due to the implication of the SMRTA, the phonon radiative equilibrium intensity will be defined with a condition of zero heat generation, $\nabla \cdot \mathbf{q} = 0$. This suggests that a phonon radiative equilibrium could exist at all possible frequencies and provides some justification for the gray media formulation [85].

We employ two forms of boundary condition in this work: radiant emitting boundaries and reflecting boundaries. The angular phonon radiance at an emissive boundary may be defined as

$$I_b(r, \mathbf{\Omega}) = \frac{C_v v_g T_b}{4\pi}, \tag{9}$$

where T_b is a constant driving boundary temperature. For reflecting conditions, outgoing angular phonon radiance is defined as the reflection of the incoming angular phonon radiance, merely undergoing a directional change, i.e., $I(\mathbf{r}, \mathbf{\Omega}) = I(\mathbf{r}, \mathbf{\Omega}')$ where we map $\mathbf{\Omega}$ to $\mathbf{\Omega}'$.

The angular variable $\mathbf{\Omega}$ is discretized via the discrete ordinates method, sometimes referred to as the "S_N method". The transport equation becomes a set of N equations for the radiant intensity in each discrete angle. Solutions to the EPRT generate angular phonon radiative intensity, and Rattlesnake employs Level-Symmetric quadrature to numerically integrate this quantity over solid angle, to obtain "moments" of the radiance. The S_N method has advantages in heterogeneous media over the spherical harmonics method (P_N), in that the (P_N) angular moments are tightly coupled and their solution requires more computational resources [67]. The recent application of a hybrid $S_N - P_N$ scheme to discretize the angular variable in the frequency-dependent phonon BTE has been shown to exhibit slow convergence in homogeneous silicon [87] which suggests the P_N angular discretization approach may not be optimal for this type of problem.

The discrete ordinates SAAF transport equation has the feature that in each quadrature direction, a linear system of equations arising from the spatial discretization of an elliptic operator is solved for the angular intensity. This means that software for solving the diffusion approximation to transport can be readily converted to solve the transport equation. The treatment of voids and certain boundary conditions require special care, however. In contrast, the solution of the first-order form of the transport equation involves transport "sweeps" [67], where incident intensities from the problem boundary, and interior sources along the way, are propagated through the spatial mesh along the direction of travel to the exiting mesh boundary. The ordering of this mesh sweep is angle and problem dependent, and in multiple dimensions cyclic graphs are possible. Developing sweep algorithms that scale to large numbers of processors is an active research area, whereas efficient parallel solvers for elliptic equations are much more mature.

The zeroth angular moment of phonon radiance $I(\mathbf{r})$ is proportional to temperature, phonon speed, and volumetric specific heat capacity:

$$\int_{4\pi} I\left(\mathbf{r}, \mathbf{\Omega}\right) d\Omega = \frac{C_v v_g T}{4\pi}. \tag{10}$$

The first angular moment is the heat flux:

$$\mathbf{q}\left(\mathbf{r}\right) = \int_{4\pi} I\left(\mathbf{r}, \mathbf{\Omega}\right) \mathbf{\Omega} \, d\Omega. \tag{11}$$

Other researchers have taken different approaches to computing heat flux, incorporating quantities obtained through MD simulations (phonon group velocity, wave vectors, and angular frequencies [88–90]).

We compute an effective thermal conductivity by taking the ratio of the average heat flux to the end-to-end temperature gradient (which includes effects at the

boundaries) in the system

$$\langle \kappa_{\text{eff,z}} \rangle = \frac{\int \mathbf{e}_z \cdot \mathbf{q}\left(\mathbf{r}\right) d^3 r}{\int \mathbf{e}_z \cdot \nabla T\left(\mathbf{r}\right) d^3 r}. \tag{12}$$

Though heat flux and temperature gradient are computed over the entire domain, the dimension of interest is one where a temperature gradient is applied. This methodology is used in MD simulations and is repeated here.

2.3.3 A Test Problem

To evaluate the effectiveness of Rattlesnake as a deterministic transport engine, we compared our numerical solutions of temperature and thermal conductivity in room temperature, homogeneous silicon to the work of Yilbas and Bin Mansoor, who performed deterministic phonon transport simulations in silicon under equivalent conditions [1]. They used a forward and backwards finite difference discretization scheme to solve the BTE for phonons.

Yilbas and Bin Mansoor modeled a thin film of silicon, a common configuration which is used in many phonon transport simulations (with both deterministic and Monte Carlo methodologies) as a benchmark problem. Material properties of room temperature silicon are well known and transport behavior at the nanoscale has been studied [85]. Material properties for this model were obtained from the open literature [7, 85], and are listed in Table 2.1.

We construct a finite element mesh for a cube of silicon with side lengths of 3Λ (equivalent to 3 acoustic lengths) using CUBIT [91] with both a coarse and fine mesh of 1000 and 12000 hexahedral elements, respectively. We apply a temperature difference of 1 K to the yz planar boundaries to simulate phonon emission sources and placed reflecting boundary conditions on the remaining planes. We define the

Table 2.1: Silicon material data

Parameter	Value
$C_v \left(\text{J} \cdot \text{m}^{-3} \cdot \text{K}^{-1} \right)$	$1.653 \cdot 10^6$
$v_g \ (\text{m} \cdot \text{s}^{-1})$	8430
$\Lambda \ (\text{m})$	$33.9 \cdot 10^{-9}$
$T_\text{L} \ (\text{K})$	301
$T_\text{R} \ (\text{K})$	300

non-dimensional temperature Θ as:

$$\Theta = \frac{T\left(x\right) - T_\text{R}}{T_\text{L} - T_\text{R}}. \tag{13}$$

We use the generalized minimum residual (GMRES) [92] method preconditioned with algebraic multigrid (AMG) [93] to solve the linear system, with an iterative convergence criteria of $\epsilon = 10^{-6}$, and an S_8 angular quadrature. Computation times for coarse and fine mesh cases were approximately 8 and 57 seconds each. Simulations were performed on a single core 2.8 GHz Intel i7 CPU with 16 GB RAM. The coarse and fine mesh solutions are within 10^{-5} of each other; for simulations of homogeneous media it may be appropriate to use a more coarse spatial mesh to decrease computation time. The behavior of the non-dimensional temperature solution for coarse and fine mesh cases obtained with Rattlesnake agree well with those from Yilbas and Mansoor, shown in Fig. 2.1. The temperature profile has a slight curvature, which is influenced by spatial discretization. Improperly scaled finite elements do not produce the desired solution behavior. As the acoustic thickness increases, phonon scattering regimes shift from ballistic to diffuse. In an acoustically thin medium, where $L \approx \Lambda$, phonons leaving a colder boundary are in the ballistic scattering regime, and propagate far across the medium to reach the
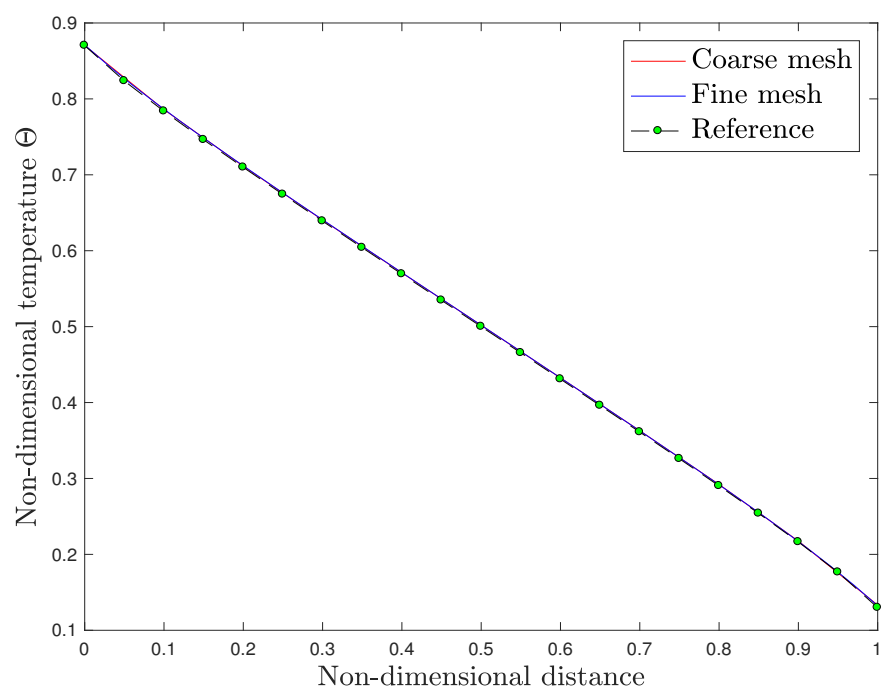
Figure 2.1: Comparison to reference [1] for silicon test problem. Coarse and fine meshes give nearly identical solutions.

hotter boundary causing the material temperature to be smaller than that associated with the prescribed incident intensity. In an acoustically thick medium, where phonons are in the diffuse scattering regime, this effect is significantly diminished. These are boundary scattering effects, and are well characterized in simulations of phonon transport [1, 85].

2.4 Uranium Dioxide with Xenon Bubble

Du et al. [3] investigated the effects of xenon presence on thermal conductivity of UO_2. MD methods were used to simulate the effect of various concentrations and geometric configurations of xenon in the UO_2 lattice for a range of temperatures. They concluded that randomly dispersed xenon in the fuel matrix has a more significant impact on thermal conductivity than quantized xenon bubbles. At higher temperatures, phonon-phonon scattering from normal and Umklapp processes becomes a main contributor to the suppression of thermal conductivity, and heat transport is locally disrupted at the xenon defect. The phonon mean free path (Λ) in UO_2 becomes shorter at high temperature and diffuse scattering dominates. Xenon concentration was limited to about 1% of volume in the simulations.

We model a selected problem from Du et al., computing temperature, heat flux and thermal conductivity in a cell of UO_2 with a bubble of xenon in the center, in the absence of grain boundaries. The behavior of xenon in a UO_2 lattice at high temperature and pressures has been reported to vary widely, and available experimental data is minimal. Computational studies have been performed to investigate expected temperatures and pressures of xenon using various methodologies which drew varying conclusions [94–96]. We performed MD simulations to determine the properties of xenon at specific pressure and temperatures; these data are used to

compute Λ in the bubble. Bates [2] performed thermal conductivity measurements on stoichiometric, unirradiated UO_2 for a large array of temperatures. We extract Λ from measured thermal conductivity in the Bates study, and perform simulations using the same bubble geometry to determine the impact of xenon on κ using values of Λ from Bates. We compare these results to the bulk κ of pristine UO_2 measured by Bates, and to κ computed using parameters from Du et al.

The role of thermal boundary resistance at the UO_2-Xe interface is investigated, as incoming delocalized waves may reflect diffusely or specularly off the xenon bubble and have a significant effect on the local thermal conductivity. We introduce the diffuse mismatch model and present a method to characterize thermal boundary resistance at heterogeneous defects in 3D.

2.4.1 Problem Description

We use Rattlesnake to simulate phonon transport in a cell of UO_2 with a xenon bubble in the cell center and no grain boundaries. The spatial domain $\mathcal{D}$ is a rectangular cell, 25 nm along the z-axis with a cross section of 3.8 nm by 3.8 nm, consistent with the geometry used by Du et al. The xenon bubble has a radius of 1 nm and accounts for approximately 1% of the total volume. The finite element geometry is constructed with CUBIT, an unstructured mesh consisting of 100689 tetrahedral elements (Fig. 2.2). The linear system is solved with the AMG-preconditioned GMRES method with convergence criteria of $\epsilon = 10^{-6}$. We performed simulations with an angular quadrature order of S_{30}, a large amount of ordinates helps to mitigate ray effects [74], which are can occur in deterministic phonon transport simulations.

Du et al. reported κ in UO_2 with Xe at 300 K, 800 K and 1500 K. Where possible,

we replicate their simulation conditions and report dimensionless temperature, heat flux and thermal conductivity. We extract Λ from values of thermal conductivity for unirradiated UO_2 as documented by Du et al. In each simulation, a 1 K temperature difference is applied along the z-axis. We use the same mesh to perform additional simulations for different values of temperature using Λ extracted from experimental values of thermal conductivity measured by Bates [2]. Simulations using the mean free path from Bates are performed independently the Du et al. simulations in order to gain insight into the effect Λ has on overall heat flux, temperature gradient and thermal conductivity.

2.4.2 Material Properties

The only materials property entering into the gray BTE in Eqn. (8) is the phonon mean free path, Λ, and so we need to determine these for UO_2 and Xe. However, it is also necessary to determine each material's phonon radiance, $I^0(T)$, as a function of temperature in order to impose the correct scalar flux at the external boundaries, and to set the transmission coefficients at the internal boundary.

To set the effective mean free path for the gray phonons in both the UO_2 and Xe we use the standard kinetic equation for thermal conductivity [11]:

$$\kappa = \frac{1}{3}C_v v_g \Lambda. \tag{14}$$

For the UO_2, v_g, and C_v of acoustic modes are computed from first principles calculations and then Λ is chosen so as to reproduce the experimentally measured values of κ in unirradiated UO_2 [2]. The calculation of v_g and C_v in UO_2 is described in detail in the next section. For Xe the κ, v_g, and C_v are computed from classical molecular dynamics simulations, and similarly used to infer Λ in the Xe.

The effective group velocity and effective mean free path of the gray phonons were assumed to be isotropic in both the UO_2 and the Xe. In order to understand the degree to which transport is ballistic in ether region we consider the *acoustic thickness*, ζ, in each domain. This is the domain size scaled by the material's effective phonon mean free path. Acoustic thickness of UO_2 is the ratio $\zeta_{UO_2} = \frac{\mathcal{D}_{UO_2,z}}{\Lambda_{UO_2}}$, where $\mathcal{D}_{UO_2,z}$ is the distance between the hot and cold sides of the UO_2 cell. Similarly, the acoustic thickness of the Xe, $\zeta_{Xe} = \frac{\mathcal{D}_{Xe}}{\Lambda_{Xe}}$, describes the diameter of the bubble relative to the effective (gray) phonon mean free path in Xe; acoustic data and mean free path for simulations using values from Du et al. are contained in Tab. 2.2.

The transport properties of Xe are strongly tied to the Xe pressure, which in turn is set by the surface tension of the UO_2/Xe interface and the bubble size. In a 2 nm diameter bubble of Xe in UO_2 the pressure is estimated to be between 2-5 GPa, and so in this work the Xe pressure was assumed to be 3 GPa at all temperatures studied. At this pressure Xe is either solid or liquid across the temperature range that we study here and so the use of a gray phonon model of transport is justified in the Xe. Across the range of temperatures we study we hold the size of the bubble fixed (with radius of 1 nm), meaning that as the temperature is changed the number of Xe atoms in the bubble is not constant. This means that our sweep of simulations does *not* represent the change in thermal conductivity due to heating UO_2 containing Xe bubbles from 300 to 1500 K. However, it does provide us insight into the ballistic versus diffusive contributions to thermal resistance from 1 nm bubbles at different temperatures.
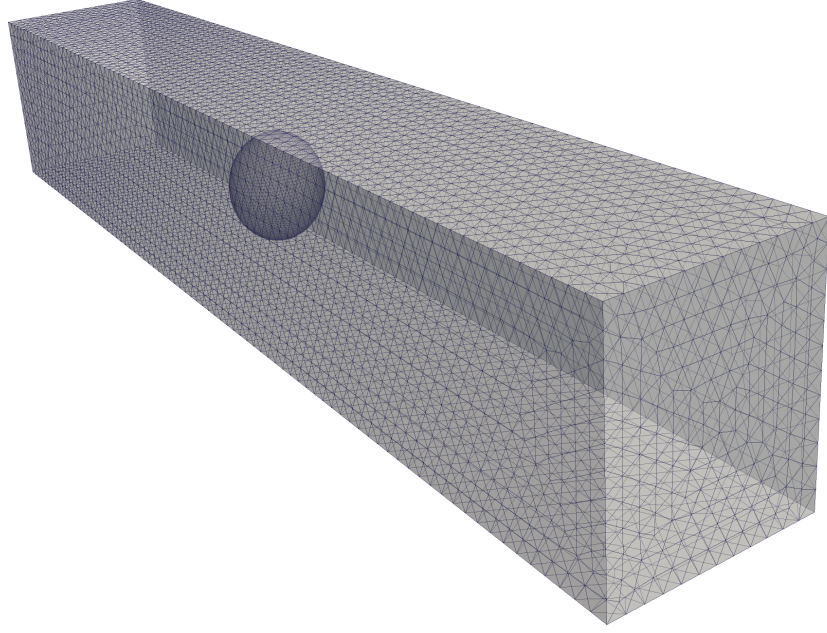
Figure 2.2: 25 nm cell of UO_2 with xenon bubble; 100379 tetragonal mesh elements.

2.4.3 UO_2 Calculations

For UO_2, the effective group velocity, volumetric specific heat, and radiance of gray phonons was computed by averaging the properties of the three acoustic branches of the phonon dispersion over the entire Brillouin zone. The phonon dispersion was computed on a $50\times50\times50$ q-point grid using Phonopy [97] based on the structure symmetry of UO_2 (Fd-3m) with interatomic force constants computed from first principles. The UO_2 simulations were executed with the plane-wave basis projector augmented wave method within the density functional theory framework as implemented in the Vienna *Ab-initio* Simulation Package (VASP) [98–100]. A plane-wave energy cutoff of 600 eV was employed in the local density approximation (LDA) [101], with a $6\times6\times6$ Monkhorst-Pack k-point grid. A $2 \times 2 \times 2$ super-cell of the UO_2 unit cell (with 4 O and 8 U atoms) was used for all calculations, including

calculation of the force constants. The perfect super-cell was found to be relaxed to a 1×10^{-3} eV/Å ionic tolerance and a 1×10^{-5} eV electronic tolerance. UO_2 is anti-ferromagnetic, but there exist ferromagnetic solutions to the Kohn–Sham equation and VASP can get trapped into a ferromagnetic state. To prevent this from happening, the MAGMOM tag was selected to ensure that alternating uranium atoms in the structure had opposing spins, and the spin of the oxygen atoms was set to zero. We further used a Hubbard parameter, U, of 4.50 eV, and a Hund's exchange parameter, J, of 0.50 eV. The resulting electronic density of states (Fig. 2.3) agrees with that of Wang et al. [102]. The phonon dispersion (Fig. 2.4), also in good agreement with that obtained in the same reference [102].

The effective transport properties of the gray phonons in UO_2 were computed from the following expressions:

$$I^0(T) = \frac{1}{4\pi} \times \sum_{p=1}^{3} \int_{BZ} dk^3 \frac{|\mathbf{v_g}(p, \mathbf{k})|}{2\pi^3 a^3} \hbar\omega(p, \mathbf{k}) \, n_{BE}(\omega(p, \mathbf{k}), T), \qquad (15)$$

where $n_{BE}(\omega, T)$ is the Bose-Einstein distribution, a is the lattice parameter of UO_2, and p is the phonon polarization. The volumetric specific heat capacity is computed using a similar integral:

$$C_v = \frac{1}{2\pi^3 a^3} \times \sum_{p=1}^{3} \int_{BZ} dk^3 \, \hbar\omega(p, \mathbf{k}) \, \frac{\partial n_{BE}(\omega(p, \mathbf{k}), T)}{\partial T}. \qquad (16)$$

Using these integrated quantities we can define an effective group velocity for gray phonons as:

$$v_g(T) = \frac{4\pi I^0(T)}{C_v T}. \qquad (17)$$

This velocity and the heat capacity are only very weakly temperature dependent over the temperature range of interest and thus we approximate it by their average values of $1764 \, \mathrm{m \cdot s^{-1}}$ and $1.007 \times 10^6 \, \mathrm{J \cdot m^{-3} \cdot K^{-1}}$, respectively. Note that this

effective velocity of the gray phonon bath is approximately 0.45 of the mean speed of sound obtained from the same UO_2 calculations. It is in effect the average group velocity of acoustic phonon modes weighted by the thermal energy in the mode. Similarly the *effective* specific heat is not the true specific heat of UO_2, but only the contribution to its specific heat from the acoustic modes and the computed value for this is is close to the high temperature limit for the acoustic modes of $12k_B/a^3$.
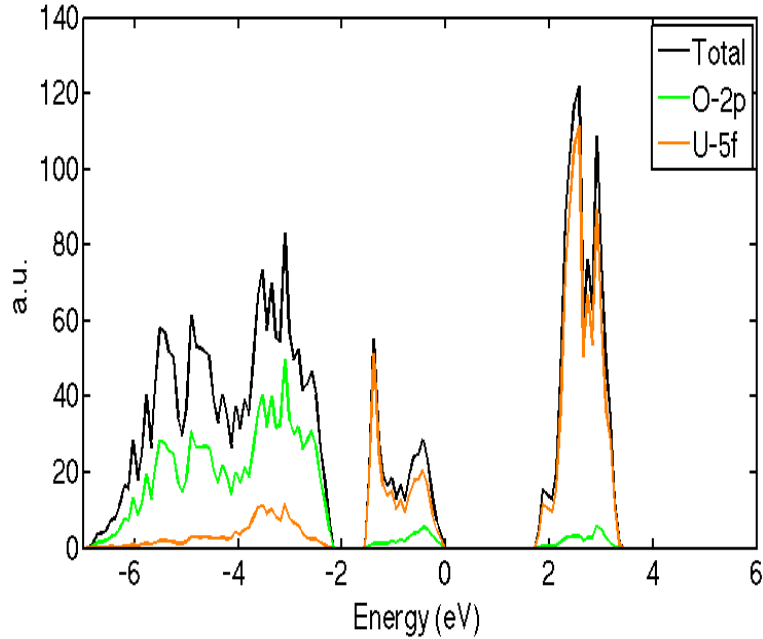
Figure 2.3: Total and partial (for the orbitals listed in the legend) electronic density of states for UO_2 with U correction.

2.4.4 Xenon Calculations

The thermal conductivity and transport properties of xenon under high pressure were computed from classical molecular dynamics simulations performed using the LAMMPS package [103]. Interatomic forces were modeled using a Lennard-Jones potential with LAMMPS parameters $\epsilon = 0.00425\,\text{eV}$ and $\sigma = 4.29\,\text{Å}$, with all
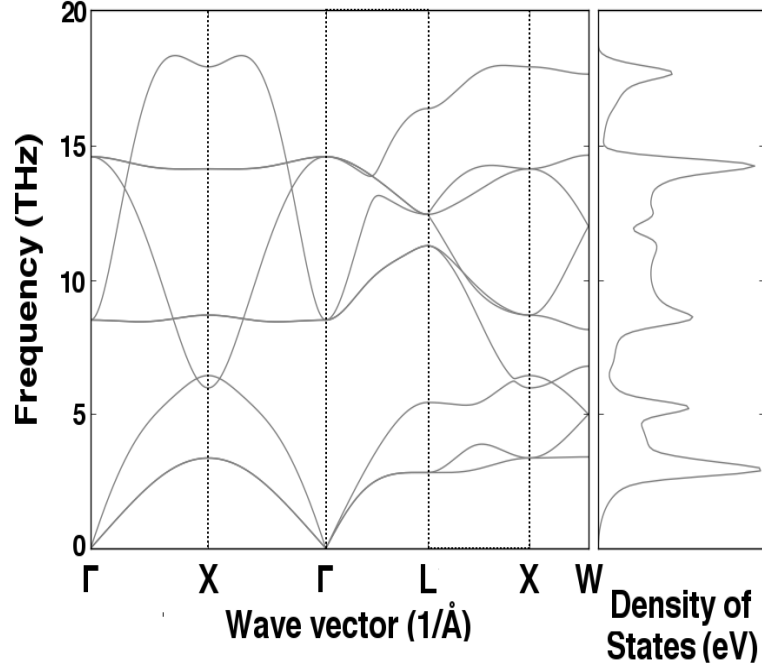
Figure 2.4: Phonon dispersion relations for UO_2.

interactions truncated after 20 Å.

Simulated systems of 10,000 Xe atoms under 3 GPa where prepared at a series of temperatures from 300 to 1700 K. This was achieved by equilibrating the system over a 500 ps simulation in the NPT ensemble before turning of the thermostat and barostat and simulating for a further 50 ps in the microcanonical ensemble. In these simulations it was found that the Xe was solid at temperatures below $\sim$ 600 K, and above that, remains liquid up to 1700 K. Once the systems were prepared, the system was simulated in for a further 1 ns in the microcanonical ensemble, during which the thermal conductivity was computed using the Green-Kubo method [104]. The Green-Kubo method is founded on the fluctuation dissipation theorem to determine the thermal conductivity of a system from the lifetime of its natural thermal fluctuations during a simulation of the system at equilibrium. A minimum

Table 2.2: Mean free path data for pristine UO_2 [3] and Xe (this work)

T (K)	Λ_{UO_2} (nm)	Λ_{Xe} (nm)	ζ_{UO_2}	ζ_{Xe}
300	31.9	1.10	0.78	1.82
800	14.3	0.77	1.75	2.6
1500	7.6	0.8	3.3	2.5

of six simulations were performed using different random starting configurations and the results averaged to obtain each thermal conductivity datum.

For v_g of Xe we use the speed of sound computed at each temperature from the Xe's density and isentropic compressibility. The isentropic compressibility was computed by simulating adiabatic expansion. At each temperature the system was first cycled in an NVE ensemble after which system dimensions were slightly increased, followed by another NVE cycling step. The compressibility was calculated from the differences in systems volume and pressure before and after expansion. This set of simulations also served as the source of density data. The Xe density was also used to compute Xe's volumetric specific heat capacity at each temperature.

The computational approach for determining both thermal conductivity and speed of sound where validated by computing the pressures at slightly lower pressures for which there exists experimental data [105] and finding the properties to be in reasonable agreement. The computed density, thermal conductivity, v_g, and Λ_{Xe} are plotted in Fig. 2.5, and clearly show a transition in properties between the solid and liquid Xe.
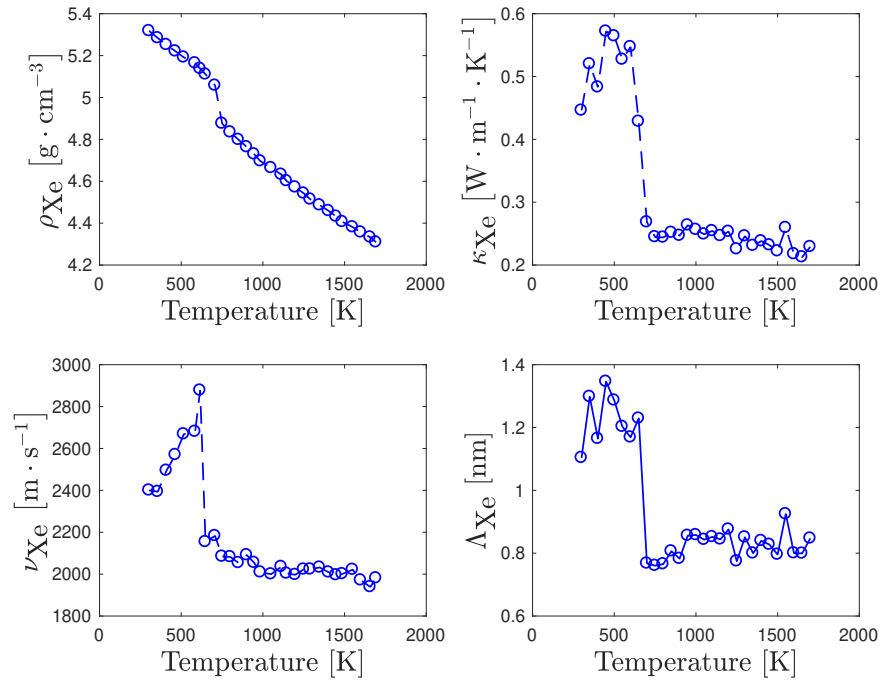
Figure 2.5: Xenon properties from MD simulations. Clockwise from top left: density, thermal conductivity, mean free path, phonon speed. Xenon experiences a phase change with increasing temperatures.

2.4.5 Thermal Boundary Resistance

We must consider the resistive effect at material interfaces, the phenomenon of thermal boundary resistance (TBR), the ratio of a temperature discontinuity at an interface to the heat flux across that interface, due to a material difference at the junction. TBR is an extraordinarily subtle phenomenon and has some consideration in other deterministic phonon transport studies [106, 107]. However, it is very important to consider in simulating phonon transport, and has been characterized in a number of other MD and MC studies [48, 50, 53].

The physics of TBR are important to phonon transport because of how phonons behave when they encounter a physical interface between two adjacent materials. At this junction, phonons become subject to a phenomenon which manifests as a transmissive and resistive effect for phonons penetrating an interface into another material. This physical effect occurs as the intrinsic properties of material change. Phonons define the internal energy of a material; when they cross a boundary from one material into the next, the change in their contribution to internal energy as well as change in their velocity must be considered.

We develop the diffuse mismatch model (DMM) [108] in a deterministic framework for 3D general geometries. We assume all phonons are diffusely scattered at the interface, with outgoing radiance emitted isotropically, and that scattering destroys the correlation between the wavevectors of incident and outgoing phonons; the probability that a phonon will scatter into a given side of the interface is independent of the phonon origin. Enforcing these conditions makes the probability of scattering into a given side proportional to the phonon density of states on that side, additionally constrained by the principle of detailed balance.

We can write a balance equation for the flow of phonons between two materials

$$U_\alpha v_{g,\alpha} T_{\alpha \to \beta} = U_\beta v_{g,\beta} T_{\beta \to \alpha}, \tag{18}$$

where U_α, U_β, $v_{g,\alpha}$, $v_{g,\beta}$ are internal energies and phonon speeds of materials α and β, respectively. We define $T_{\alpha \to \beta}$ as the probability of transmission from material α into material β, and $T_{\beta \to \alpha}$ as the probability of transmission from material β into material α. It follows that

$$T_{\alpha \to \beta} + T_{\beta \to \alpha} = 1, \tag{19}$$

to uphold conservation of energy and detailed balance. We solve for the transmission probabilities, which are

$$T_{\alpha \to \beta} = \frac{U_\beta v_{g,\beta}}{U_\alpha v_{g,\alpha} + U_\beta v_{g,\beta}} \tag{20}$$

$$T_{\beta \to \alpha} = \frac{U_\alpha v_{g,\alpha}}{U_\alpha v_{g,\alpha} + U_\beta v_{g,\beta}}, \tag{21}$$

it follows that the probabilities of reflectance are defined as $R_{\alpha \to \alpha} = 1 - T_{\alpha \to \beta}$ and $R_{\beta \to \beta} = 1 - T_{\beta \to \alpha}$, where $R_{\alpha \to \alpha}$ is the reflectance of phonons in material α incident on the interface back into material α, and $R_{\beta \to \beta}$ is the reflectance of phonons in material β incident on the interface back into material β.

We take the first order form of the steady-state, one-speed phonon transport equation to derive balance relations for phonons incident on and leaving a spatially discontinuous interface

$$\mathbf{\Omega} \cdot \nabla I\left(\mathbf{r}, \mathbf{\Omega}\right) + \frac{1}{\Lambda} I\left(\mathbf{r}, \mathbf{\Omega}\right) = \frac{1}{\Lambda} I^0\left(\mathbf{r}\right). \tag{22}$$

In Fig. 2.6 we denote "-" as the upwind radiant flux and "+" as the downwind radiance. The scalar radiance is identified by $I_{\alpha;\beta}^{\pm}\left(\mathbf{r}_{\text{int}}\right)$. We must solve for the upwind and downwind scalar radiance at the interface $\mathbf{r}_{\text{int}}$ to characterize the effects
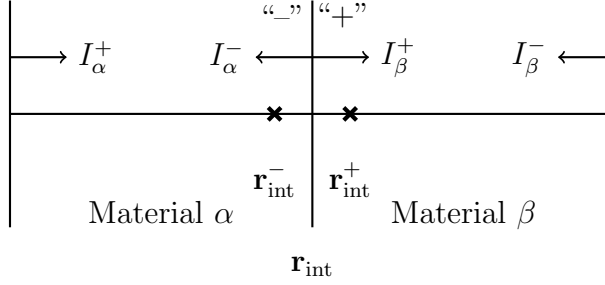
Figure 2.6: Upwind and downwind phonon radiance at a physical interface between two materials

of TBR in our transport simulation. In the transport equation we solve for the angular radiance, which is integrated over solid angle to solve for scalar radiance.

At the location $\mathbf{r}_{\text{int}}$ with its unit vector normal to the interface which points from material α to material β denoted as $\mathbf{n}_{\alpha\to\beta}$, we can write conservation equations which define the flow of phonons immediately at both sides of the interface. On the β side of the interface, phonons which flow away from the interface into material β come from two sources: they are transmitted through the interface from material α, and reflected from those incident on the surface from the β side.

On the β side of the interface, each angular radiance corresponding to a particular ordinate $\mathbf{\Omega}_m$ is assigned the new diffuse flux, an angular redistribution of the transmitted portion of phonons from side α and reflected phonons from side β. This diffuse flux is now the effective source of phonons flowing away from the interface into material β. An analogous procedure holds for phonons flowing into material α. We identify the new flux with its contributions from α and β side phonons as $I_{\alpha;\beta}\left(\mathbf{r}_{\text{int}}^{\pm}\right)$. The conservation equation expressing the flow of phonons away from the interface into material α is then developed as

$$\int_{\mathbf{n}_{\alpha\to\beta}\cdot\hat{\Omega}>0} I\left(\mathbf{r}_{\text{int}}^+, \boldsymbol{\Omega}\right) \left|\mathbf{n}_{\alpha\to\beta}\cdot\boldsymbol{\Omega}\right| d\Omega =$$

$$I_\beta\left(\mathbf{r}_{\text{int}}^+\right) \int_{\mathbf{n}_{\alpha\to\beta}\cdot\boldsymbol{\Omega}>0} \left|\mathbf{n}_{\alpha\to\beta}\cdot\boldsymbol{\Omega}\right| d\Omega =$$

$$T_{\alpha\to\beta} \int_{\mathbf{n}_{\alpha\to\beta}\cdot\boldsymbol{\Omega}>0} I\left(\mathbf{r}_{\text{int}}^-, \boldsymbol{\Omega}\right) \left|\mathbf{n}_{\alpha\to\beta}\cdot\boldsymbol{\Omega}\right| d\Omega$$

$$+ R_{\beta\to\beta} \int_{\mathbf{n}_{\alpha\to\beta}\cdot\boldsymbol{\Omega}<0} I\left(\mathbf{r}_{\text{int}}^+, \boldsymbol{\Omega}\right) \left|\mathbf{n}_{\alpha\to\beta}\cdot\boldsymbol{\Omega}\right| d\Omega, \quad (23)$$

such that we solve for the downwind diffuse radiance flowing into material β from material α,

$$I_\beta\left(\mathbf{r}_{\text{int}}^+\right) = \frac{1}{\int_{\mathbf{n}_{\alpha\to\beta}\cdot\boldsymbol{\Omega}>0} \left|\mathbf{n}_{\alpha\to\beta}\cdot\boldsymbol{\Omega}\right| d\Omega} \times$$

$$\left[T_{\alpha\to\beta} \int_{\mathbf{n}_{\alpha\to\beta}\cdot\boldsymbol{\Omega}>0} I\left(\mathbf{r}_{\text{int}}^-, \boldsymbol{\Omega}\right) \left|\mathbf{n}_{\alpha\to\beta}\cdot\boldsymbol{\Omega}\right| d\Omega\right.$$

$$\left.+ R_{\beta\to\beta} \int_{\mathbf{n}_{\alpha\to\beta}\cdot\boldsymbol{\Omega}<0} I\left(\mathbf{r}_{\text{int}}^+, \boldsymbol{\Omega}\right) \left|\mathbf{n}_{\alpha\to\beta}\cdot\boldsymbol{\Omega}\right| d\Omega\right]. \quad (24)$$

A similar expression describes the upwind diffuse radiance of phonons flowing from material β into material α. These new expressions for the scalar radiance are now the isotropic emission sources on either side of the interface and are distributed at each direction of outgoing angular radiance at the interface $I_{\alpha;\beta}\left(\mathbf{r}_{\text{int}}^\pm, \boldsymbol{\Omega}\right)$.

The effective implementation of this model allows for the description of localized heat flux and temperature around defects in heterogeneous structures. The DMM is a relatively crude descriptor of TBR, an improved model of interface physics would necessitate the inclusion of anharmonic effects, and would also need to be
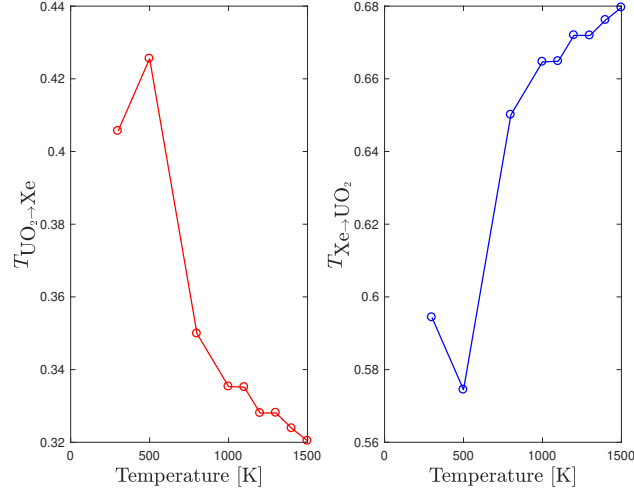
Figure 2.7: Transmission coefficients $T_{\mathrm{UO_2 \to Xe}}$ and $T_{\mathrm{Xe \to UO_2}}$ as functions of material properties U, v_g for 300 to 1500 K.

adaptive to phonon frequency selection over the interface itself [109]. We computed transmission and reflection coefficients for UO_2 and Xe from the material properties determined in Sec. 2.4.3 and 2.4.4; these are shown in Fig. 2.7. At all temperatures the phonon radiance is approximately two orders of magnitude larger in the UO_2 than in the Xe; the boundary is highly resistive to phonons flowing from UO_2 into the Xe bubble with approximately 40% transmitted at 300 K, decreasing sharply as temperature increases.

2.4.6   Results and Discussion

We report simulated heat flux and thermal conductivity for an array of temperatures with two sets of values for $\Lambda_{\mathrm{UO_2}}$; one generated from the MD results of Du et al. (denoted Λ_{Du}), the other extracted from experimentally measured values of κ in unirradiated samples of UO_2 from Bates (denoted Λ_{Bates}). In both cases we use material properties for Xe based on MD simulations we performed, as well as the

same spatial mesh. We observe the effects of thermal boundary resistance at the Xe bubble, which play a role in the amount of overall thermal resistance the bubble provides. In all cases, the presence of xenon lowers the thermal conductivity in the UO_2.

Figure 2.8 shows all values of simulated κ and the measured pristine κ. In the upper half of Fig. 2.8 we compare to Bates and follow a similar trend showing decreased thermal conductivity with increasing temperature. This is further affected by the presence of the xenon bubble; κ is reduced by approximately $30 - 55$ % over the temperature range with the sharpest difference occurring at lower temperature.

In the lower half of Fig. 2.8 we compare our κ to that of Du et al.; while we follow a loose trend in the shape of the curve, we experience a large discrepancy in simulated values. We under-predict κ in simulations with and without a Xe bubble, which may have multiple causes. Our computed group velocity in UO_2 is lower by approximately a factor of 2 compared to Du et al.; it is no surprise that our κ with Xe is also lower by approximately the same factor. We justify this exclusively for a gray approach in that we assume all phonons do not travel at the speed of sound in UO_2; indeed from the calculations in Sec 2.4.3 is it clear that group velocity is averaged, but has contributions from phonons with varying Λ lumped into a single term. Some phonon modes may be highly sensitive to frequency and this detail is washed out in the gray approach. This assumption may explain some of the underestimation in the ballistic effects. In addition, we may not be capturing some intrinsic phonon scattering, and we currently do not have anharmonicity built into the relaxation time; there is no way to discern these effects. The relaxation time τ_{eff} has many contributions; Umklapp processes, defect scattering, boundary scattering and the resonant scattering of phonons. Classic MD can be used to characterize

many of these processes, but MD is not able to capture certain quantum effects at low temperatures, such as specific heat [110], and this may be a reason for the discrepancy.
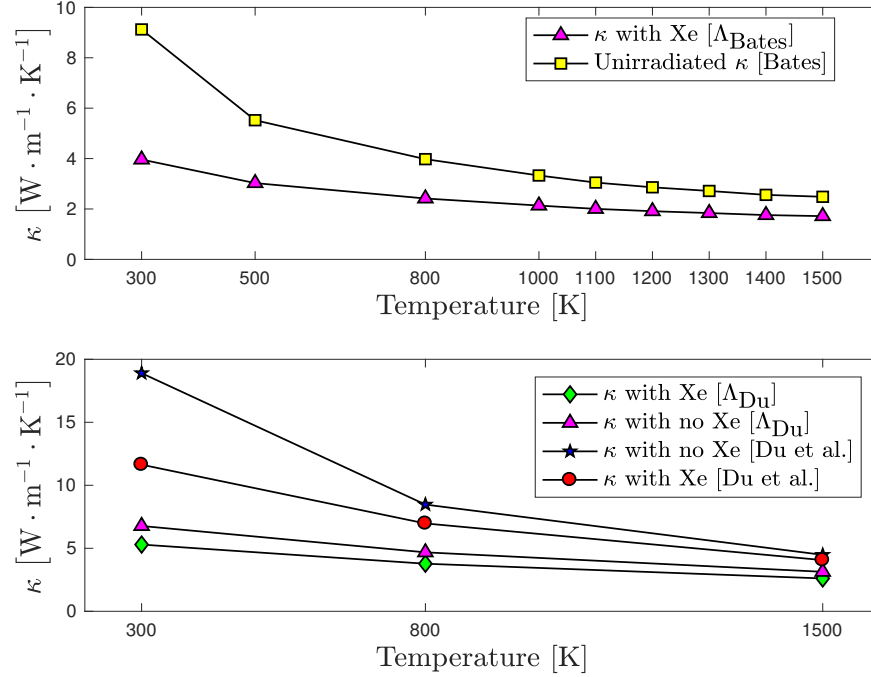
Figure 2.8: Upper plot: κ computed with Λ_{Bates}; magenta triangle – κ with xenon bubble; yellow square – κ from unirradiated UO_2 [2]. Lower plot: κ computed with Λ_{Du}; green diamond – κ with xenon bubble; magenta triangle – κ with no xenon; blue star – κ with no xenon [3]; red circle – κ with xenon bubble [3].

Dimensionless temperature for all simulated temperature is shown in Fig. 2.9. The influence of the xenon bubble is clear, jumps at the interface are observed; these are more pronounced at lower temperatures when phonon scattering is highly ballistic. This effect results in localized negative temperature gradients, which was also observed by Yang in Si nanowires [53], and the gradient monotonically shifts towards zero with increasing temperature. Note that while the temperature gradient becomes negative, the net flux in this region is still positive (see Fig. 2.10)

— heat is apparently flowing uphill. This result is counter intuitive when thinking of heat flow in the diffusive limit, but is entirely consistent with a ballistic picture of transport in which the energy of the phonon gas at any point contains non-local information.
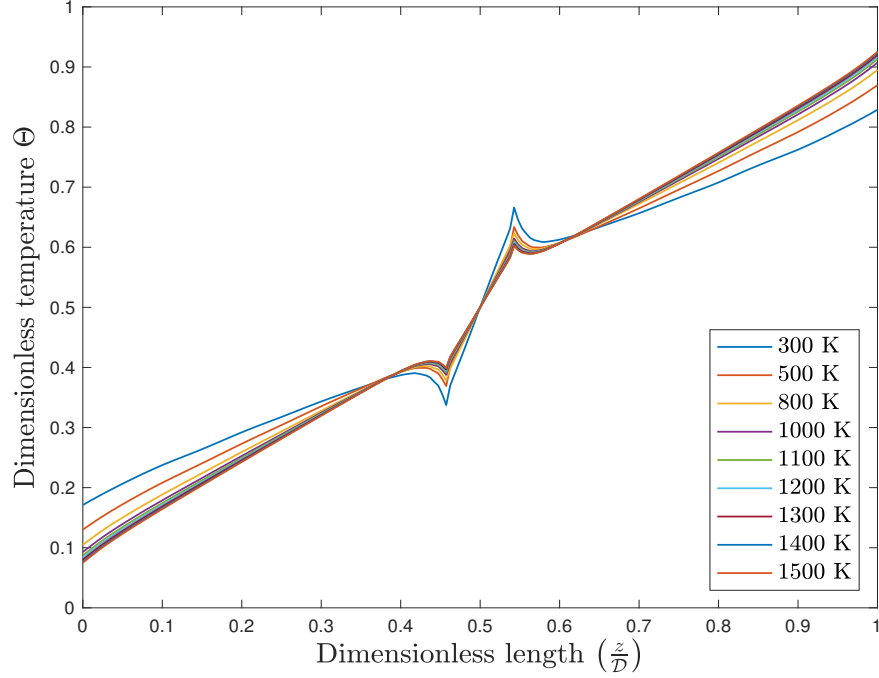
Figure 2.9: Dimensionless temperature Θ for all simulation temperatures. The presence of the xenon bubble is clear, as the gradient in the center region becomes steeper. This simulation was conducted using Λ_{Bates}.

The centerline heat flux $\mathbf{q}(\mathbf{r})$ shown in Fig. 2.10 has been normalized to the 300 K value; $\mathbf{q}(\mathbf{r})$ is inversely proportional to temperature and experiences a steady decline as temperatures increase. As temperature increases, Λ_{UO_2} decreases and diffuse scattering becomes more prevalent, which contributes to the reduction in heat flux. As a result of TBR, large portions of the phonon radiance are reflected at the xenon bubble, decreasing local $\mathbf{q}(\mathbf{r})$ by resisting the flow of phonons.

Heat flux in the UO_2 region remains approximately constant along the tempera-

ture gradient and changes drastically at the Xe bubble. We observe this effect in Figs. 2.10 and 2.11, where heat flux is severely depressed in the region local to the Xe bubble. The presence of a single xenon bubble does not significantly impact average $\mathbf{q}\left(\mathbf{r}\right)$ in the domain, but it does affect the behavior of the local heat flux. Du et al. established this by performing MD simulations which include multiple Xe bubbles and Xe randomly dispersed in the UO_2 matrix [3]. Ray effects are observed at lower temperatures when phonon scattering is highly ballistic (slight oscillations in $\mathbf{q}\left(\mathbf{r}\right)$) but vanish as scattering becomes diffuse. With increasing temperature, the heat flux is gradually suppressed and the effects of Xe on the local heat flux become less significant. Λ_{UO_2} decreases by approximately a factor of 3 between the temperature extremes, and this decrease is more detrimental to heat flux than compared to the presence of a singular bubble of Xe. Additional Xe bubbles would have a greater negative effect on bulk thermal conductivity.

Table 2.4 contains the number of Richardson (source iterations) iterations required for convergence, and total acoustic thickness of the spatial domain over the range of temperatures. As ζ increases, required iterations decrease; this is counterintuitive as purely scattering thermal radiation and phonon transport simulations tend to require more iterations for convergence with increasing ζ. This effect is potentially related to the oscillations experienced in the ballistic scattering regime, where Λ is on the order of the entire spatial domain (Casimir limit).
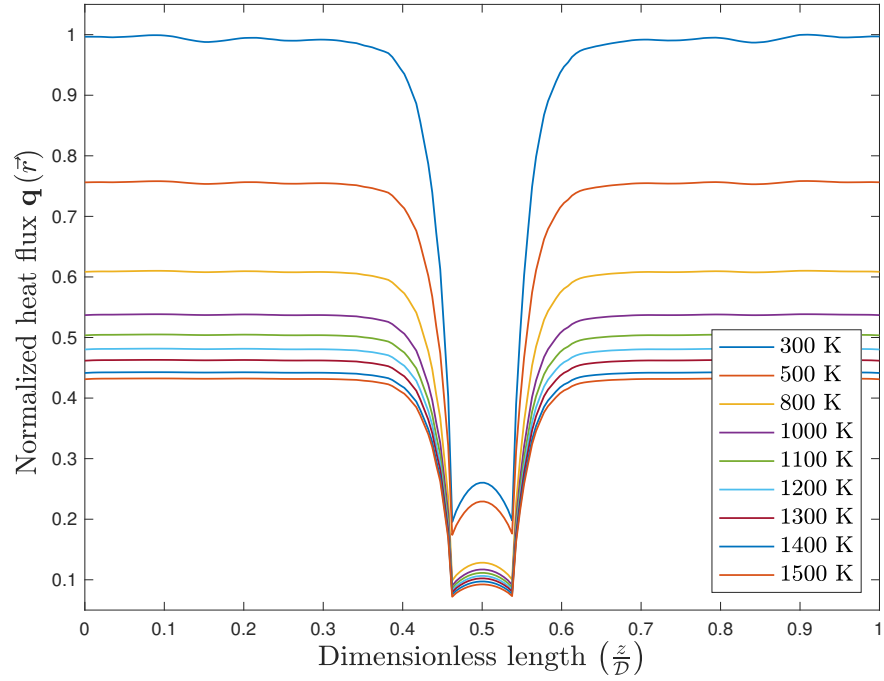
Figure 2.10: Heat flux along z-axis normalized to the 300 K value, which shows the presence of the xenon bubble and its effect on the local heat flux. Heat flux steadily decreases with increasing temperature as phonon transport becomes gradually more diffuse. This simulation was conducted using Λ_{Bates}.
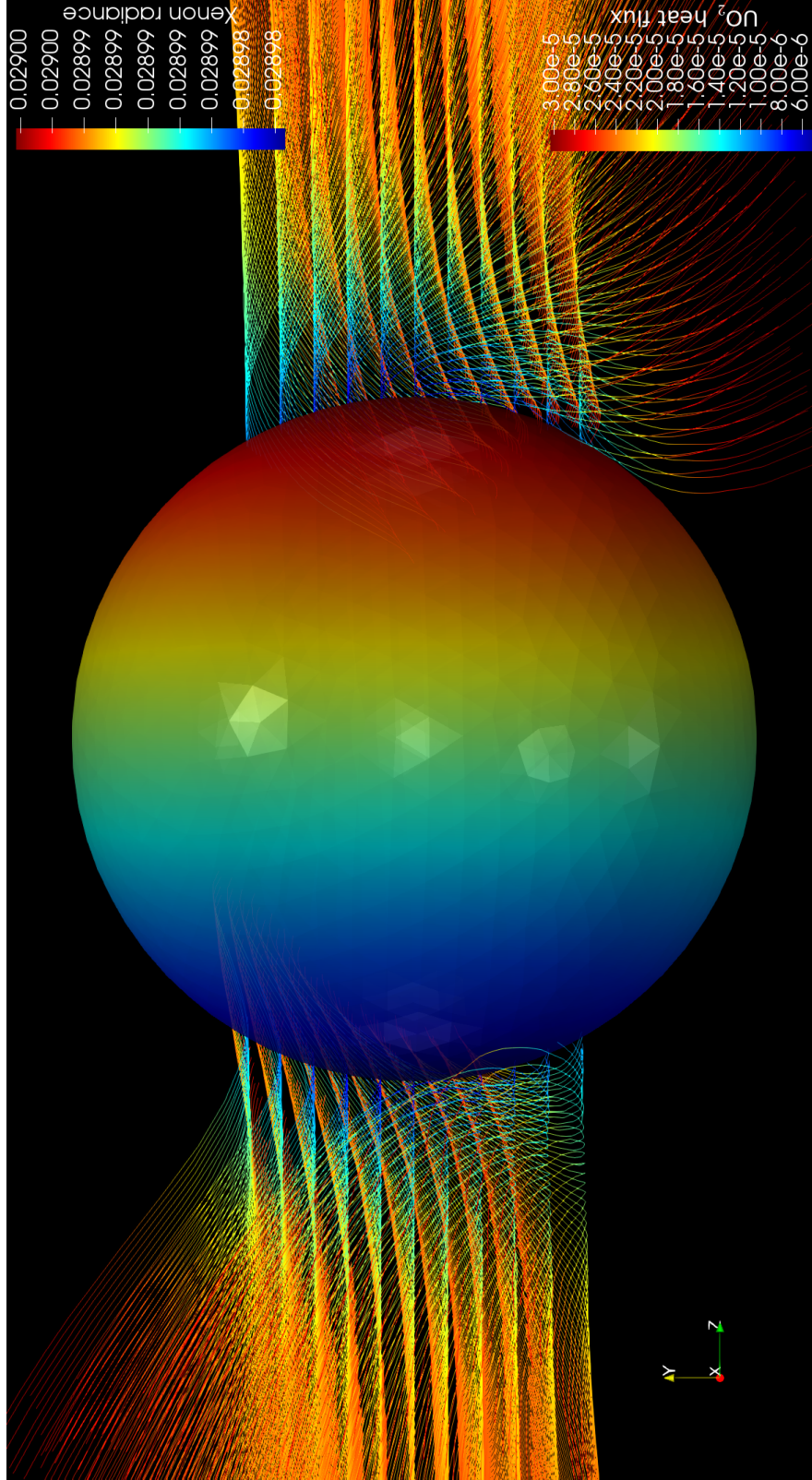
Figure 2.11: Phonon radiance (temperature) of the Xe bubble and streamlines of the heat flux in the UO_2 region at 300 K. Higher temperature phonons are incident on the right side of the bubble; the resistance encountered increases phonon scattering, which decreases heat flux at the interface. The opposite effect occurs on the left side of the Xe bubble, where heat flux is greater as colder phonons have decreased scattering and flow away from the bubbles.

Table 2.3: Thermal conductivity $\left(\mathrm{W} \cdot \mathrm{m}^{-1} \cdot \mathrm{K}^{-1}\right)$ simulated using $\Lambda_{\mathrm{UO_2}}$

$T\,(\mathrm{K})$	Pristine $\mathrm{UO_2}$ [3]	$\mathrm{UO_2 + Xe}$ [3]	$\mathrm{UO_2 + Xe}$
300	15.97	11.64	5.3
800	7.81	6.97	3.8
1500	4.29	4.06	2.6

Table 2.4: Iteration details: source iterations (SI) and acoustic thickness ζ for simulation using Λ_{Bates}.

$T\,(\mathrm{K})$	Source its.	$\zeta_{\mathrm{UO_2}} + \zeta_{\mathrm{Xe}}$
300	116	3.4
500	85	4.2
800	82	6.3
1000	76	6.8
1100	79	7.2
1200	77	7.5
1300	75	7.8
1400	75	8.2
1500	76	8.5

2.5 Conclusions

We have presented the features of a 3D, generalized geometry radiation transport code modified to simulate phonon transport in a gray formulation. We have implemented the physics for thermal boundary resistance in 3D to describe phonon transport behavior at localized defects in the material. We have presented our deterministic transport results for a simulation of a 3D domain of UO_2 with a Xe impurity and compared them against MD results for similar geometry and simulation parameters [3]. Additionally, we use Λ_{UO_2} extracted from experimentally measured pristine UO_2 for the same simulation setup, and mimic the shape of the κ curve in Bates [2] but with lower values of κ due to the Xe presence.

The transport method we have presented is trivially extendable to simulate a multi-frequency phonon spectrum using input variables derived from DFT simulations, consistent with our discussion in this present work (Sec. 2.4.3 and 2.4.4). The use of deterministic methods to simulate phonon transport is an underdeveloped aspect of the phonon transport community. Classical molecular dynamics simulations and DFT electronic structure calculations can provide detailed information about material properties, dispersion relations, and thermal conductivity but do so only at a local or nanometer scale. It is well understood that resistive processes also arise from the mesoscale structure of materials and these cannot be captured efficiently from atomistic calculations (a point that is reinforced by the results in this work).

By coupling Rattlesnake to MD and DFT methodologies, we show a way to bridge the gap between the atomistic and engineering scales. This multiscale method provides a framework for rapid prediction of the engineering scale thermal conductivity in materials with evolving microstructures. Such a tool is particularly

imperative for modeling nuclear fuels and their surrounding structural materials in which the thermal conductivity of the materials is a central component of the system performance.

2.6 Acknowledgements

3   Prediction of Thermal Conductivity in Dielectrics using Fast, Spectrally-resolved Phonon Transport Simulations

Jackson R. Harter, Aria S. Hosseini, Todd S. Palmer, P. Alex Greaney

3.1 Abstract

We present a new method for predicting effective thermal conductivity (κ_{eff}) in materials, informed by *ab initio* material property simulations. Using the Boltzmann transport equation in a self-adjoint angular flux formulation, we performed simulations in silicon at room temperatures over length scales varying from 10 nm to 10 μm and report temperature distributions, spectral heat flux and thermal conductivity. Our implementation utilizes a Richardson iteration on a modified version of the phonon scattering source. In this method, a closure term is introduced to the transport equation which acts as a redistribution kernel for the total energy bath of the system. This term is an effective indicator of the degree of disorder between the spectral phonon radiance and the angular phonon intensity of the transport system. We employ polarization, density of states and full dispersion spectra to resolve thermal conductivity with numerous angular and spatial discretizations.

3.2 Introduction

In many applications a material's propensity for conducting heat is an important factor in its overall performance. For thermal management applications, having high or low thermal conductivity is of principal importance, but thermal conductivity makes an auxiliary contribution to a material's figure of merit in many other applications such as batteries, high frequency electronics, and thermoelectric materials.

In order to accelerate the discovery, design, and selection of application-driven materials, it is desirable to efficiently compute a thermal conductivity from first principles. The past decade has seen considerable progress towards this goal in semiconductors and ceramics, where heat transport is dominated by phonons [111,

112]. Methods have been developed which make routine the computing of second order interatomic stiffness matrices of a crystal from density functional theory (DFT) calculations, and from them, the phonon dispersion [35, 36, 39, 40, 113, 114]. More recently, methods have been developed for computing third and fourth order stiffness matrices from which the rates of intrinsic three- and four-phonon scattering processes may be derived. The use of these methods is becoming commonplace, as together they enable one to compute the intrinsic phonon thermal conductivity, κ, using the equation derived from the Boltzmann transport equation for a phonon gas:

$$\kappa = \frac{1}{8\pi^3} \sum_p \int_{\mathrm{BZ}} \tau_{p\mathbf{k}} \mathbf{v}_{p\mathbf{k}} \otimes \mathbf{v}_{p\mathbf{k}} \omega_{p\mathbf{k}} \hbar n \left(\omega_{p\mathbf{k}}, T \right) d\mathbf{k}^3, \tag{1}$$

which integrates the contributions to thermal transport from all phonons at all polarizations p and wave vectors $\mathbf{k}$ in the crystal's first Brillouin zone. Here, ω and $\mathbf{v}_{p,\mathbf{k}}$ are the phonon angular frequency and group velocity, respectively, which are obtained from the phonon dispersion relation.

The equation above gives a material's inherent capacity for transporting heat under the assumption that the perturbation in the phonon population that gives rise to a net heat flux is spatially homogeneous. However, in most practical applications materials contain defects and impurities in addition to micro and nano-structured morphology; these all present additional resistance to phonon transport. Predicting the macroscale thermal conductivity in these heterogeneous materials is more complicated, but is of profound technological importance as the hierarchy of defect structure and morphology can be central to the material's functionality. For example, in thermoelectric devices, dopants, impurities, inclusions, and nano-structuring are engineered into materials in order to optimize the electrical and thermal properties. In other applications where materials are under irradiation, it is essential to predict

the evolution of thermal conductivity during the accumulation of radiation-induced damage.

In materials where atomistic to micro-scale heterogeneity impacts thermal conductivity, the phonon population is also not spatially uniform, and so predicting the macroscopic thermal conductivity requires an understanding of the full phonon population distribution within some representative microstructure. This can be done by *simulating* the spectrally-dependent phonon distribution as governed by the Boltzmann transport equation (BTE) using phonon transport properties derived from DFT calculations of atomic interactions. The BTE describes the evolution of a distribution of particles as a function of their position, frequency and direction of travel, making the BTE a six-dimensional equation (or seven-dimensional, in the time-dependent case).

Advances have been made in the simulation of spectrally-dependent phonon transport, providing important insights into the spectral contribution to heat transport, but to date the computational burden associated with BTE solutions have limited the size, dimensionality, and/or physics of the systems considered. Allu *et al.* [57] investigated frequency dependence of the BTE in silicon slabs and reported spectral thermal conductivity based on Knudsen number (the mean free path divided by the domain length). However, the trade-off of this approach was their reported high computational expense, and the discrete phonon groups had no coupling. Mazumder and Majumdar [60] demonstrated polarization dependence of phonons in Monte Carlo transport simulations and showed the importance of the branch dependence; polarization transitions occur for background scattering as well as anharmonic interactions [21]. Hua derived the time and frequency dependent phonon transport equation using the method of degenerate kernels in

an attempt to increase computational efficiency compared to traditional integral discretization methods [58]. This was only done in 1-D, did not provide any spatial discretization, and was primarily analytical. As simulating frequency dependent phonon transport allows for the characterization of the frequency spectra, it allows for mode dependent contributions to the specific heat capacity and phonon velocity. Minnich *et al.* [54] demonstrated this mode dependence in their simulations of aluminum and silicon thin films, and calculated the spectral heat capacity from each frequency interval, explicitly illustrating the contribution of each mode to thermal conductivity. Rather than discriminating phonons by frequency and polarization, Romano has developed an approach that separates phonon modes into groups by discretizing the spectrum of phonon mean free path (MFP) [115, 116]. This provides considerable computational savings as the MFP is the only spectrally relevant phonon property that appears in the BTE. Most recently, Zhang *et al.* [61] developed a coupled approach using a reference temperature formulation which efficiently simulates temperature distribution and thermal conductivity over the nano- to micro-scale length range. However, they did not consider optical phonons with short mean free paths in their simulations. We discuss the results of Zhang *et al.* in greater detail below, but taken together, these prior works highlight that for simulating phonons it is imperative that the phonons are spectrally-resolved, and that however one defines the phonon spectrum, one cannot cavalierly disregard portions of it. This makes fully self-coupled calculations of large systems computationally challenging. In this manuscript we present an alternative approach for solving the spectrally-dependent phonon BTE that draws on numerical methods developed for neutron transport in the software package Rattlesnake [73]. The method solves the BTE in the self-adjoint angular flux (SAAF) formulation, which is computationally efficient, making it possible to simulate phonon transport in relatively large systems.

The numerical procedures for simulating the collective transport of phonons occupying a spectrum of vibrational modes is similar to the procedures used in nuclear engineering for simulating multi-group neutron or radiation transport [4,72]. With neutron or radiation transport, the energy spectrum is partitioned into discrete groups and the transport simulation accounts for within-group and group-to-group scattering of neutrons based on the interaction cross sections. Rattlesnake [73] employs a multi-group energy discretization scheme to solves the BTE for neutrons. It is developed in the Multi-physics Object Oriented Simulation Environment (MOOSE) framework [70] at Idaho National Laboratory (INL) and solves the SAAF-BTE using a finite element spatial discretization and a discrete ordinates angular discretization. Having previously adapted Rattlesnake to model one-group (grey) phonon transport [55,56,117] in both homogeneous and heterogeneous media, in the work presented here we have further developed Rattlesnake to simulate spectrally-dependent phonon transport.

The remainder of the manuscript is organized as follows: In the next section we develop the methods used to derive the SAAF-BTE for spectral transport, temperature coupling between discrete phonon groups, and the energy redistribution function used in closing the system of equations. Following this, we describe the methods used to compute a material's phonon properties and the methods we have developed to convolve these data into the collective properties of a set of discrete transport groups simulated in the SAAF-BTE. Finally, to demonstrate the computational efficiency of our multi-group, temperature coupled approach, simulations are presented of phonon transport in silicon of varying thickness. For these we report spectrally-resolved temperature, heat flux, and thermal conductivity. We discuss each of these quantities, how they are affected by spatial and angular

resolution, the effect of the new closure term, and how convergence is affected by the simulation of all phonon modes.

3.3   Methods

The generalized Boltzmann transport equation is used widely by the transport community to model the evolution of a distribution of particles or carriers. The modes of atomic vibration of crystal are traveling waves with well defined wave vectors. These waves extend across the entirety of the crystal; however, if uncertainty is applied to the wavevector the vibrations become propagating localized wavepackets. As the energy of vibrations comes in discrete quanta proportional to their vibrational frequency, individual wavepackets can be treated as quasiparticles – phonons – that collectively follow Bose-Einstein statistics. The total vibrational energy of the crystal can thus be modeled as a phonon quasiparticle gas and so can be described by the Boltzmann transport equation for uncharged particles:

$$\frac{df\left(\mathbf{r}, \mathbf{k}, p\right)}{dt} = -\mathbf{v}\left(\mathbf{k}, p\right) \cdot \nabla f\left(\mathbf{r}, \mathbf{k}, p\right) + \left[\frac{df}{dt}\right]_{\text{coll.}}. \tag{2}$$

Here $f\left(\mathbf{r}, \mathbf{k}, p\right)$ is the number of phonons at location $\mathbf{r}$ occupying the phonon mode with wavevector $\mathbf{k}$ and polarization p. The term $\mathbf{v}$ is the group velocity of a phonon wavepacket and is given by $\mathbf{v} = \mathbf{v}\left(\mathbf{k}, p\right) = \nabla_{\mathbf{k}}\omega\left(\mathbf{k}\right)$, the derivative of the vibration's angular frequency, ω, with respect to $\mathbf{k}$. The group velocity is a vector normal to the isofrequency surface for the dispersion relation which is not necessarily parallel to $\mathbf{k}$. While the natural parameter for enumerating the phonon modes of a crystal is the wavevector and polarization (4 quantum numbers are required), for transport simulations it is more natural to parameterize the particle/carrier population by the particles' direction of travel, and then by their speed, and to treat these two parameters separately. This is particularly true for neutron transport as their

dispersion relation is isotropic. To put the phonon transport problem in to a form where it can leverage the numerical power of existing transport solvers such as Rattlesnake, and restricting our interest to the time independent case, in what follows we write the Boltzmann transport

$$\left| \mathbf{v} \left(\hat{\mathbf{\Omega}}, \eta, p \right) \right| \hat{\mathbf{\Omega}} \cdot \nabla f \left(r, \hat{\mathbf{\Omega}}, \eta, p \right) = \left[\frac{df \left(r, \hat{\mathbf{\Omega}}, \eta, p \right)}{dt} \right]_{\text{coll.}}, \tag{3}$$

where $f = f(\mathbf{r}, \hat{\mathbf{\Omega}}, \eta, p)$ has been parameterized by the phonons' direction of propagation, $\hat{\mathbf{\Omega}}$, and spectral variable η. The spectral metric η could be energy, frequency, wave number, mean free path, or any other descriptor or quantum number for enumerating the phonon modes.

The term on the right hand side (RHS) of Eq. (3) is the rate of change of the population of due to the creation/annihilation of phonons and events that change a phonon's direction of travel. We model this using the single mode relaxation time (SMRT) approximation [11] which assumes that the net rate of loss/gain of phonons in a single mode is described by a single relaxation time, $\tau = \tau(\hat{\mathbf{\Omega}}, \eta, p)$, and is proportional to the deviation of the population from thermodynamic equilibrium. Defining the mean free path (MFP) of phonons $\Lambda(\hat{\mathbf{\Omega}}, \eta, p) = |\mathbf{v}| \tau$, the simplified BTE is written as

$$\hat{\mathbf{\Omega}} \cdot \nabla f = \frac{f^0 \left(T\left(\mathbf{r} \right), \hat{\mathbf{\Omega}}, \eta, p \right) - f}{\Lambda}, \tag{4}$$

where the equilibrium phonon distribution f^0 is described by Bose-Einstein statistics

$$f^0 = f^0 \left(T\left(\mathbf{r} \right), \hat{\mathbf{\Omega}}, \eta, p \right) = \langle n_{\text{BE}} \rangle = \frac{1}{\exp \left[\frac{\hbar \omega \left(\hat{\mathbf{\Omega}}, \eta, p \right)}{k_{\text{B}} T(\mathbf{r})} \right] - 1}.$$

Here $T\left(\mathbf{r} \right)$ is the local temperature, $\hbar$ is the reduced Planck constant and k_B is Boltzmann's constant.

The population f gives the *number* of phonons in the mode characterized by $\hat{\boldsymbol{\Omega}}$, η, and p and is thus dimensionless. As we are interested transport of heat rather than phonon number is more useful to weight the population by the modes' contribution to energy flux, and solve for the *angular flux intensity*, ψ, which has dimensions of power per area per steradian, and is defined as

$$\psi\left(\mathbf{r}, \hat{\boldsymbol{\Omega}}, \eta, p\right) = \hbar\omega\mathbf{v}f\mathbb{D}d\eta. \tag{5}$$

Here the term, $\mathbb{D} = \mathbb{D}(\hat{\boldsymbol{\Omega}}, \eta, p)$ is the phonon density of states (DOS) per increment of solid angle $\hat{\boldsymbol{\Omega}}$ and spectral descriptor. It has dimensions of number per unit volume per steradian per η, and it satisfies the relationship

$$3N_v = \sum_p \int d\eta \int_{4\pi} \mathbb{D}\left(\hat{\boldsymbol{\Omega}}, \eta, p\right) d\Omega, \tag{6}$$

where N_v is the number of atoms per unit volume. The BTE in terms of angular radiance is

$$\hat{\boldsymbol{\Omega}} \cdot \nabla\psi = \frac{\phi^0 - \psi}{\Lambda}, \tag{7}$$

where ϕ^0 is the *radiance* of the mode at equilibrium given by

$$\phi^0 = \phi^0\left(T\left(\mathbf{r}\right), \hat{\boldsymbol{\Omega}}, \eta, p\right) = \frac{\hbar\omega\,\mathbf{v}\,\mathbb{D}d\eta}{\exp\left[\frac{\hbar\omega}{k_B T(\mathbf{r})}\right] - 1}, \tag{8}$$

and is discretized into partitions with dependency on $\hat{\boldsymbol{\Omega}}$ within the Brillouin zone; this method is discussed in a proceeding section. The local temperature is defined as the temperature that a system at equilibrium would have in order to have the same thermal energy, U_T, as the phonon bath

$$U_T\left(\mathbf{r}\right) = \sum_p \int d\eta \int_{4\pi} d\hat{\boldsymbol{\Omega}}\frac{\hbar\omega\,f\,\mathbb{D}}{\exp\left[\frac{\hbar\omega}{k_B T(\mathbf{r})}\right] - 1}$$

$$= \sum_p \int d\eta \int_{4\pi} d\hat{\boldsymbol{\Omega}}\frac{\phi^0}{|\mathbf{v}|}. \tag{9}$$

The numerical approach to extract $T(\mathbf{r})$ from this relationship is described in detail later in the manuscript, but we first address the issue of energy conservation.

The SMRT approximation for the collision term that appears in the BTE in Eqs. (4) and (7) assumes that modes which are out of equilibrium exchange energy with an implied phonon reservoir at the local temperature to relax them back into equilibrium. However, as the rate of this energy exchange is different for all modes for any arbitrary phonon population, it is likely that there will be a net flow of energy to or from the phonon bath, resulting in a lack of local energy conservation. The problem is that the flow of energy into the implied phonon bath in the SMRT is not reflected in the explicit phonon bath used to compute temperature in Eq. (9), and so we must include an additional source term to correct this.

The net energy flow per unit volume, $\dot{U}_I$, to the implied phonon bath is

$$\dot{U}_I\left(\mathbf{r}\right) = \sum_p \int d\eta \int_{4\pi} d\Omega \, \frac{\phi^0 - \psi}{\Lambda}. \tag{10}$$

To conserve energy, we must return this energy to the explicit phonon bath, and to do that we must first decide how to distribute the energy over the phonon modes. The most obvious choice for this is to add the energy back proportional to the equilibrium distribution of energy across the modes. Applying this correction to the BTE to close the coupling of SMRT with the phonon bath gives:

$$\hat{\mathbf{\Omega}} \cdot \nabla \psi = \frac{\phi^0 - \psi}{\Lambda} - \beta \frac{\phi^0}{|\mathbf{v}|},$$

where β is a rate and is given by

$$\beta = \beta\left(\mathbf{r}\right) = \frac{\dot{U}_I}{U_T}.$$

This residual energy projection is a measure of the balance of the equilibrium phonon population to the transport system population; β is tightly coupled to

temperature, the transport and equilibrium systems, and is the closure required to ensure energy conservation. In our framework, both the temperature and β are functionals of the entire phonon population. The energy flow $\dot{U}_I$ can be either positive or negative depending on the phonon population. The most ballistic groups tend to have the strongest non-equilibrium condition occurring near isothermal boundaries and these are the regions in which we find β to be the largest.

3.3.1 SAAF-BTE for Phonons

In our previous work [55, 56, 117], we modified the SAAF-BTE for transport of grey neutrons to make it treat grey phonon transport, and then solved it to model heat conduction in UO_2 containing Xe bubbles. In grey transport the particles of interest are resolved in direction but the spectral properties are averaged over the entire distribution making a "grey" spectrum. In spectrally-resolved transport the grey approximation is equivalent to coupling the particle distribution evolution over angle, but having no coupling between the different portions of the property spectrum as in the first and second order equations

$$\hat{\mathbf{\Omega}} \cdot \nabla \psi \left(\mathbf{r}, \hat{\mathbf{\Omega}} \right) + \frac{1}{\Lambda} \psi \left(\mathbf{r}, \hat{\mathbf{\Omega}} \right) = \frac{1}{4\pi\Lambda} \phi^{\mathrm{T}} \left(\mathbf{r} \right), \tag{11}$$

$$-\hat{\mathbf{\Omega}} \cdot \nabla \left[\Lambda \hat{\mathbf{\Omega}} \cdot \nabla \psi \left(\mathbf{r}, \hat{\mathbf{\Omega}} \right) \right] + \frac{1}{\Lambda} \psi \left(\mathbf{r}, \hat{\mathbf{\Omega}} \right) = \frac{1}{4\pi} \left[\frac{1}{\Lambda} \phi^{\mathrm{T}} \left(\mathbf{r} \right) - \hat{\mathbf{\Omega}} \cdot \nabla \phi^{\mathrm{T}} \left(\mathbf{r} \right) \right]. \tag{12}$$

Here the coupling term, ϕ^{T}, is the zeroth angular moment

$$\phi^{\mathrm{T}} = \phi^{\mathrm{T}} \left(\mathbf{r} \right) = \int_{4\pi} \psi \left(\mathbf{r}, \hat{\mathbf{\Omega}} \right) d\Omega, \tag{13}$$

which we refer to as the *transport scalar flux*. The total scalar flux is defined as the integral of the zeroth angular moment over all spectral groups and polarizations

$$\Phi^{\mathrm{T}} = \Phi^{\mathrm{T}} \left(\mathbf{r} \right) = \sum_{p} \int_{\eta} \int_{4\pi} \psi \left(\mathbf{r}, \hat{\mathbf{\Omega}} \right) d\Omega d\eta,$$

and ϕ^{T} and Φ^{T} both have units of $\mathrm{W} \cdot \mathrm{rad}^{-1} \cdot \mathrm{m}^{-2}$. In the BTE, the phonon angular intensity is defined along a direction of travel $\hat{\mathbf{\Omega}}$, a function of polar and azimuthal angles θ and ϕ; $\hat{\mathbf{\Omega}}$ is an independent variable of ψ, which itself is the dependent variable, $\psi(\mathbf{r}, \hat{\mathbf{\Omega}})$.

The weak form of Eq. (12) was then solved with Rattlesnake. In this current work, we introduce a new form of the SAAF-BTE specifically for phonons, which relies on implicit temperature coupling to better represent the subtle physics of phonon transport. We return to Eq. (4), with phonon state variables multiplied through and the addition of the non-equilibrium bath source correction to the right hand side

$$|\mathbf{v}| \, \hat{\mathbf{\Omega}} \cdot \nabla \psi \left(\mathbf{r}, \hat{\mathbf{\Omega}} \right) = \frac{\frac{1}{4\pi} \phi^0 \left(T \left(\mathbf{r} \right) \right) - \psi \left(\mathbf{r}, \hat{\mathbf{\Omega}} \right)}{\tau} - \frac{\beta \left(T \left(\mathbf{r} \right) \right) \phi^0 \left(T \left(\mathbf{r} \right) \right)}{4\pi},$$

and rearrange

$$\hat{\mathbf{\Omega}} \cdot \nabla \psi \left(\mathbf{r}, \hat{\mathbf{\Omega}} \right) + \frac{1}{\Lambda} \psi \left(\mathbf{r}, \hat{\mathbf{\Omega}} \right) = \frac{1}{4\pi\Lambda} \phi^0 \left(T \left(\mathbf{r} \right) \right) - \frac{\beta \left(T \left(\mathbf{r} \right) \right)}{4\pi \, |\mathbf{v}|} \phi^0 \left(T \left(\mathbf{r} \right) \right), \qquad (14)$$

where the terms on the left are the streaming and collision operators, respectively, with source terms on the right hand side. We have included temperature dependent notation $(T \left(\mathbf{r} \right))$ in Eq. (14) as a reference point to show the terms where temperature is coupled in our approach. For much of the remainder of this section, we drop the independent variables $(\mathbf{r}, \hat{\mathbf{\Omega}})$.

The vacuum and reflecting boundary conditions for this transport equation are defined as:

$$\psi \left(\mathbf{r}_b \right) = \begin{cases} \psi^{\mathrm{vac}} \left(\mathbf{r}_b, \hat{\mathbf{\Omega}} \right), \hat{\mathbf{\Omega}} \cdot \bar{\mathbf{n}}_b < 0 \\ \psi^{\mathrm{ref}} \left(\mathbf{r}_b, \hat{\mathbf{\Omega}}_r \right), \hat{\mathbf{\Omega}} \cdot \bar{\mathbf{n}}_b < 0 \end{cases},$$

here, $\bar{\mathbf{n}}_b$ is the outward unit normal at a point $\mathbf{r}_b$ on the boundary. In neutron transport space, ψ^{vac} implies a vacuum boundary $(\psi(\mathbf{r}_b, \hat{\mathbf{\Omega}}) = 0)$. However, in this

implementation, we leverage the vacuum boundary as an adiabatic boundary to specify an incident source of phonons, e.g., $\psi(\mathbf{r}_b, \hat{\boldsymbol{\Omega}}) = \phi^0(\mathbf{r}_b)$. The reflective angle $\hat{\boldsymbol{\Omega}}_r$ in ψ^{ref} is

$$\hat{\boldsymbol{\Omega}}_r = \hat{\boldsymbol{\Omega}} - 2\left(\hat{\boldsymbol{\Omega}} \cdot \bar{\mathbf{n}}_b\right)\bar{\mathbf{n}}_b.$$

The derivation of the SAAF form of the phonon BTE is based on a straightforward algebraic technique. From a computational perspective the SAAF formulation is advantageous as the full angular flux intensity is the unknown. Upwinding is a common numerical discretization of advection operators in partial differential equations, and is frequently used with the traditional first-order form of the Boltzmann transport equation, particularly in one and two spatial dimensions. The (primarily) lower triangular linear algebra problem in each quadrature direction is solved via a "transport sweep" - forward propagation of information through spatial cells in the direction of particle travel. The SAAF equations have an elliptic streaming term, and the resulting linear algebraic equations for the intensity in each angular ordinate are then solved via preconditioned GMRES methods on unstructured spatial grids – this is the primary numerical advantage to using the SAAF equations; `boomerAMG`-preconditioned GMRES is massively parallelizable. In contrast, sweeping algorithms (especially on unstructured grids in 3D) are challenging to implement in parallel; the development of an efficient parallel sweep algorithm is an active area of interest in the neutron transport community [118]. The use of reflecting boundary conditions is easier with the availability of the full angular flux, as the incoming and outgoing directions are coupled in the same manner as the first order form of the transport equation [69]. Through the application of a continuous finite element (CFEM) spatial discretization, the matrices are symmetric positive definite (SPD), which allows for the use of solution techniques such as the

preconditioned Krylov family of solvers. To obtain the SAAF form of the BTE, a simple algebraic approach is followed, solving Eq. (14) for the angular intensity:

$$\psi = \frac{\phi^0}{4\pi} - \frac{\Lambda\beta\phi^0}{4\pi\,|\mathbf{v}|} - \Lambda\hat{\mathbf{\Omega}}\cdot\nabla\psi,$$

and substitute this expression back into the streaming term in Eq. (14)

$$\hat{\mathbf{\Omega}}\cdot\nabla\left(\frac{\phi^0}{4\pi} - \frac{\Lambda\beta\phi^0}{4\pi\,|\mathbf{v}|} - \Lambda\hat{\mathbf{\Omega}}\cdot\nabla\psi\right) + \frac{1}{\Lambda}\psi = \frac{\phi^0}{4\pi\Lambda} - \frac{\beta\phi^0}{4\pi\,|\mathbf{v}|}, \tag{15}$$

rearranging yields the SAAF form of the phonon BTE

$$-\hat{\mathbf{\Omega}}\cdot\nabla\left[\Lambda\hat{\mathbf{\Omega}}\cdot\nabla\psi\right] + \frac{1}{\Lambda}\psi = \frac{1}{4\pi}\left[\frac{\phi^0}{\Lambda} - \hat{\mathbf{\Omega}}\cdot\nabla\phi^0 - \frac{\beta\phi^0}{|\mathbf{v}|} + \hat{\mathbf{\Omega}}\cdot\nabla\frac{\Lambda\beta\phi^0}{|\mathbf{v}|}\right]. \tag{16}$$

We use the discrete ordinates method [74] to discretize the angular variable. In the discrete ordinates approach, we represent the independent variable $\hat{\mathbf{\Omega}}$ by a discrete set of directions, $\{\hat{\mathbf{\Omega}}_m, m = 1, \ldots, M\}$. The functions of $\hat{\mathbf{\Omega}}$ are represented only by their values at each of their directions on the spatial mesh, e.g.,

$$f\left(\mathbf{r}, \hat{\mathbf{\Omega}}\right) \to f\left(\mathbf{r}, \hat{\mathbf{\Omega}}_m\right) \equiv f_m\left(\mathbf{r}\right), \qquad m = 1, \ldots, M. \tag{17}$$

Consider the angular flux intensity as a function of the direction variable $\hat{\mathbf{\Omega}}$. There exists a set of complete orthogonal functions in $\hat{\mathbf{\Omega}}$, much like Legendre polynomials; these are the spherical harmonics functions. To compute the total scalar flux in a group at the end of an iteration, the angular flux intensity is integrated over direction using Eq. (13). However, we make the approximation that the angular flux intensity $\psi(\mathbf{r}, \hat{\mathbf{\Omega}})$ can be represented by these spherical harmonics functions (termed Y) and we expand the angular flux in terms of these functions

$$\psi\left(\mathbf{r}, \hat{\mathbf{\Omega}}\right) \approx \frac{1}{4\pi}\sum_{k=0}^{\infty}\sum_{n=-k}^{n=k}\psi_{k,n}\left(\mathbf{r}\right)Y_{k,n}\left(\hat{\mathbf{\Omega}}\right), \tag{18}$$

where

$$\psi_{k,n}\left(\mathbf{r}\right) = \int_{4\pi}Y_{k,n}^*\left(\hat{\mathbf{\Omega}}\right)\psi\left(\mathbf{r}, \hat{\mathbf{\Omega}}\right)d\Omega. \tag{19}$$

This approach involves expanding the angular dependence of the flux intensity in a finite series of spherical harmonics $Y_{l,m}(\hat{\mathbf{\Omega}}) = Y_{l,m}(\theta, \varphi)$, a familiar sight in quantum mechanics. Coupling for the angular flux intensity and the transport flux exists in the angular moments alone

$$\phi_{l,n}(\mathbf{r}) = \frac{1}{4\pi} \sum_{l=0}^{L} \sum_{n=-l}^{l} \sum_{m=1}^{M} w_m \psi_m(\mathbf{r}) Y_{l,n}^*\left(\hat{\mathbf{\Omega}}_m\right) Y_{l,n}\left(\hat{\mathbf{\Omega}}_m\right),$$

here, L is the truncated spherical harmonics, l is the degree of spherical harmonics and n is the order, and weights sum to 2π in 2D

$$\sum_{m=1}^{M} w_m = 2\pi.$$

The total heat flux $\mathbf{q}(\mathbf{r})$ is the sum of the first angular moments ($\phi_{1,0}$ and $\phi_{1,1}$ for two spatial dimensions) over all spectral groups and polarizations

$$\mathbf{q}(\mathbf{r}) = \sum_{p} \int_{\eta} \int_{4\pi} \psi\left(\mathbf{r}, \hat{\mathbf{\Omega}}\right) \hat{\mathbf{\Omega}} d\Omega d\eta,$$

and has units of $\mathrm{W} \cdot \mathrm{m}^{-2}$. In this way we solve the transport equation for each angular direction $\hat{\mathbf{\Omega}}_m$. At the end of each iteration, the numerical integration is performed to represent the scalar flux with these angular moments. Then, ϕ^{T} is used to determine the local temperatures in the transport system, and are then passed into the equilibrium radiance relations. Now that we have represented the angular flux intensity by this quadrature, the discrete form of Eq. (16) for any direction $\hat{\mathbf{\Omega}}_m$ with an associated weight w_m in the angular quadrature set is:

$$- \hat{\mathbf{\Omega}}_m \cdot \nabla \left[\Lambda \hat{\mathbf{\Omega}}_m \cdot \nabla \psi_m^{(\ell+1)}\right] + \frac{1}{\Lambda} \psi_m^{(\ell+1)} =$$

$$\frac{1}{4\pi} \left[\frac{\phi^{0,(\ell)}}{\Lambda} - \hat{\mathbf{\Omega}}_m \cdot \nabla \phi^{0,(\ell)} - \frac{\beta^{(\ell)} \phi^{0,(\ell)}}{|\mathbf{v}|} + \hat{\mathbf{\Omega}}_m \cdot \nabla \frac{\Lambda \beta^{(\ell)} \phi^{0,(\ell)}}{|\mathbf{v}|}\right], \quad (20)$$

where we have assigned iteration indices to Eq. (20); we solve for the value of angular flux intensity, $\psi^{(\ell+1)}$ using sources from the previous iteration (ℓ). This resembles source iteration, a well known solution technique in neutron transport [74, 119, 120]. This procedure is outlined in Algorithm 1.

The transport calculation assumes that all of the spectral groups are decoupled; each system of equations is solved separately and no information is passed between them. We have demonstrated this capability previously with Rattlesnake [56, 117]. It is possible to solve each system of equations separately and then compute an average material temperature for the domain. However, this only considers isolated group contributions to temperature and heat flux. Explicit simulation of group-to-group phonon scattering foregoes the SMRT approximation, is computationally demanding, and is an active research area [13, 54]; this work does not consider explicit scattering processes.

The physics dictate that phonon modes are coupled as they become excited through phonon collisions and temperature changes. The amount of heat flowing through each phonon mode in the system must 'see' the others – even forsaking an explicit collision model, individual modes must feel the effects of the material temperature; Bose-Einstein statistics assert this, and the phonon groups must be globally coupled in some manner. A material temperature is determined by prescribing a temperature gradient between spatial boundaries, giving rise to blackbody phonon emission into the material. Phonon scattering in each of the groups are driven by this temperature gradient, but again no coupling exists. This decoupled approach fails to consider the temperature in the Bose-Einstein statistics which must be extended to all phonon modes – the true equilibrium distribution is an integration coupling all spectral zones. Temperature is defined by the phonon

phase space distributions, spanning all modes and polarizations. Phonons are coupled via the internal energy of the crystal system, and we can leverage this detail to derive a set of self-consistent equations where an average material temperature is shared between each of the discrete phonon groups.

The total phonon radiance of the system is defined as

$$\Phi^{00} = \Phi^{00}\left(T\left(\mathbf{r}\right)\right) = \sum_{p} \int_{\eta} \frac{\hbar\omega \left|\mathbf{v}\right| \mathbb{D}}{\exp\left[\frac{\hbar\omega}{k_{\mathrm{B}}T(\mathbf{r})}\right] - 1} d\eta, \tag{21}$$

which is just the contribution of ϕ^0 over all modes. We make the assumption that the total equilibrium radiance Φ^{00} can be related to the total transport scalar flux in the domain, such that the two must be in radiative equilibrium. This treatment uses the Bose-Einstein distribution as the phonon source for each of the spectral groups as opposed to the transport scalar flux; we still perform an integration of the angular intensity at the end of each linear iteration to obtain transport scalar flux. Equating Φ^{00} to the sum of the transport flux, we have

$$\Phi^{00}\left(\mathbf{r}\right) = \sum_{p,\eta} \phi^{\mathrm{T}} = \sum_{p,\eta} \frac{\hbar\omega_{p,\eta} \left|\mathbf{v}_{p,\eta}\right| \mathbb{D}_{p,\eta}}{\exp\left[\frac{\hbar\omega_{p,\eta}}{k_{\mathrm{B}}T(\mathbf{r})}\right] - 1}, \tag{22}$$

where the (p, η) index denotes a double summation over the polarizations and spectral property indices. Now we may carry out the solution for $T\left(\mathbf{r}\right)$, which involves summations over the angularly dependent material properties (index m) and group index g, both described in proceeding Sec. 3.3.2.

$$T\left(\mathbf{r}\right) = \sum_{g,m} \frac{\hbar\overline{\omega}_{g,m}}{k_{\mathrm{B}} \ln\left[\frac{\hbar\omega_{g,m}v_{g,m}\mathbb{D}_{g,m}}{\phi_g^{\mathrm{T}}(\mathbf{r})} + 1\right]}. \tag{23}$$

Equation (23) is used to compute an average temperature for the entire spatial domain. $T\left(\mathbf{r}\right)$ is what couples the phonon groups together – they now depend on a global average temperature. The resulting value of $T\left(\mathbf{r}\right)$ is used to compute a new value of ϕ^0 using Eq. (8).

Equation (20) in the discrete ordinate method generates a linear system of equations arising from the spatial discretization of an elliptic operator, and is solved for angular intensity $\psi_{p,\eta,m}$ in each quadrature direction. This means that software for solving the diffusion approximation to transport can be exploited to implement acceleration techniques, which will be part of a future study. The Galerkin weak form of Eq. (20) using weighted residual formulation with CFEM is then solved with Rattlesnake. The derivation of the weak form of the SAAF-BTE for phonons is similar to that of the weak form of the SAAF-BTE for neutrons and can be followed in the Rattlesnake theory [73]. Algorithm 1 is outlines the technique used to solve the system of equations.

Algorithm 1: Temperature coupled iteration

---

1 initialize $\phi^0\left(\mathbf{r}_b\right), \psi_m^{(\ell)}\left(\mathbf{r}\right), \phi^{\mathrm{T},(\ell)}\left(\mathbf{r}\right), \phi^{0,(\ell)}\left(\mathbf{r}\right), \Phi^{00,(\ell)}\left(\mathbf{r}\right),\, \Phi^{\mathrm{T},(\ell)}\, T^{(\ell)}\left(\mathbf{r}\right)$
2 set convergence tolerance ε
3 **for** $g = 1$ *to* G **do**
4 $\quad$ **for** $m = 1$ *to* M **do**
5 $\quad\quad$ solve SAAF-BTE (Eq. 20) for $\psi_m^{(\ell+1)}$
6 $\quad$ **end**
7 $\quad$ compute $\phi^{\mathrm{T},(\ell+1)}\left(\mathbf{r}\right)$ and solve for $T^{(\ell+1)}\left(\mathbf{r}\right)$
8 $\quad$ compute $\phi^0\left(T^{(\ell+1)}\right)$
9 **end**
10 compute $\Phi^{00,(\ell+1)}$, $\Phi^{\mathrm{T},(\ell+1)}$, $\beta^{(\ell+1)}$
11 **if** $\left|\frac{\phi^{T,(\ell+1)}(\mathbf{r})-\phi^{T,(\ell)}(\mathbf{r})}{\phi^{T,(\ell+1)}(\mathbf{r})}\right| < \varepsilon$ **then**
12 $\quad$ break
13 **else**
14 $\quad$ go to 3

3.3.2 Phonon Transport Properties of Silicon

For the purposes of demonstrating and testing the use of Rattlesnake to simulate spectrally-resolved phonon transport we use silicon as a model material system. The thermal conductivity of Si is isotropic and well characterized, and there are

a wealth of experimental and computational data against which to compare our model. Silicon has cubic crystal symmetry; to simplify our model and to enable us to use a standard set of transport ordinates akin to neutron transport (which does not have cubic symmetry), we simplify the transport spectrum to make it spherically symmetric. The discussion that follows describes first the process we used to compute *ab initio* the phonon properties of Si, and the metric we have developed for grouping the phonon modes of Si into a discrete set of transport groups with aggregated transport properties.

3.3.2.1   Calculation of Phonon Properties

The frequency and group velocity of phonons with a given wave vector and polarization are computed from the dispersion relation obtained from the dynamical matrix of second order force constants. The probability of three phonon scattering processes, the dominant intrinsic scattering process at high temperature, are computed from the matrix of third order stiffness interactions. The 2nd and 3rd order force constants for Si at 0 K were obtained from the *AlmaBTE* database [113]. In this data set the 2nd order force constants were computed via the frozen phonon method as implemented using *phonopy* [39] using a large $5 \times 5 \times 5$ supercell in order to accurately capture the contributions from long ranged interatomic interactions. The 3rd order force constants were calculated using a $5 \times 5 \times 5$ supercell using the package *thirdorder.py* [114] and considered all three-atom interactions of atoms less than five neighbours removed from one another. The complexity of the unit cell does not directly affect computational cost, but it can have indirect influence on the computational cost. The main source of computational expense comes from how finely one resolves the phonon spectrum, which depends on the span of frequencies and mean free paths. However, the CPU time is impacted by the acoustic thickness

of a particular angle-group; if the unit cell has many optical modes with low velocity and short lifetime, these diffusive modes will take longer to converge. We discuss this further in a proceeding section. The full details of the DFT calculations are given in reference [114].

Starting with these stiffness matrices we used *AlmaBTE* to compute the full phonon dispersion and group velocities on a $24 \times 24 \times 24$ Brillouin zone mesh. The 0 K velocities and frequencies were assumed to be unchanged at higher temperatures. The phonon-phonon scattering times were computed on the same mesh at a temperature of 300 K. All of the phonon modes in the Brillouin zone are represented in the transport groups, albeit in an approximate way. In this work, this was done to make the transport spectrum spherically symmetric; however it is no extra work to include all the modes in the Brillouin zone in a non-approximate way, and to model anisotropic materials. For this, one would need to use a set of ordinates which match the crystal symmetry, and we would not be able to decouple the transport group's properties and directions.

3.3.3 Decomposition of Phonon Spectrum into Transport Groups

Discretization of the BTE in Eq. (20) means solving for the heat flux in a set of transport groups where each group represents the combined contribution to transport from a collection of phonon modes with similar direction of propagation and spectral character. The task is to determine the effective transport properties of each group such that all phonon modes are accounted for, and that the temperature in Eq. (23) may be inverted.

In discretized form, the angular and spectral distribution of a quantity $A(\hat{\mathbf{\Omega}}, \eta, p)$

of the population is approximated as a sum of piece-wise basis functions:

$$A\left(\hat{\mathbf{\Omega}}, \eta, p\right) \approx \sum_{m=1}^{N_\Omega} \sum_{g=1}^{N_\eta} A_{m,g,p} \chi_m\left(\hat{\mathbf{\Omega}}\right) \chi_g\left(\eta\right).$$

Here m is the index over discrete ordinates in $\hat{\mathbf{\Omega}}$, and g is the index over control points (*groups*) in p and η. The functions $\chi_m(\hat{\mathbf{\Omega}})$ and $\chi_g\left(\eta\right)$ are element shape functions — non overlapping boxcar functions that satisfy the relationships

$$\int_\eta d\eta \int_{4\pi} d\Omega \, \chi_m\left(\hat{\mathbf{\Omega}}\right) \chi_g\left(\eta\right) = w_m \Delta\eta_g,$$

where $\Delta\eta_g$ is the width of the g-th spectral group, and

$$\int_\eta d\eta \int_{4\pi} d\Omega \, \chi_m\left(\hat{\mathbf{\Omega}}\right) \chi_g\left(\eta\right) \chi_{m'}\left(\hat{\mathbf{\Omega}}\right) \chi_{g'}\left(\eta\right) = \begin{cases} w_m^2 \Delta\eta_g^2, & \text{if } m = m' \text{ and } g = g' \\ 0, & \text{otherwise} \end{cases}.$$

The transport group quantities $A_{m,g}$ represent the combined contribution to transport from all of the phonon modes that fall into the m, g-th group. To perform this calculation we define the group integration operator

$$G_{m,g}\left\{A\left(\hat{\mathbf{\Omega}}, \eta, p\right)\right\} = \sum_d \int_\eta d\eta \int_{4\pi} d\Omega \, A\left(\hat{\mathbf{\Omega}}, \eta, p\right) \chi_m\left(\hat{\mathbf{\Omega}}\right) \chi_g\left(\eta\right).$$

Using this operator we define the groups' mean free path as the average of the mean free paths of the phonon modes in the group weighted by their contribution to the phonon flux

$$\Lambda_{m,g} = \frac{G_{m,g}\left\{\Lambda\phi^0\left(\overline{T}\right)\right\}}{G_{m,g}\left\{\phi^0\left(\overline{T}\right)\right\}}.$$

Where $\overline{T}$ is the expected average temperature of the system to be simulated.

Similarly, for computing radiance from temperature we define:

$$\phi_{m,g}^0\left(\overline{T}\right) = \frac{1}{w_m}G_{m,g}\left\{\phi^0\left(\overline{T}\right)\right\} = \frac{1}{w_m}G_{m,g}\left\{\frac{\hbar\omega\,|\mathbf{v}|\,\mathbb{D}}{\exp\left(\frac{\hbar\omega}{k_BT}\right)-1}\right\},$$

$$\phi_{m,g}^{0,\prime}\left(\overline{T}\right) = \frac{1}{w_m}G_{m,g}\left\{\frac{d\phi^0\left(\overline{T}\right)}{dT}\right\},$$

$$\phi_{m,g}^{0,\prime\prime}\left(\overline{T}\right) = \frac{1}{w_m}G_{m,g}\left\{\frac{d^2\phi^0\left(\overline{T}\right)}{dT^2}\right\}.$$

The only material properties in the discretized BTE (Eq. (20)) are the groups' effective mean free path and radiance, however the transport simulation needs to be able to compute the local temperature and so it also requires the weighting terms to obtain this from the sum over fluxes. To compute the energy in a group from the angular flux, we define the group velocity as the averaged velocity weight by mode energy

$$\overline{v}_{m,g} = \frac{G_{m,g}\left\{\phi^0\left(\overline{T}\right)\right\}}{G_{m,g}\left\{\frac{\phi^0\left(\overline{T}\right)}{|\mathbf{v}|}\right\}}.$$

For the local temperature calculation we need to know the total of the product of frequency, density of states and velocity

$$\overline{\omega v\mathbb{D}}_{m,g} = G_{m,g}\left\{\omega\,|\mathbf{v}|\,\mathbb{D}\right\},$$

and the average frequency

$$\overline{\omega}_{m,g} = \frac{G_{m,g}\left\{\omega\mathbb{D}\right\}}{G_{m,g}\left\{\mathbb{D}\right\}}.$$

The approach developed up to this point is quite general; we have not yet specified a choice of spectral parameterization, and the method can be applied to anisotropic materials if one uses a set of transport ordinates with the appropriate symmetry. In the remainder of the manuscript we limit ourselves to one choice for

parameterization of the dispersion in Si, in which we approximate the dispersion relation to be spherically symmetric enabling us to use a standard set of non-symmetric transport ordinates. In this approach we used just the dispersion for Si along the (100) crystal direction, and we collapsed the three optical branches and the two transverse acoustic branches into a single branch with averaged frequency as shown in Fig. 2.4. The dispersion was parameterized in wave *number*, k, and this condensed (100) dispersion was used as the dispersion along all directions. The density of states was defined as

$$\mathbb{D}\left(\hat{\mathbf{\Omega}}, k, p\right)_{m,g} = \frac{3d_p k^2}{\pi k_{\max}^3 a_{\text{Si}}^3},$$

where d_p is the degeneracy that accounts for the merged branches and a_{Si} is the lattice parameter of the Si unit cell. The integral of this accounts for all the phonon modes of Si

$$\sum_{p=1}^{3} \int_{4\pi} d\Omega \int_0^{k_{\max}} dk \frac{3d_p k^2}{\pi k_{\max}^3 a_{\text{Si}}^3} = \frac{3 \times 8}{a_{\text{Si}}^3} = 3N_v,$$

The approximated dispersion was split into between three and 20 groups in k of equal size; we used a discretization of 9 groups in our simulation, split up amongst the polarizations (see Table 3.1).

Using these data, we can compute radiant emission sources on the boundaries, driven by a prescribed temperature boundary condition,

$$\phi_{p,\eta}^0 \left(T\left(\mathbf{r}_b\right)\right) = \frac{\hbar \omega_{p,\eta} \left|\mathbf{v}_{p,\eta}\right| \mathbb{D}_{p,\eta}}{\exp\left[\frac{\hbar \omega_{p,\eta}}{k_b T(\mathbf{r}_b)}\right] - 1}. \tag{24}$$

Equation (24) is used by the vacuum condition at a boundary $\mathbf{r}_b$ to supply an incident source of phonons for a given group and polarization. We compute an effective thermal conductivity along a direction by taking the ratio of the total heat flux to the end-to-end temperature gradient (which includes boundary effects) in
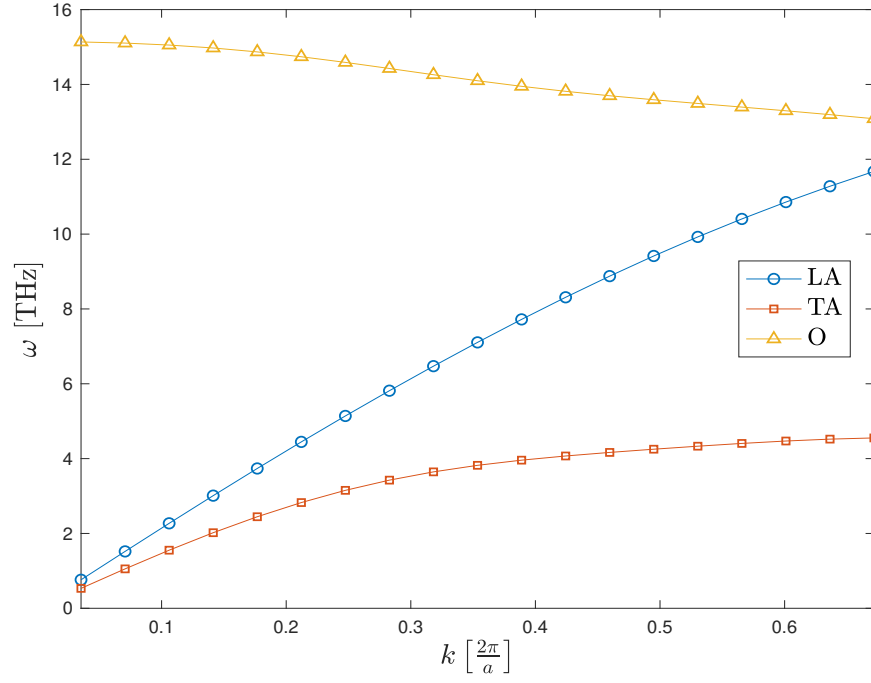
Figure 3.1: Dispersion relation in silicon.
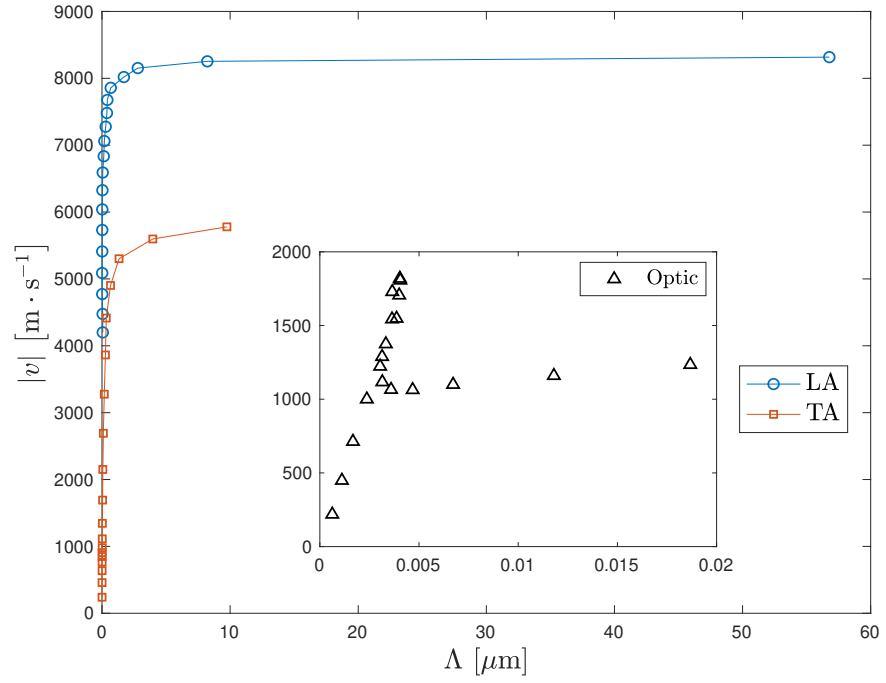
Figure 3.2: Mean free paths for dispersion branches vs. group velocity. Units are consistent for inset figure.

Table 3.1: Silicon material properties.

G	Λ [nm]	$\overline{\omega} \cdot 10^{13}$ [s^{-1}]	$\overline{v}$ [m·s^{-1}]	$\overline{\mathbb{D}} \cdot 10^{27}$ [m^{-3}]	$\overline{\tau}$ [ps]	$\overline{\omega v \mathbb{D}}$ [m^{-2}·s^{-2}]
1 (LA)	3120	1.49	8079	0.0736	386	$12.9 \cdot 10^{42}$
2 (LA)	155	4.25	6926	0.515	22.4	$156 \cdot 10^{42}$
3 (LA)	28.7	6.46	5152	1.4	5.6	$458 \cdot 10^{42}$
4 (TA)	898	0.99	5076	0.147	177	$9.4 \cdot 10^{42}$
5 (TA)	79.5	2.3	2063	1.03	38.5	$42.2 \cdot 10^{42}$
6 (TA)	11.1	2.75	721	2.8	15.4	$51.8 \cdot 10^{42}$
7 (O)	3.15	9.43	786	0.22	4	$24.9 \cdot 10^{42}$
8 (O)	3.8	8.92	1651	1.55	2.3	$219 \cdot 10^{42}$
9 (O)	4.58	8.43	1126	4.2	4.1	$397 \cdot 10^{42}$

the system

$$\kappa_x\left(\mathbf{r}\right) = \frac{1}{\left[T\left(x_{\mathrm{L}}\right) - T\left(x_{\mathrm{R}}\right)\right]} \frac{1}{L_y L_z} \int \mathbf{e}_x \cdot \mathbf{q}\left(\mathbf{r}\right) d^3\mathbf{r}. \tag{25}$$

3.4   Results

We performed spectrally resolved phonon transport simulations in two-dimensional planes of silicon of varying geometric size. We report heat flux, thermal conductivity, and the equilibrium temperature distribution. We used full phonon dispersion and density of states computed at room temperature from *ab initio* DFT simulations. Spatial domain sizes varied from 10 nm to 10 μm and were spatially discretized using coarse (C) and fine (F) triangular finite element meshes (Fig. 3.3). We employed S_4, S_8, and S_{16} Gauss-Legendre angular quadratures. We simulate a 1 K temperature gradient along the x-axis, with boundary temperatures of $T_{\mathrm{L}} = 301\,\mathrm{K}$, $T_{\mathrm{R}} = 300\,\mathrm{K}$. Reflecting conditions are placed on remaining boundaries. We use AMG-preconditioned GMRES [71, 121, 122] to solve the linear system of equations, with convergence criteria set to $\epsilon = 10^{-8}$. The selected four cases we discuss in this section were all simulated using S_8 quadrature with the fine spatial mesh.
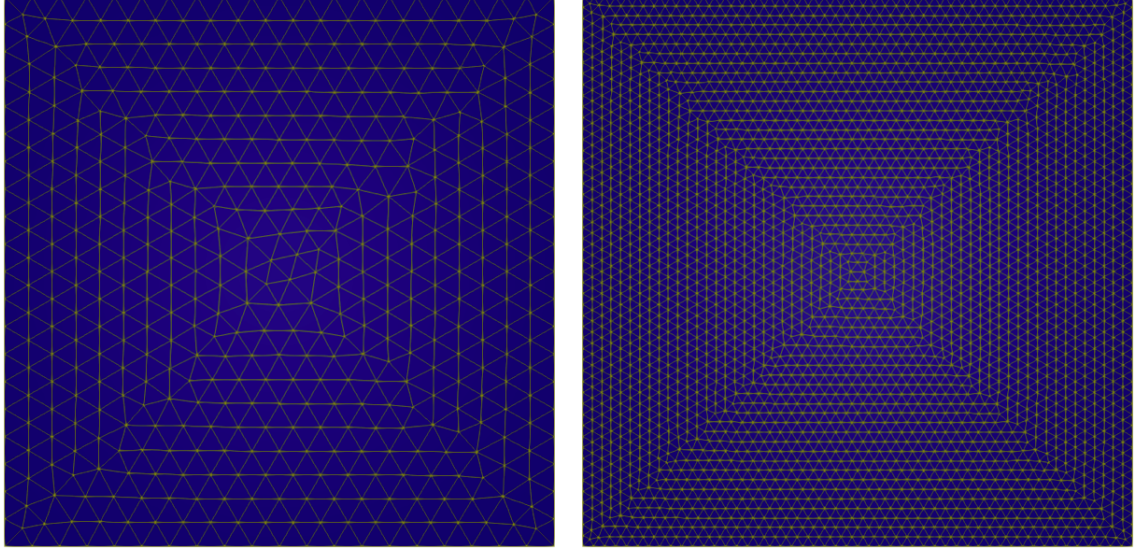
Figure 3.3: Coarse (left, 926 elements) and fine (right, 5770 elements) spatial meshes.

In centerline temperature profiles (Fig. 3.4), it is clear that non-equilibrium behavior arises when the domain is small, and this occurs because radiative equilibrium cannot be established. The incident phonon radiance from opposing sides encounter interference due to their proximity – the distance between hot and cold sources is less than the mean free path of the majority of phonons. This feature is prominent in smaller geometric domain sizes, exacerbated by the presence of ballistic phonons, which may undergo very few collisions before reaching the opposite side of the domain. An equilibrium solution to the temperature distribution exists upon numerical convergence of the simulation as the temperature distribution in each phonon mode is identical. However, if an equivalent transient simulation was conducted, the modal temperature distributions may not be identical. The temperature profiles produced from this work may provide a basis for the benchmarking of temperature distributions in molecular dynamics (MD) simulations, which rely on the careful selection of fitting parameters; the temperature profiles computed by

our method may aid in the accurate fitting of these parameters [123].
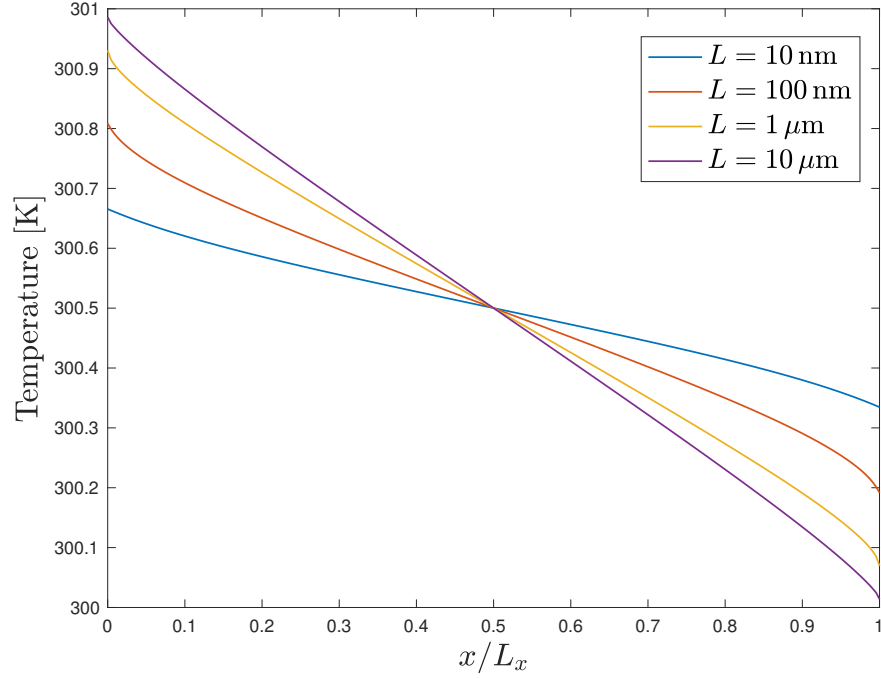
Figure 3.4: Centerline temperature distribution for four cases. Temperature slips at the boundaries are observed, and their magnitude diminishes in proportion to increasing domain size, as phonon boundary emission sources become further separated.

The closure term β (Fig. 3.5) provides a glimpse into the non-equilibrium behavior of the simulation at various domain sizes; β tightly couples the total phonon radiance (Φ^{00}) and total flux (Φ^{T}). We have shown β multiplied by the average relaxation time $\bar{\tau}$ in order to understand the fraction of total energy exchanged into the bath in one scattering event. The total amount of energy exchanged in β between Φ^{T} and Φ^{00} is infinitesimal relative to the total energy of the system, but without the presence of β conservation is broken, and a parabolic, rather than constant heat flux is observed.

Φ^{T} and Φ^{00} are not equivalent at small domain sizes; this occurs due to the disparity between the boundary emission source and the localized transport flux,

and it is no surprise that the majority of the curvature exhibited by β exists near the boundaries of Fig. 3.5. This artifact is a direct consequence of the system size, where emitting boundaries are in competition with each other. β exhibits a sign change, beginning negative at T_{L} and turning positive at T_{R}. In cases where $\beta < 0$, $\phi^{\mathrm{T}} > \phi^0$; ϕ^{T} is strongly influenced by the boundary conditions, where the incident angular intensity ψ is specified by the phonon radiance relation in Eq. (24). As phonons flow from hot to cold sides, the sign of β tends positive as $\phi^0 > \phi^{\mathrm{T}}$, after the spatial midpoint. This is because the local radiance ϕ^0 is now stronger than local transport flux ϕ^{T} – the cold boundary can not overcome the flow of phonons from the hot side, which results in a positive β, but also elevates the temperature away from the cold boundary shown on the profiles in Fig. 3.4. Blackbody phonon emission is very strong in proportion to the transport flux, and although overall convergence is achieved the localized non-equilibrium effect is very apparent, especially in smaller domain sizes.

Centerline total heat flux profiles for the $S_{8,F}$ case are shown in Fig. 3.6. As system size increases, heat flux decreases. Because of the flat heat flux profiles observed in all cases, it is clear that including β to close the transport equation is a necessity. Without β, energy leaks out of the system and yields a non-conserved heat flux. However, inspecting group heat flux paints a clear image of which groups carry the most heat in the system. It is, of course, the groups with the largest Λ, and those which remain the most ballistic over the entire geometric domain range. Figure 3.7 shows group heat flux for the $S_{8,F}$ case for all domain sizes. It is clear that larger values of $\Lambda_{p,\eta}$ are responsible for a higher heat flux; ballistic phonons carry energy further between collisions. The LA phonons are the dominant carriers due to their higher velocities and mean free path whereas TA and O phonons contribute
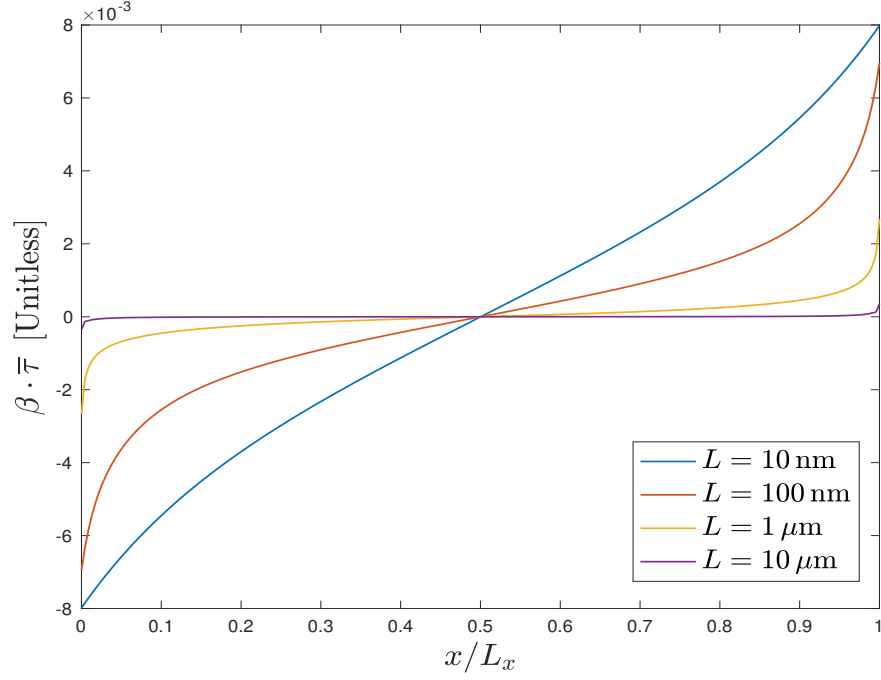
Figure 3.5: $\beta \cdot \overline{\tau}$ distributions along the x-axis for four domain sizes. As domain size increases, the behavior of β in the bulk tends toward zero as the total radiance (Φ^{00}) and total flux (Φ^{T}) come into balance and the influence of the heated boundaries subsides. The left boundary emits phonons at a higher temperature than the right boundary and so locally, $\phi^{T} > \phi^{0}$. The opposite is true on the right side of the figure, in proximity of the colder phonon source. The influence of β is directly affected by the size of the domain; with smaller domain sizes, the emissive sources are in greater competition with each other and radiative equilibrium can not be established.

lesser quantities. Acoustic phonons are generated by atomic displacements moving in phase, which is responsible for their higher velocity. Conversely, optic phonon motion is out of phase and are shorter range carriers. This phenomenon can be traced to Fig. 3.2, where larger magnitudes of the derivatives of the dispersion curves equate to higher wave propagation speed. Heat flux flattens out as geometric size increases, shown in Fig. 3.7; in this way we can analyze the degree to which the heat-carrying groups are affected by the change in domain size. If phonon groups were decoupled, the relation between heat flux and domain length would remain fixed in each group, as individual groups are not influenced by the average energy of the domain. However, in a coupled simulation the equilibrium distribution of each phonon channel is impacted by the average material temperature. Results for heat flux and thermal conductivity vary by approximately 3% between all angular and spatial resolutions. Thus, for a homogeneous material, a moderate angular and spatial resolution is sufficient for accurate results. This will likely change in heterogeneous environments such as porous materials, bulk material with dopants or inclusions (e.g. UO_2 with Xe bubbles), where ray effects have been observed in grey simulations [117].

Normalized spectral heat flux is shown in Fig. 3.8, giving insight into how rapidly each of the groups approach the ballistic limit. It is clear that q_1 (with $\Lambda_1 = 3120$ nm) carries the dominant portion of energy throughout the entire range of domain sizes, as it barely begins to approach the asymptotic limit at a length of 10 microns. However, it is overtaken early on by groups 2-5, until the domain sizes reaches about 1000 nm. As expected, the diffuse groups do not contribute appreciably to the overall heat flux.

Thermal conductivity for all cases is shown in Fig 3.9. The increasing angular
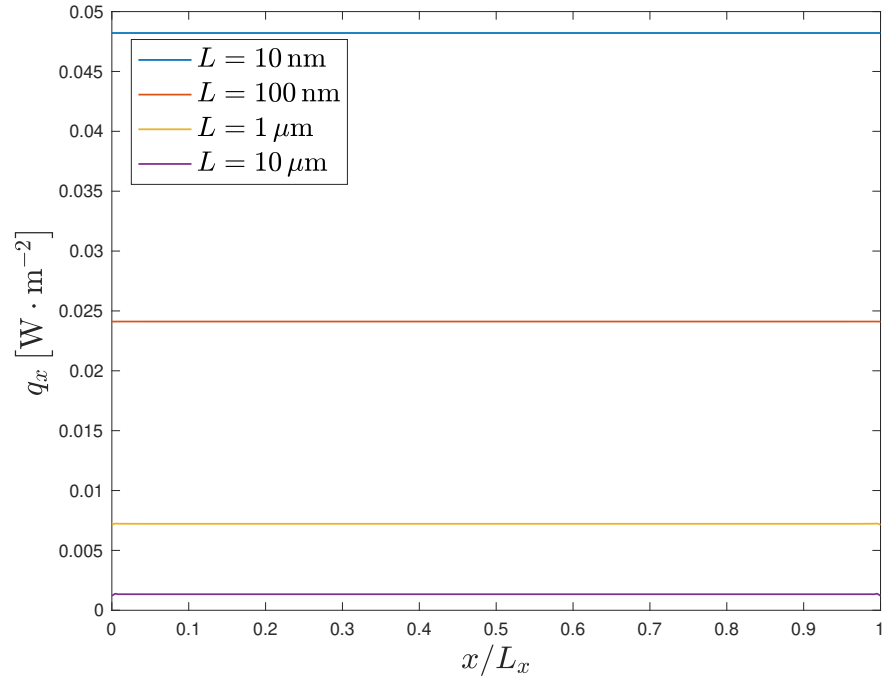
Figure 3.6: Centerline total heat flux for the $S_{8,F}$ case. Heat flux is approximately constant across the domain, with very minor fluctuations occurring at the hot and cold emitting boundaries. With increasing domain size, heat flux decreases.
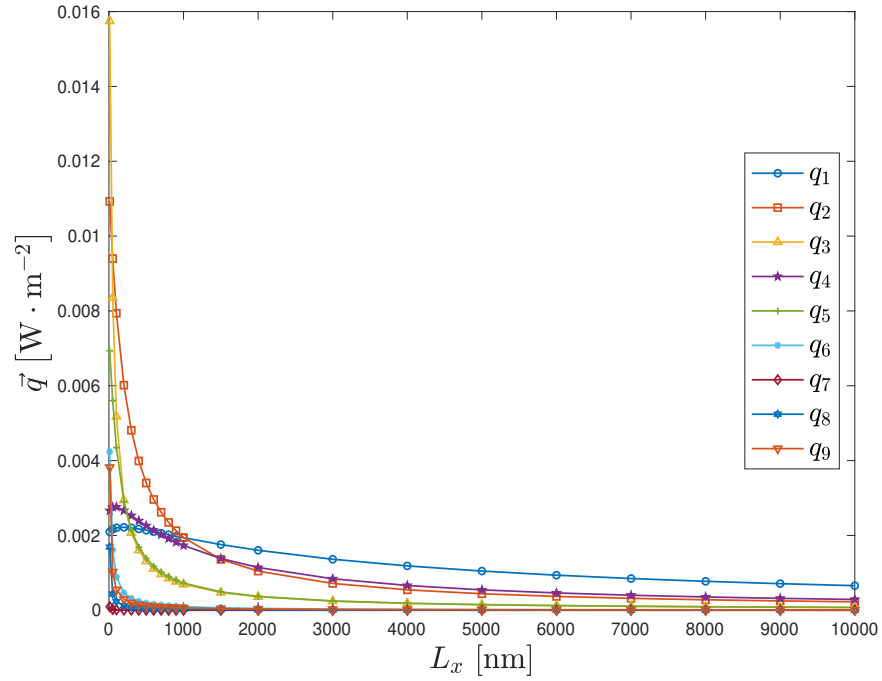
Figure 3.7: Group heat flux for each geometric domain size for the $S_{8,F}$ case. Groups 1-3 are LA, 4-6 are TA, and 7-9 are O. Diffuse groups (7, 8, 9) always carry low amounts of heat and remain relatively flat independent of domain size.
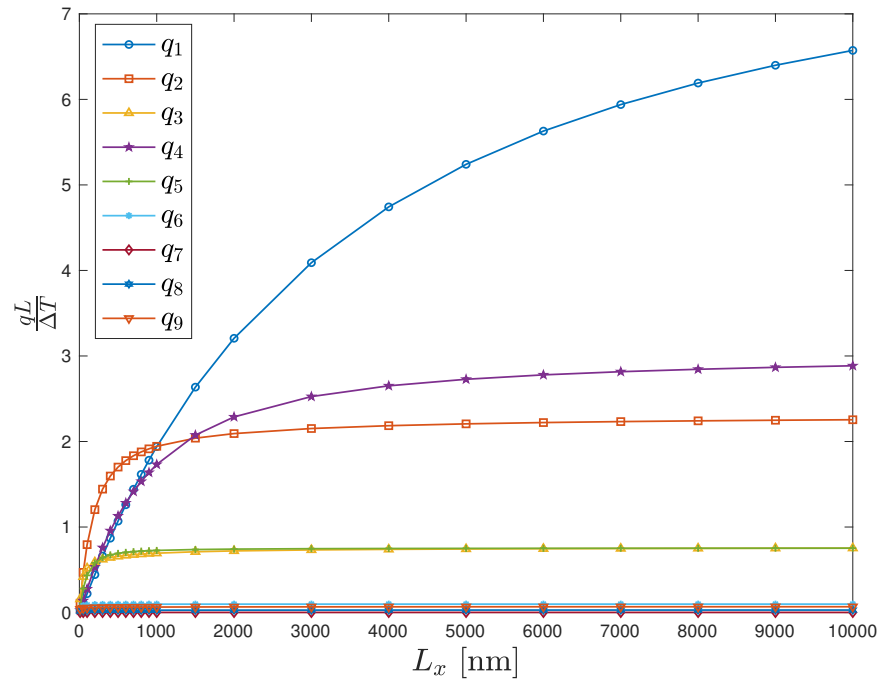
Figure 3.8: Normalized group heat flux ($S_{8,F}$ case); the ballistic limit is achieved rapidly by most of the phonon groups, with the exception of group 1 (largest Λ in the system).

refinements reduce heat flux and thermal conductivity by minute amounts, caused by additional information present due to a higher number of streaming directions. The sizes of the domains span 10 nm to 10 μm and κ_{eff} is proportional to this size. As domain size increases, κ_{eff} asymptotically approaches a bulk value of about $165\,\text{W}\cdot\text{m}^{-1}\cdot\text{K}^{-1}$, and many researchers have reported values for κ_{eff} with variation on the order of 100% [124]. As spatial and angular discretizations change, so do the values of spectral κ_{eff}. On smaller spatial meshes, $\Lambda_{p,\eta}$ tends to be ballistic per cell, even if they would be diffuse on the global domain. The coarse spatial discretization is acoustically thicker (more diffuse) where the fine spatial discretization is acoustically thinner (more ballistic). It is only as global domain increases in size that these groups become acutely diffuse, and their contribution to total heat flux becomes quite negligible; this trend is shown in Figs. 3.7 and 3.8. Table 3.2 contains the contributions from optic phonons to κ_{eff}, and they have a stronger effect in smaller global domains. For simulations with large (greater than 1 μm) domain sizes, omitting optic phonons would cause a dramatic decrease in the amount of iterations required to converge the solution, with negligible loss of accuracy (Table 3.2). Overall, it is more important to finely resolve spatial cell (finite element) size in comparison to angular resolution.

Comparisons of Φ^{00} and Φ^{T} are shown in Fig. 3.10. The distance between Φ^{00} and Φ^{T} are related to the magnitude of β, and intuitively, as domain size increases and the magnitude of β decreases, Φ^{00} and Φ^{T} should converge. However, for the 100 nm domain this is not the case; the two fluxes are further apart. Looking back to Fig. 3.7, there is a slight bump for groups 1 and 4, where heat flux experiences a slight rises rather than a monotonic decrease. Modal dominance of heat flux has an affect on the magnitude between Φ^{00} and Φ^{T} at 100 nm, where the system is still
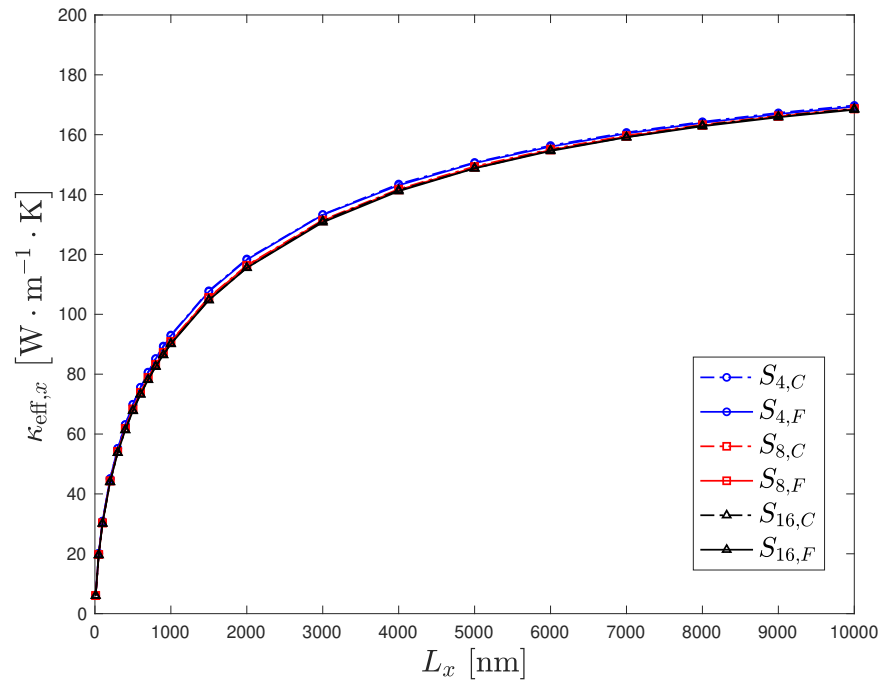
Figure 3.9: Thermal conductivity for various angular and spatial (F = fine, C = coarse) discretizations up to 10 μm. The overall difference between the extreme cases is about 3%.

sufficiently far from equilibrium. The same effect is present in domains up to 600 nm, after which the heat flux contribution from group 4 at 700 nm finally becomes less than the heat flux at 50 nm. This lag is caused by phonons in group 1 finally overtaking those from group 4; this transition happens in between 600 and 700 nm, and is observed in Fig. 3.8. As the geometric domain increases to the micrometer scale, Φ^{00} and Φ^{T} become increasingly convergent and their respective difference reduces to $< 1\%$. These criteria lead to the system being thrust into a state of equilibrium, compared to differences in the distributions on the nanometer scale where the system is far from equilibrium.
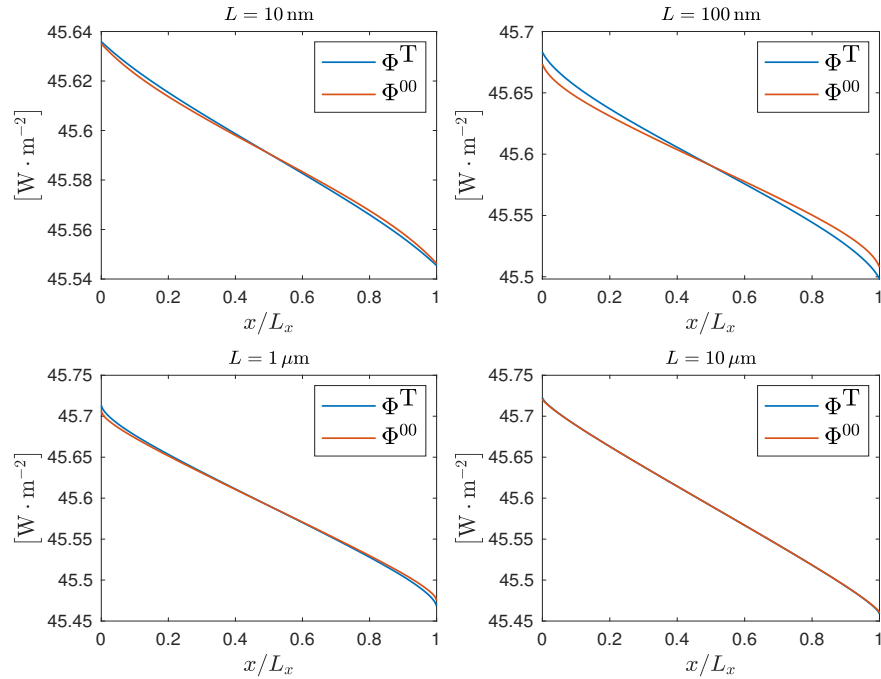
Figure 3.10: Total radiance (Φ^{00}) and transport flux (Φ^{T}) comparisons domain sizes between 10 nm and 10 μm using an S_8 quadrature. As the domain size increases, the systems relax to a more equilibrate state.

Phonon transport suffers from boundary scattering effects, and in systems which have strong non-equilibrium behavior, the boundaries can have a profound

influence on solution behavior a finite distance into the geometric domain. In our method, β has a strong gradient near any emitting boundary; both the equilibrium radiance and transport scalar flux are rapidly changing a finite distance away from a boundary. The magnitude of Φ^{T} near a boundary is a direct result of the boundary emission, where each outgoing ordinate of the angular intensity at an emissive boundary is assigned an incident phonon radiance (the adiabatic boundary condition). In turn, the magnitude of Φ^{00} depends on the solution of Φ^{T}, but will not be equivalent near a boundary at short geometric domains due to the influence of an opposing boundary emission. To combat the strong boundary effects, we applied adaptive mesh refinement (AMR) using a gradient jump indicator. The gradient jump criteria takes the gradient norm of any specified solution quantity (in this case, we chose β) at the face between a mesh element and its' neighbor element. The elements are sorted by increasing error, and the elements which fall into a specified tolerance are refined. As we used triangular finite elements, a single level of refinement splits one element into four smaller elements of equivalent area, and so on; we specified a maximum of two refinement levels. All refinement took place a finite distance from the emissive boundaries, shown in Fig. 3.11, where the gradient of β changes rapidly. The strongest boundary effects are observed in the 10 nm and 100 nm simulations, which is expected as phonons will nearly all be in the ballistic scattering regime at those domain sizes.

The planar temperature distribution for four length scale (10 nm, 100 nm, 1 μm, 10 μm) cases are shown in Fig. 3.12; domain size increases from (a) - (d). In small domain sizes, equilibrium is difficult to establish. Phonon flux on the hot side is suppressed by phonons incident from the cold side, which reduces temperature. As the geometric domain increases in size, the Fourier limit is recovered and heat
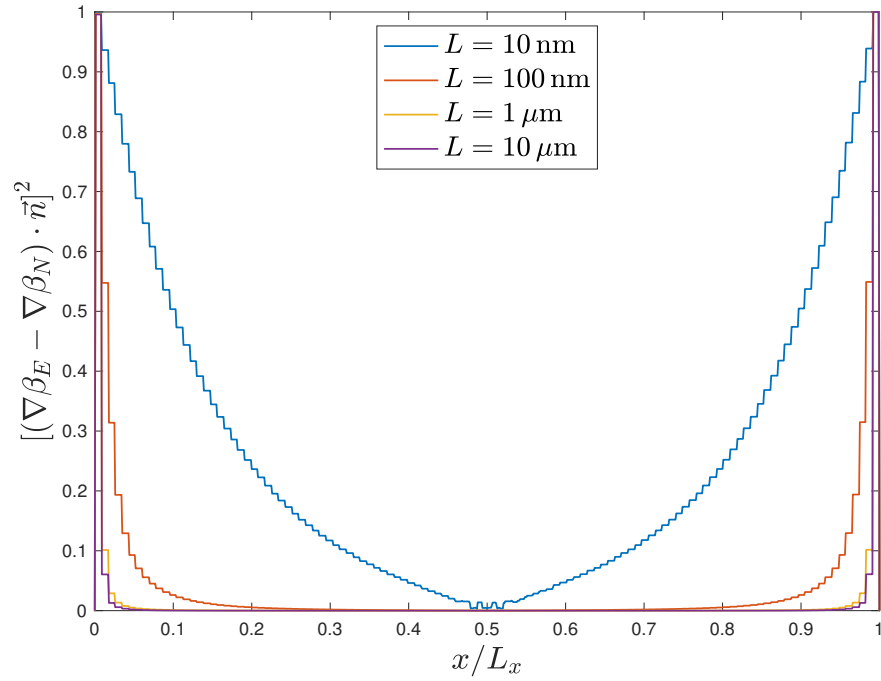
Figure 3.11: Normalized error from the AMR process. Differences in the solution gradient of β for various domain sizes. The strongest gradient jumps are observed near the edges, a result of the fixed boundary condition. For the 10 nm case, equilibrium is difficult to establish and the gradient of β continues to quickly change over most of the spatial domain. In larger domains, this effect persists about 10% of the distance away from the emitting boundaries.

transport exists in an almost purely diffusive regime.

Figure 3.12: The temperature distribution for four length scale (10 nm, 100 nm, 1 μm, 10 μm) cases in the x-y plane; domain size increases from (a) - (d). In small domain sizes, equilibrium is difficult to establish. Phonon flux on the hot side is suppressed by phonons incident from the cold side; in turn this reduces temperature. All legend scales are equal.

In Figure 3.13 the distribution of β is shown for various domain sizes. The relationship between a system unable to establish equilibrium (Fig. 3.13a) to one in an equilibrate state (Fig. 3.13d) is stark – β is nearly constant in large systems as the difference between Φ^{00} and Φ^{T} reduces. β also shows the effect of the fixed boundary temperature and the slight curvature effect present in the temperature distribution. The magnitude and sign of β also affect the convergence of the transport problem. Phonon transport simulations are classified as "purely scatterering" meaning the ratio of the mean free paths on the left and right hand sides of Eq. (20) are unity, and these physics cause convergence to lag in acoustically thick problems. The

presence of β affects the balance of Eq. (20), and in simulations where β is not approximately constant in the bulk, the disparity between Φ^{00} and Φ^{T} is also large, in correlation with Fig. 3.10. This energy redistribution was required to close the transport system – without its presence, we observed a non-conserved heat flux. The inclusion of β projects the residual energy; the phonon groups are analogous to networks of siphons drawing from a central plenum, the energy bath.
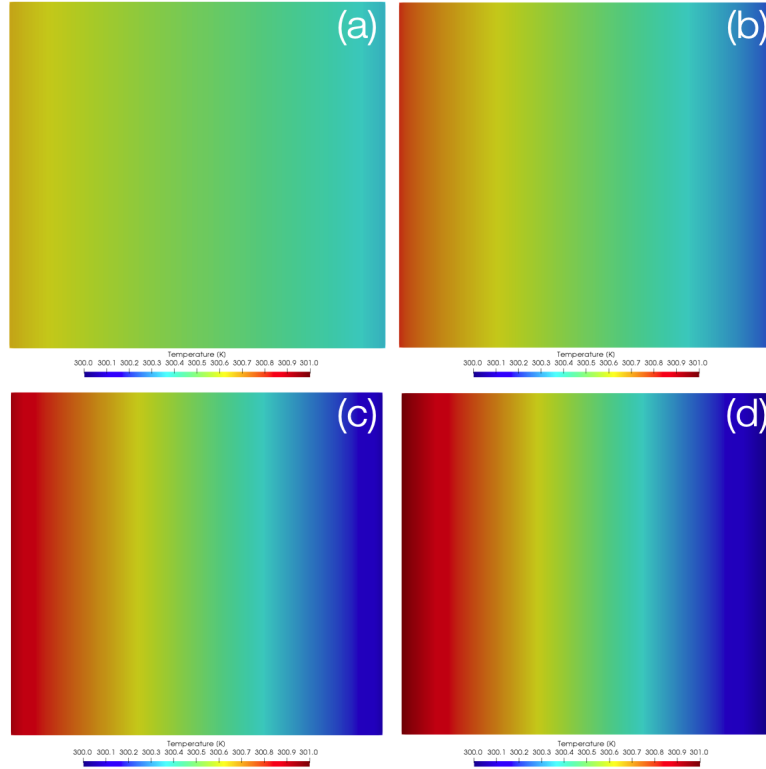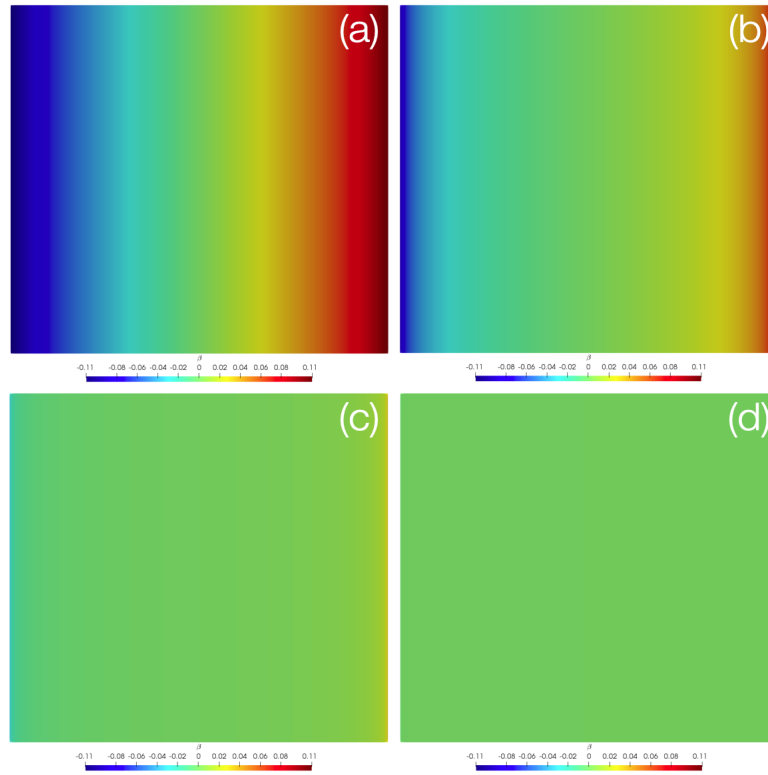

Figure 3.13: β distributions for four length scale (10 nm, 100 nm, 1 μm, 10 μm) cases in the x-y plane; domain size increases from (a) - (d). A measure of local thermodynamic equilibrium, β is nearly zero at large domain sizes, indicative of an established equilibrium. All legend scales are equal.

The ratio $\zeta_{p,\eta} = \frac{\mathcal{D}}{\Lambda_{p,\eta}}$ is the acoustic thickness of the domain ($\mathcal{D}$) with respect to mean free path per polarization and spectral group. The value of $\zeta_{p,\eta}$ changes in each group and polarization; certain group and mode polarizations are acoustically thick

and affect the convergence of the numerical simulation. Table 3.3 contains required iterations for each simulation and bounding values of $\zeta_{p,\eta}$ for the polarization and mode simulated. An increasing domain size requires more iterations to converge the solution, shown in Table 3.3. This is a consequence of the acoustic thickness; in the set $\{p, \Lambda_\eta\}$, the minimum value of Λ_η is the limiting factor. Due to the coupled nature of the transport simulation, the convergence performance of ballistic phonons is hindered by the diffuse phonons; in a decoupled simulation ballistic phonons converge much faster than diffuse phonons. The acoustic thickness in each polarization and mode are of primary interest in the numerical transport simulation. Depending on mode and polarization, $\Lambda_{p,\eta}$ can vary greatly due to its associated $v_{p,\eta}$ and $\tau_{p,\eta}$, affecting the acoustic thickness and causing significant degradation of numerical convergence, shown in Table 3.3. As optic phonons do not contribute significantly to thermal conductivity in these simulations, elimination of optic modes would reduce the overall amount of iterations; the simulation converges only as fast as its' slowest converging group. For the TA phonons, the implementation of an acceleration scheme such as diffusion synthetic acceleration (DSA) could reduce the required number of iterations.

One of the drawbacks of the coupled temperature method is the implicit dependency of all phonon channels; that is, if one or more of the channels is very diffuse, the simulations require many iterations to converge, if convergence is achieved at all. We have demonstrated convergence on domains ranging from 10 nm to 10 μm, but encountered significant decrease in efficiency when domain size increases to thousands of times the smallest value of Λ_η (large $\zeta_{p,\eta}$). This is expected, as phonons in diffuse channels are highly scattering. We have observed similar, slowly convergent behavior in previous decoupled transport simulations where Λ was small

compared to the domain size [56, 117]. The distinction in a coupled implementation is that ballistic phonons are throttled by the presence of diffuse phonons, and convergence behavior is significantly affected. The involvement of a numerical acceleration scheme such as nonlinear diffusion acceleration (NDA) may improve convergence properties; with NDA, the solution of a lower order (with no angular variable) diffusion problem informs a source term in a higher order transport problem. This is a proven technique in neutron transport [73, 74, 119, 125], but may require significant revision for use in a phonon transport simulation and is planned in a future study.

Zhang *et al.* simulate a similar temperature coupling through informing each discrete phonon group by the overall temperature of the domain, and were able to simulate large spatial domains, up to 100 μm [61]. However, they neglected optic phonons in their coupled simulations, and so convergence properties of their approach may be artificially positive as convergence of phonon transport problems is limited by the smallest value of Λ, e.g., the most diffuse phonon groups. Multiple researchers [112, 126–128] have cited the necessity in simulating optic phonons due to the acoustic-optic coupling effect found in various materials – all phonons are coupled through the total energy of the domain. The inclusion of optic phonons effectively places a muzzle on the TA and LA phonons and prevents them from carrying their maximal potential of heat. While we study Si, as did Zhang *et al.*, the development of this transport framework is desired to be general enough in its approach to be used in simulating materials which may have strong acousto-optic coupling effects.

We performed simulations isolating LA and TA phonons to gain insight into how much optic phonons contribute to κ_{eff} depending on the size of the geometric domain.

Table 3.2: Difference in κ_{eff} with and without optic phonons for $S_{8,F}$ simulation. Thermal conductivity is in units of $\left[\text{W} \cdot \text{m}^{-1} \cdot \text{K}^{-1} \right]$.

L [nm]	$\kappa_{\text{LA,TA,O}}$	$\kappa_{\text{LA,TA}}$	$\Delta\kappa\,(\%)$
10	6.1	5.2	14.8
100	30.3	28.2	6.9
1000	90.8	88.4	2.6
10000	168.6	166.7	1.1

Table 3.3: $S_{8,F}$ with LA, TA, O phonons.

L [nm]	GMRES Iterations	$\min\left(\zeta_{p,\eta}\right)$	$\max\left(\zeta_{p,\eta}\right)$
10	29	0.0032	3.175
100	59	0.032	31.75
1000	1276	0.32	317.5
10000	46600	3.2	3175

Table 3.2 shows the difference in κ_{eff} with and without optic phonon contribution. There is a nontrivial difference in κ_{eff} when domain size is small, but this effect diminishes as the simulation becomes more diffuse with increasing acoustic thickness. It is important to recognize the contribution of optic phonons in smaller spatial domains; at these sizes, optic phonons can exist "agnostically" between the ballistic and diffuse regimes. The presence of optic phonons causes significant degradation in the performance of the solver when comparing iterations between Table 3.3 and 3.4. While optic phonons may not be required in large simulation cells due to overshadowing influence of LA and TA phonons, it is nonetheless important to consider their contribution κ_{eff}, and subsequent effect on solver performance.

Table 3.4: $S_{8,F}$ with LA and TA phonons.

L [nm]	GMRES Iterations	min $(\zeta_{p,\eta})$	max $(\zeta_{p,\eta})$
10	28	0.0032	0.901
100	41	0.032	9.01
1000	114	0.32	90.1
10000	3306	3.2	901

3.5 Conclusions

We have developed a temperature coupled, spectral method for simulating effective thermal conductivity from nano- to micro-scale using material properties for homogeneous silicon obtained from *ab initio* density functional theory. In this study we simulated 2D geometric domains to characterize algorithmic and transport performance. The extension of this method to simulate three-dimensional structures is trivial, but will demand additional spatial and angular degrees of freedom. Angular degrees of freedom scale as $N(N+2)$ for 3D and $N(N+2)/2$ for 2D, where N is the chosen order of the discrete ordinates angular discretization. Spatial degrees of freedom scale with the nodal count in the selected finite element type, e.g., 3 nodes in 2D for a triangular element, 4 nodes in 3D for a tetragonal element. Computational cost will scale proportional to degrees of freedom in the equation system. We demonstrated correlation between the geometric dependency of heat flux and thermal conductivity, and our results for κ_{eff} in Si are in good agreement with those available in the open literature. Convergence properties are negatively impacted by the presence of optic phonons; the diffuse characteristics of optic phonons increase the acoustic thickness of simulations. A closure term, β, was developed to conserve the local system energy, and this fraction is projected as a source term in each phonon group, providing additional systemic coupling through the energy bath.

The range and sign of β indicates the degree of disorder between the transport system and the total energy of the phonon bath. In small geometric domains, the importance of using BTE simulations to model heat transport cannot be overstated; the difference between Φ^{T} and Φ^{00} is large where equilibrium cannot be established, and spatial effects dramatically change temperature distributions and heat flux. Previous works have shown optic phonons to contribute little to overall heat flux in silicon [17, 51, 61, 129]. However, geometric domains less than 100 nm in size (Table 3.2), and in devices where precision is critical, optic phonons should be included in simulation to accurately compute κ_{eff}. This work focused on purely homogeneous materials to characterize a new method, but our approach can be extended to bulk systems with voids (porous materials for thermoelectric devices) and heterogeneous systems (systems with inclusions, nuclear fuel with fission product defects) quite readily with the addition of an interface physics model. Subsequent improvement on this work would include simulation of transference between polarization branches, and the additional modeling of 3-phonon scattering through the relaxation time parameter included in the total relaxation time via Matthiessen's rule. We are currently developing diffusion acceleration techniques adapted from neutron transport methods in order to speed up convergence properties as domains become extremely acoustically thick.

Detailed thermal transport requires development of high precision tools with which to perform modeling and simulation efforts. In turn, these efforts can guide the design of nano- and micro-scale devices, and the prediction of thermal behavior at the engineering scale. Perturbations at the atomic-molecular scale drive changes in the microstructure; *ab initio* driven BTE simulations are a promising development in a scale-bridging framework, representing one element in the larger problem of

informing engineering scale simulations.

3.6 Declaration of Competing Interests

There are no conflict of interest in this work.

3.7 Acknowledgements

4   Iterative Performance of Spectral Phonon Transport Methods in Rattlesnake

Jackson R. Harter, Todd S. Palmer, P. Alex Greaney

4.1 Abstract

We have recently developed a deterministic, spectral phonon transport method, with temperature coupled Bose-Einstein source terms, implemented in the Rattlesnake code at Idaho National Laboratory. This method predicts thermal conductivity and equilibrium temperature distributions in homogeneous and heterogeneous materials using data generated by *ab initio* density functional theory methods. The equations associated with this method are solved via a modification of traditional source iteration. In this report, we compare the performance of source iteration applied to an existing uncoupled, traditional SAAF method to our new method and comment on the iterative performance of each. We observe ballistic and diffusive phonon scattering as acoustic thickness of the domain changes, and are able to make comparisons between the accuracy and efficiency of both methods.

4.2 Introduction

The rapid modernization of technology has seen an increased demand for micro- and nanoscale devices – apparati which can perform under extreme conditions at very small length scales. Computer processors (CPUs), cell phone technology, and thermoelectric devices all have the potential to be designed and machined to small length scales, but the limiting factor which constrains these devices is the dissipation of the heat they generate. With the desire to run large electrical currents through CPUs to yield high processor clock speeds [130, 131], or using thermoelectrics to generate electricity from waste heat [132], the ability of these devices to properly mitigate their generated heat is absolutely critical to their integrity, efficiency, and performance. The dominant energy carrier in the materials which compose these devices is the *phonon*, a lattice vibration induced by a

temperature perturbation [12, 14]. In addition to these semiconductor materials, phonons are also responsible for the majority of heat transfer in uranium dioxide (UO_2) nuclear fuel under irradiation, the fuel in nuclear power plants (NPPs). The size of the fuel in NPPs is generally much larger than the micro- and nanoscale dimensions of CPUs or thermoelectrics, and these materials are also more challenging in that isotopic defects – products generated by the nuclear fission process – are generated in the fuel and create obstacles for the scattering of phonons.

The Monte Carlo (MC) method is most commonly used for this purpose, as the random walk nature of the method can easily treat scattering physics and the phonon dispersion relation. However, a challenging aspect of the MC method is the Central Limit Theorem, as well as the small time step requirement if transient simulations are to be performed [60, 62, 133–135]. Because the phonon dispersion is nonlinear and varies over a wide range of frequencies, it can be difficult to incorporate into numerical solutions.

Bulk property prediction can be achieved using molecular dynamics (MD) or density functional theory (DFT) numerical models. These methods assume a known electronic potential and use this in either a fluctuation model (Green-Kubo method with MD or non-equilibrium MD [31, 34, 42]) or solve the full Schrödinger equation (DFT) [35, 36, 39, 40, 113, 114] and resolve the full phonon dispersion and density of states. MD and DFT methods are effective in predicting bulk properties, but are limited to very small problems; because of the computational restraint imposed by solving all the degrees of freedom in a perturbed atomic lattice, simulations are restricted to about 100,000 atoms, nowhere near enough to simulate a macroscopic quantity of interest.

By contrast, deterministic methods can provide an accurate answer in an efficient

manner by considering discrete phase space densities in place of individual particle tracking (as performed in MC methods) and discretizing the angular variable via the discrete ordinates method. The fully resolved phonon BTE is a function of 7 variables and is considerably difficult to solve, but these spatial and angular approximations can substantially reduce computation times. Deterministic methods have yielded accurate results for heat flux and thermal conductivity, and are efficient [57, 59, 61, 136, 137], but can be inaccurate in heterogeneous media if a sophisticated interface physics model is neglected. The full nonlinear phonon scattering source is also, in general, dealt with via the relaxation time approximation [11], as explicit collisions are difficult to model. Additionally, there have been no reliable developments for polarization branch transference. The relaxation time approximation is a reliable alternative to modeling the nonlinear scattering processes, but some loss of resolution is experienced as detailed scattering events are washed out through the use of this approximation. Deterministic phonon transport methods are an area of active development and, in general, yield results which are physical and in agreement with other methods [17, 51, 52, 57, 59, 61, 129, 138, 139].

We have previously developed a fully coupled method for predicting spectral thermal conductivity in dielectric materials [140], which uses the self-adjoint angular flux (SAAF) formulation of the phonon BTE, a second-order spatial method which possesses an elliptical streaming operator and implements a modified scattering source, the analytical phonon equilibrium radiance informed by a numerical temperature generated by the phonon angular intensity. We derived a new closure term, a residual energy projection, which preserves conservation of energy and generates a constant heat flux in the spatial domain [140]. Although our method produces a constant, conserved heat flux, we encountered a significant reduction

in numerical convergence properties as the geometric domain size (L) increased relative to the phonon mean free path (Λ) in homogeneous silicon [140]. We desire to apply our transport framework to simulate heterogeneous systems with models of thermoelectric devices and nuclear fuels with many defects and inclusions – at large (1 to 100 micron) scales – then pass an effective thermal conductivity to fuels performance codes to resolve engineering scale calculations. In these larger systems, numerical convergence was extremely slow and would be intractable in a development setting where thousands of parameterized simulations would be required in order to generate accurate predictions of fuel performance [29]. Thus, we seek numerical methods to *accelerate* our transport simulations. Because phonons are similar to neutrons and x-rays, we look to methods developed by the neutron and thermal radiation transport communities as a baseline.

In neutron and thermal radiation transport, the BTE is used to model nuclear reactors, experimental apparati, atmospheric transport and stellar particle transport [72, 73, 141]. The BTE is generally formulated to be solve via the method of *source iteration* (SI) [74], in which the solution of the left hand side of the equation for a primal, angular variable (such as the angular neutron or photon flux) is used to construct the particle scattering source term on the right hand side of the equation for the next iteration step. The standard SI method for the solution of the neutron transport equation is represented as

$$\mu \frac{\partial \psi^{(\ell+1/2)}}{\partial x} + \sigma_t \psi^{(\ell+1/2)} = \sigma_s \phi^{(\ell)} \tag{1a}$$

$$\phi^{(\ell+1/2)} = \frac{1}{2} \int_{-1}^{1} \psi^{(\ell+1/2)} d\mu \tag{1b}$$

$$\phi^{(\ell+1)} = \phi^{(\ell+1/2)}, \tag{1c}$$

where ℓ represents an iteration index, and the values are $\ell + 1/2$ are used to update the

source term for the following iteration. This procedure is repeated until convergence is reached. Traditional source iteration methods have been proven to work well in neutron and radiation transport, but break down when the *scattering ratio*, c, the ratio of the scattering cross section (σ_s) to total cross section (σ_t) approaches unity. Additionally, when the *optical thickness* of a material (the ratio of the spatial domain size $\mathcal{D}$ to the neutron or photon mean free path $\lambda = \frac{1}{\sigma_t}$) is large, convergence may also slow, as these particles are highly diffuse, meaning they will have many scattering events before being absorbed or leaking out of the system. A large scattering ratio and large optical thickness are significant barriers to convergence using the traditional SI method.

The *acoustic thickness* (ζ) of a material in phonon transport is analogous to the optical thickness, except that we use the phonon mean free path in place of the neutron or photon mean free path. The acoustic thickness is the inverse of the Knudsen (Kn) number, commonly associated with many phonon transport or fluid transport research. When ζ is large, it indicates that the phonon scattering regime will be diffuse, e.g., a phonon emitted by a hot material will scatter many times before it is absorbed by a colder material. Depending on the magnitude of ζ, this diffuse scattering will slow the numerical convergence of these simulations. Because of the complexity of the dispersion relation (and the presence of *optic* phonons), some phonon modes may be very diffuse and can severely impede numerical convergence on large spatial domains [140]. Phonon transport problems are also *purely scattering*, or $c = 1$: all phonon interaction events are treated as elastic or inelastic scattering (though in this current work, we treat only elastic scattering events) through the interaction term Λ.

4.3 Methods

4.3.1 First Order Form

The steady-state first (spatial) order form of our modified phonon BTE [140] under the relaxation time approximation [11] (RTA) is

$$\hat{\boldsymbol{\Omega}}\cdot\nabla\psi\left(\mathbf{r},\hat{\boldsymbol{\Omega}},\omega,p\right)+\frac{\psi\left(\mathbf{r},\hat{\boldsymbol{\Omega}},\omega,p\right)}{\Lambda\left(\omega,p\right)}=\frac{\phi_0\left(T\left(\mathbf{r}\right),\omega,p\right)}{4\pi}\left[\frac{1}{\Lambda\left(\omega,p\right)}-\frac{\beta\left[\phi_0,\phi_{\mathrm{T}}\right]}{\left|\mathbf{v}\left(\omega,p\right)\right|}\right]. \quad (2)$$

The *angular flux intensity*, ψ, is a parameterized function of the phonon's direction of propagation, $\hat{\boldsymbol{\Omega}}$, polarization p and frequency ω. The phonon polarization is its geometric orientation within the crystalline lattice, and can have either transverse (T) or longitudinal (L) modes. We study silicon (Si) in this manuscript, and therefore average the polarizations to three as a result of the crystal symmetry of Si. The phonon's *mean free path*, $\Lambda = \Lambda\left(\omega,p\right)$ is the product of the group velocity $v = \left|\mathbf{v}\left(\omega,p\right)\right|$ and relaxation time $\tau = \tau\left(\omega,p\right)$; it describes the average distance traveled by a phonon before a collision.

The steady-state, uncoupled first (spatial) order form of the traditional phonon BTE with the RTA applied is

$$\hat{\boldsymbol{\Omega}}\cdot\nabla\psi\left(\mathbf{r},\hat{\boldsymbol{\Omega}},\omega,p\right)+\frac{\psi\left(\mathbf{r},\hat{\boldsymbol{\Omega}},\omega,p\right)}{\Lambda\left(\omega,p\right)}=\frac{\phi_{\mathrm{T}}\left(\mathbf{r},\omega,p\right)}{4\pi\Lambda\left(\omega,p\right)}, \quad (3)$$

and the variables described are exactly the same as those in Eq. (2). The *transport scalar flux* (zeroth angular moment) is obtained by integrating the angular intensity over the 2D unit sphere

$$\phi_{\mathrm{T}}\left(\mathbf{r},\omega,p\right)=\int_{4\pi}\psi\left(\mathbf{r},\hat{\boldsymbol{\Omega}},\omega,p\right)d\Omega. \quad (4)$$

The *domain scalar flux* is the angle and frequency integrated angular flux intensity

summed over polarization

$$\Phi_{\mathrm{T}}\left(\mathbf{r}\right) = \sum_p \int_{4\pi} \int_\omega \psi\left(\mathbf{r}, \hat{\mathbf{\Omega}}, \omega, p\right) d\omega d\Omega, \tag{5}$$

and the total heat flux (first angular moment) is

$$\mathbf{q}\left(\mathbf{r}\right) = \sum_p \int_{4\pi} \int_\omega \hat{\mathbf{\Omega}}\,\psi\left(\mathbf{r}, \hat{\mathbf{\Omega}}, \omega, p\right) d\omega d\Omega. \tag{6}$$

The *average material temperature* is the integral over the spectral variable ω of all transport scalar flux inserted into an inverted Bose-Einstein distribution,

$$T\left(\mathbf{r}\right) = \int_\omega \frac{\hbar\omega}{k_{\mathrm{B}} \ln\left[\frac{\hbar\omega v \mathbb{D}}{\phi_{\mathrm{T}}(\mathbf{r})} + 1\right]} d\omega. \tag{7}$$

The *equilibrium radiance* is the integral of the temperature dependent Bose-Einstein distribution over the spectral variable ω, and describes the number of phonons at a certain mode and at a temperature

$$\phi_0\left(T\left(\mathbf{r}\right)\right) = \int_\omega \frac{\hbar\omega v \mathbb{D}}{e^{\frac{\hbar\omega}{k_{\mathrm{B}} T(\mathbf{r})}} - 1} d\omega \tag{8}$$

The residual energy projection term, $\beta\left[\phi_0\left(T\left(\mathbf{r}\right)\right), \phi_{\mathrm{T}}\left(\mathbf{r}\right)\right]$ was developed with the assumption of local thermodynamic equilibrium (LTE) [140] and is represented as the following

$$\beta\left[\phi_0\left(T\left(\mathbf{r}\right)\right), \phi_{\mathrm{T}}\left(\mathbf{r}\right)\right] = \frac{\int_\omega \int_{4\pi} \frac{\frac{\phi_0(T(\mathbf{r}))}{4\pi} - \psi\left(\mathbf{r}, \hat{\mathbf{\Omega}}\right)}{\Lambda} d\Omega d\omega}{\int_\omega \frac{\phi_0(T(\mathbf{r}))}{v} d\omega}, \tag{9}$$

We discretize Eqs. (2) and (3) in the spectral variable ω and collate the polarization index p into the *group* index g, giving a total number of discrete spectral groups G, and yielding the *multigroup* form of the coupled and uncoupled phonon BTE, respectively

$$\hat{\mathbf{\Omega}} \cdot \nabla \psi_g\left(\mathbf{r}, \hat{\mathbf{\Omega}}\right) + \frac{\psi_g\left(\mathbf{r}, \hat{\mathbf{\Omega}}\right)}{\Lambda_g} = \frac{\phi_{0,g}\left(T\left(\mathbf{r}\right)\right)}{4\pi}\left[\frac{1}{\Lambda_g} - \frac{\beta\left[\phi_0, \phi_{\mathrm{T}}\right]}{v_g}\right], \qquad g = 1, \dots, G, \tag{10}$$

$$\hat{\mathbf{\Omega}} \cdot \nabla \psi_g\left(\mathbf{r}, \hat{\mathbf{\Omega}}\right) + \frac{\psi_g\left(\mathbf{r}, \hat{\mathbf{\Omega}}\right)}{\Lambda_g} = \frac{\phi_{\mathrm{T},g}\left(\mathbf{r}\right)}{4\pi\Lambda_g}, \qquad g = 1, \dots, G. \tag{11}$$

In subsequent derivations and sections, we drop variable notation to conserve space, but retain the temperature notation to describe where angular intensity and equilibrium radiance exhibit coupling.

4.3.2 SAAF Form

We derive the SAAF form of the coupled and uncoupled equations, beginning with the coupled version. Solve Eq. (2) for angular intensity

$$\psi_g = \frac{\phi_{0,g}\left(T\left(\mathbf{r}\right)\right)}{4\pi} - \frac{\Lambda_g \beta\left[\phi_0, \phi_{\mathrm{T}}\right]\phi_{0,g}\left(T\left(\mathbf{r}\right)\right)}{4\pi v_g} - \Lambda_g \hat{\mathbf{\Omega}} \cdot \nabla \psi_g, \tag{12}$$

and substitute this expression into the gradient term of Eq. (2),

$$\hat{\mathbf{\Omega}} \cdot \nabla \left[\frac{\phi_{0,g}\left(T\left(\mathbf{r}\right)\right)}{4\pi} - \frac{\Lambda_g \beta\left[\phi_0, \phi_{\mathrm{T}}\right]\phi_{0,g}\left(T\left(\mathbf{r}\right)\right)}{4\pi v_g} - \Lambda_g \hat{\mathbf{\Omega}} \cdot \nabla \psi_g\right] + \frac{1}{\Lambda_g}\psi_g =$$

$$\frac{\phi_{0,g}\left(T\left(\mathbf{r}\right)\right)}{4\pi\Lambda_g} - \frac{\beta\left[\phi_0, \phi_{\mathrm{T}}\right]\phi_{0,g}\left(T\left(\mathbf{r}\right)\right)}{4\pi v_g}, \tag{13}$$

$$-\Lambda_g \hat{\mathbf{\Omega}} \cdot \nabla \left[\hat{\mathbf{\Omega}} \cdot \nabla \psi_g\right] + \frac{1}{\Lambda_g}\psi_g = \frac{1}{4\pi}\left[\frac{\phi_{0,g}\left(T\left(\mathbf{r}\right)\right)}{\Lambda_g} - \hat{\mathbf{\Omega}} \cdot \nabla \phi_{0,g}\left(T\left(\mathbf{r}\right)\right) + \right.$$

$$\left. \hat{\mathbf{\Omega}} \cdot \nabla \frac{\Lambda_g \beta\left[\phi_0, \phi_{\mathrm{T}}\right]}{v_g}\phi_{0,g}\left(T\left(\mathbf{r}\right)\right) - \frac{\beta\left[\phi_0, \phi_{\mathrm{T}}\right]}{v_g}\phi_{0,g}\left(T\left(\mathbf{r}\right)\right)\right]. \tag{14}$$

We follow a similar process for Eq. (11) to derive

$$-\Lambda_g \hat{\mathbf{\Omega}} \cdot \nabla \left[\hat{\mathbf{\Omega}} \cdot \nabla \psi_g\right] + \frac{1}{\Lambda_g}\psi_g = \frac{1}{4\pi}\left[\frac{\phi_{\mathrm{T},g}\left(\mathbf{r}\right)}{\Lambda_g} - \hat{\mathbf{\Omega}} \cdot \nabla \phi_{\mathrm{T},g}\left(\mathbf{r}\right)\right]. \tag{15}$$

Now that the SAAF forms of the equations have been derived, we will show how these equations are solved using Source Iteration (SI) [74] and a modified SI (MSI).

When a transport solve is performed, the angular flux intensity is updated, $\psi^{(\ell+1/2)}$, and so is the transport scalar flux

$$\hat{\boldsymbol{\Omega}} \cdot \nabla \psi_g^{(\ell+1/2)} + \frac{1}{\Lambda} \psi_g^{(\ell+1/2)} = \frac{\phi_{\mathrm{T},g}^{(\ell)}(\mathbf{r})}{4\pi\Lambda_g} \tag{16}$$

$$\phi_{\mathrm{T},g}^{(\ell+1/2)}(\mathbf{r}) = \int_{4\pi} \psi_g^{(\ell+1/2)}\left(\mathbf{r}, \hat{\boldsymbol{\Omega}}\right) d\Omega \tag{17a}$$

$$\phi_{\mathrm{T},g}^{(\ell+1)}(\mathbf{r}) = \phi_{\mathrm{T},g}^{(\ell+1/2)}(\mathbf{r}), \tag{17b}$$

and this process is repeated until convergence is achieved.

With the coupled formulation of the BTE, we have a modified approach to the traditional SI method. Instead of directly simulating scattering using ϕ_T on the RHS of the transport equation, we use the transport scalar flux to determine a local system temperature, which we use to set the strength of the equilibrium radiance, and the residual energy projection. The flux intensity is updated the same way as in Eq. (17a). Once this is obtained, the average material temperature (which depends on the transport scalar flux) is expressed as

$$T^{(\ell+1)}(\mathbf{r}) = \frac{1}{G}\frac{\hbar}{k_\mathrm{B}} \sum_{g=1}^{G} \omega_g \left[\ln \left[\frac{\hbar\omega_g v_g \mathbb{D}_g}{\phi_{\mathrm{T},g}^{(\ell+1)}} + 1 \right] \right]^{-1}, \tag{18}$$

the in-group equilibrium radiance

$$\phi_{0,g}^{(\ell+1)}(T(\mathbf{r})) = \frac{\hbar\omega_g v_g \mathbb{D}_g}{\exp\left[\frac{\hbar\omega_g}{k_\mathrm{B} T^{(\ell+1)}(\mathbf{r})}\right] - 1}, \tag{19}$$

and finally the residual energy projection β

$$\beta^{(\ell+1)}[\phi_0, \phi_\mathrm{T}] = \frac{\sum_g \frac{\phi_{0,g}^{(\ell+1)}(T(\mathbf{r})) - \phi_{\mathrm{T},g}^{(\ell+1)}}{\Lambda_g}}{\sum_g \frac{\phi_{0,g}^{(\ell+1)}(T(\mathbf{r}))}{v_g}}. \tag{20}$$

It is imperative to understand that the updated values of temperature $T^{(\ell+1)}$, source $\phi_g^{0,(\ell+1)}$ and redistribution $\beta^{(\ell+1)}$ all depend on the previous iteration's value of

$\psi^{(\ell+1/2)}$. In this way, there is a complex dependency of variables. Ordinarily, this would seem like a very simple problem in a neutron transport simulation; a fixed source problem without a scattering interaction. However, a complication here is that the source terms are dependent on the solution of the left hand side, which is why we must iterate. The key quality in the modified SI method is that we do not use ϕ_{T}, but instead used terms *derived* from it, in the source.

4.3.3 Boundary Conditions

The incident angular flux and reflecting boundary conditions for this transport equation are defined as:

$$\psi\left(\mathbf{r}_b\right) = \begin{cases} \psi^{\mathrm{inc}}\left(\mathbf{r}_b, \hat{\mathbf{\Omega}}\right), \hat{\mathbf{\Omega}} \cdot \bar{\mathbf{n}}_b < 0 \\ \psi^{\mathrm{ref}}\left(\mathbf{r}_b, \hat{\mathbf{\Omega}}_r\right), \hat{\mathbf{\Omega}} \cdot \bar{\mathbf{n}}_b < 0 \end{cases},$$

here, $\bar{\mathbf{n}}_b$ is the outward unit normal at a point $\mathbf{r}_b$ on the boundary. In neutron transport space, ψ^{inc} implies an incident neutron flux boundary condition. In this implementation, we use this boundary as an adiabatic boundary to specify an incident source of phonons, e.g., $\psi(\mathbf{r}_b, \hat{\mathbf{\Omega}}) = \phi^0\left(\mathbf{r}_b\right)$ (for the coupled equations) or $\psi(\mathbf{r}_b, \hat{\mathbf{\Omega}}) = \phi^{\mathrm{T}}\left(\mathbf{r}_b\right)$ (for the uncoupled equations). The reflective angle $\hat{\mathbf{\Omega}}_r$ in ψ^{ref} is

$$\hat{\mathbf{\Omega}}_r = \hat{\mathbf{\Omega}} - 2\left(\hat{\mathbf{\Omega}} \cdot \bar{\mathbf{n}}_b\right)\bar{\mathbf{n}}_b.$$

Using the material properties, we compute radiant emission sources on the boundaries, driven by a prescribed temperature boundary condition,

$$\phi_{0,g}\left(T\left(\mathbf{r}_b\right)\right) = \frac{\hbar\omega_g \left|\mathbf{v}_g\right| \mathbb{D}_g}{\exp\left[\frac{\hbar\omega_g}{k_{\mathrm{B}}T(\mathbf{r}_b)}\right] - 1}. \tag{21}$$

Equation (21) is used by the incident flux condition at a boundary $\mathbf{r}_b$ to supply a source of phonons for a given group and polarization. We compute an effective

thermal conductivity along a direction by taking the ratio of the total heat flux to the end-to-end temperature gradient (which includes boundary effects) in the system

$$\kappa_x\left(\mathbf{r}\right) = \frac{1}{\left[T\left(x_{\mathrm{L}}\right) - T\left(x_{\mathrm{R}}\right)\right]} \frac{1}{L_y L_z} \int \mathbf{e}_x \cdot \mathbf{q}\left(\mathbf{r}\right) d^3 \mathbf{r}. \tag{22}$$

4.3.4   Iteration Algorithms

Algorithm 2: Temperature coupled, modified source iteration (MSI) algorithm

---

1 initialize $\phi_{0,g}^{(\ell)}\left(\mathbf{r}_b\right), \psi_{m,g}^{(\ell)}\left(\mathbf{r}\right), \phi_{\mathrm{T},g}^{(\ell)}\left(\mathbf{r}\right), \phi_{0,g}^{(\ell)}\left(\mathbf{r}\right), T^{(\ell)}\left(\mathbf{r}\right)$, set convergence ε

2 **while** $\left|\frac{\phi_{T,g}^{(\ell+1)}(\mathbf{r}) - \phi_{T,g}^{(\ell)}(\mathbf{r})}{\phi_{T,g}^{(\ell+1)}(\mathbf{r})}\right| > \varepsilon$ **do**

3 $\quad$ **for** $g = 1$ *to* G **do**

4 $\quad\quad$ **for** $m = 1$ *to* M **do**

5 $\quad\quad\quad$ solve coupled SAAF-BTE (Eq. 14) for $\psi_{m,g}^{(\ell+1/2)}$

6 $\quad\quad$ **end**

7 $\quad$ **end**

8 $\quad$ compute $\phi_{\mathrm{T},g}^{(\ell+1)}\left(\mathbf{r}\right)$ and solve for $T^{(\ell+1)}\left(\mathbf{r}\right)$

9 $\quad$ compute $\phi_{0,g}^{(\ell+1)}\left(T\left(\mathbf{r}\right)\right), \beta^{(\ell+1)}$

10 **end**

Algorithm 3: Traditional source iteration (SI) algorithm

---

1 initialize $\psi_m^{(\ell)}\left(\mathbf{r}\right)$, set convergence ε

2 **while** $\left|\frac{\phi_{T,g}^{(\ell+1)}(\mathbf{r}) - \phi_{T,g}^{(\ell)}(\mathbf{r})}{\phi_{T,g}^{(\ell+1)}(\mathbf{r})}\right| > \varepsilon$ **do**

3 $\quad$ **for** $g = 1$ *to* G **do**

4 $\quad\quad$ **for** $m = 1$ *to* M **do**

5 $\quad\quad\quad$ solve uncoupled SAAF-BTE (Eq. 15) for $\psi_{m,g}^{(\ell+1/2)}$

6 $\quad\quad$ **end**

7 $\quad$ **end**

8 $\quad$ compute $\phi_{\mathrm{T},g}^{(\ell+1)}\left(\mathbf{r}\right)$

9 **end**

In both methods, convergence is tested by comparing the successive values of

the scalar flux in each group

$$\left\|\phi_T^{(\ell+1)} - \phi_T^{(\ell)}\right\|_\infty < \epsilon \, (1 - \rho) \left\|\phi_T^{(\ell+1)}\right\|_\infty, \tag{23}$$

where ϵ is a prescribed convergence criteria, set in this study to be $\epsilon = 10^{-6}$, and ρ is the spectral radius of the problem,

$$\rho \approx \frac{\left\|\phi_T^{(\ell+1)} - \phi_T^{(\ell)}\right\|_\infty}{\left\|\phi_T^{(\ell)} - \phi_T^{(\ell-1)}\right\|_\infty}, \tag{24}$$

which is shown in Adams [119]. The infinity norm $\|\|_\infty$ is the maximum value in an arbitrary vector $\mathbf{x}$

$$|\mathbf{x}|_\infty = \max_i |x_i| \tag{25}$$

The spectral radius (the magnitude of the largest eigenvalue in an iteration matrix) tells us how fast an iteration converges; the error is reduced by a factor of ρ each iteration, with asymptotic behavior – a measure of the convergence rate. Applying this criteria helps guard against "false convergence", where in slowly convergent simulations, two successive iterates may be close enough to exhibit the illusion of convergence. The SI scheme has been used in the nuclear engineering community for decades, and is a reliable, efficient method of solution for problems for which particles are in the ballistic regime, and optically (acoustically) thin, meaning the particles are likely to exit the system ("leak") after a few collisions. As systems become more diffuse (acoustically thick), the SI scheme converges very slowly and is inefficient [119].

4.3.5 Four Group Data Set

We computed material properties for silicon from density functional theory, discretized in four groups of spectral properties to simplify and test the iterative

Table 4.1: Four-group silicon material properties.

G	Λ [nm]	$\overline{\omega} \cdot 10^{13}$ $[s^{-1}]$	$\overline{v}$ [m$\cdot$s^{-1}]	$\overline{\mathbb{D}} \cdot 10^{18}$ [m^{-3}]	$\overline{\tau}$ [ps]
1 (LA)	3120	1.49	8079	0.0736	386
4 (TA)	898	0.99	5076	0.147	177
5 (TA)	79.5	2.3	2063	1.03	38.5
9 (O)	4.58	8.43	1126	4.2	4.1

performance of our methods. The original data set was 9 groups, and is from our earlier work [140]. The group descriptions cover all phonon modes, with the fundamental property of interest (Λ) spanning 3 orders of magnitude. By selecting these data, we will be able to comment on the iterative performance of the methods and the effectiveness of the coupling in the modified SI method. Phonons with larger group velocity and mean free path carry more energy; the opposite is true for phonons with a lower group velocity and mean free path.

4.4 Results

To characterize the performance of the two methods, we generated two test problems. It is not expected that the two methods will yield the same solutions to these test problems, as governing equations are different. However, the governing equations and methodology are similar, and the results of each method (SI and MSI) should also be similar.

4.4.1 Test Problem A

Problem A is defined as follows: 2D geometric domains varying between 10 nm and 10 μm, with continuous finite element spatial discretizations of 1, 10, 100, and 1000 QUAD4 finite elements in the x and y direction, yielding a total element count

of 1, 10^2, 10^4, and 10^6 equally spaced cells per mesh, respectively. For all variations of this problem, the S_8 level symmetric angular quadrature was used, which contains 40 angular ordinates per simulation. The iterative convergence criteria is $\varepsilon = 10^{-6}$, with a temperature difference imposed by boundary temperatures of $T_L = 301\text{K}$ and $T_R = 300\text{K}$. Scalar flux and equilibrium radiance in each group are initialized to 1. Two phonon groups (groups 1 and 4) were used in this simulation. The notation SI means "source iteration" and MSI means "modified source iteration". The goal of this effort is to understand the performance of the two computational methods as the spatial mesh cells change size, and the mean free path of the phonons per cell varies.

The MSI scheme takes fewer iterations and less CPU time to converge compared to the SI scheme, most likely due to the coupling of the groups; iterations and CPU time are shown in Figs 4.1 and 4.2, respectively. The convergence properties are improved due to the coupling, because the Λ are essentially averaged over the groups — where one group might be exceptionally slow to converge (due to its acoustic thickness). We believe there is phonon 'throttling' occurring when the Λ_g becomes highly disparate and ranges over two to three orders of magnitude. This phenomenon can be beneficial depending on the scattering regime and the size of the system. This effect has a twofold contribution: the phonon source is a proper non-equilibrium Bose-Einstein distribution, coupled in temperature through the angular flux intensity of the transport system; and because of the inter-group communication, convergence may be improved in a system with a large range in the spectral Λ, which we will report more on for test problem B. Traditional SI will converge slower because the phonon groups are completely uncoupled, and only within group scattering is simulated. The physics of β induce a feedback effect into

the simulation; β tells us how far out of equilibrium we are locally, and if so, that fraction of energy is injected back into the system, which helps bring the system back into balance.

In Figs. 4.3 – 4.5, an anomaly is present for the N_{msi} case with 10^6 elements – the average heat flux exhibits a much different trend, and much higher value, than the other cases with a more coarse spatial discretization for the MSI algorithm. We believe all results for the N_{msi} case with 10^6 elements to be incorrect, and an outlier to our suite of tests. This occurs even though the data are consistent across all input files. Table 4.2 shows overall acoustic thickness of the problem for each group, for each domain size. As size increase, the problem becomes more acoustically thick and requires more iterations to converge. The MSI algorithm outperforms SI for a 2 group problem, requiring fewer iterations and less CPU time to converge. MSI has the most benefit at larger acoustic thicknesses, but is comparable to SI when problems are acoustically thin, as well.

We show CPU time and iterations against MFP/cell for Λ_1 and Λ_2, Figs. 4.6 - 4.8. As the MFP/cell increases for each domain size, so do the total amount of iterations – this is expected. However, the MSI method converges in fewer iterations than the traditional SI method.
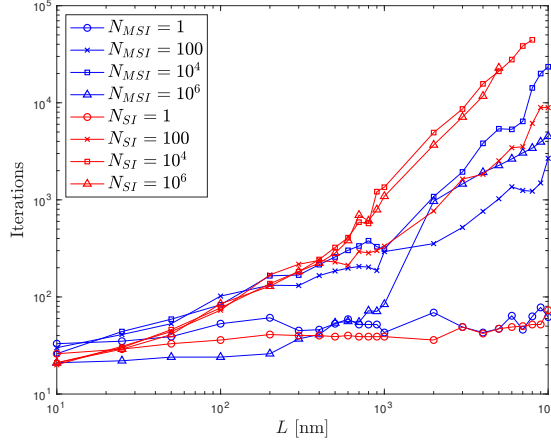
Figure 4.1: Iteration comparison between SI and MSI methods for various spatial discretizations.
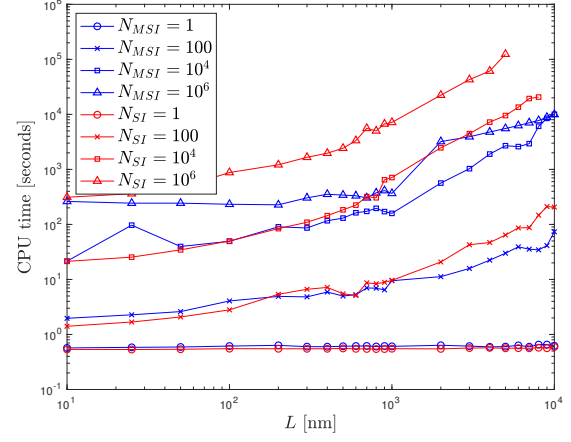
Figure 4.2: CPU time comparison between SI and MSI methods for various spatial discretizations.
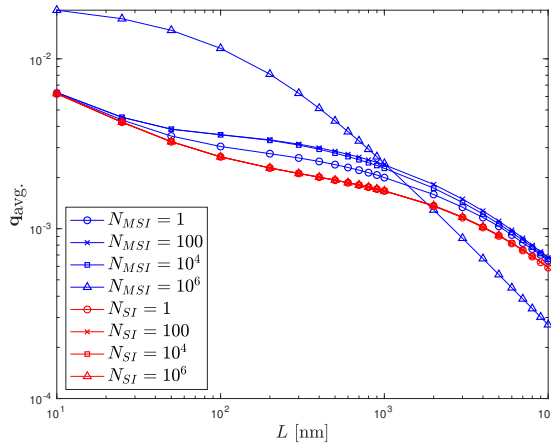
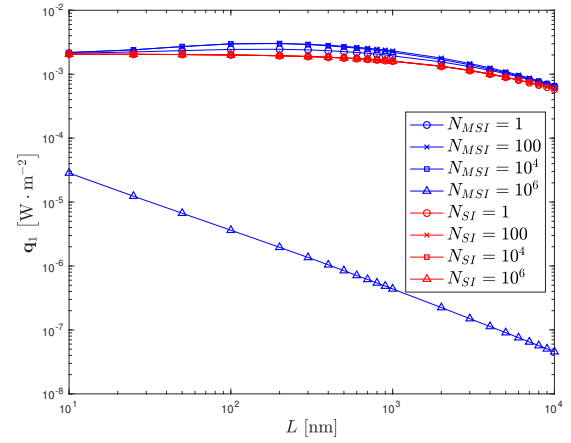Figure 4.3: Average heat flux for all spatial discretizations over all geometric domain sizes

Figure 4.4: Average heat flux in group 1 for all spatial discretizations over all geometric domain sizes
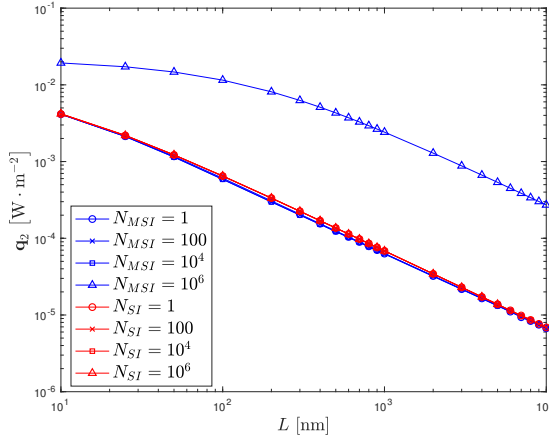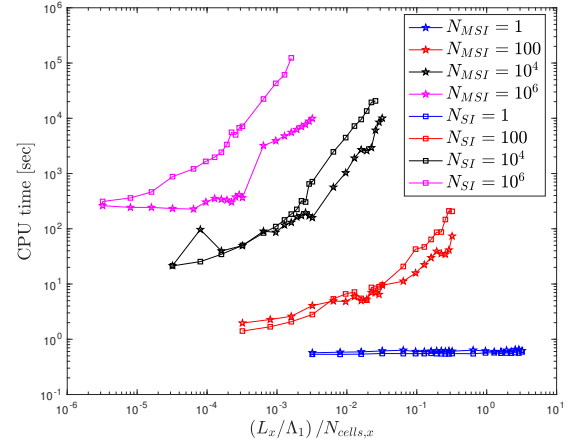
Figure 4.5: Average heat flux in group 2 for all spatial discretizations over all geometric domain sizes

Figure 4.6: CPU time vs. cell size (in MFP per geometric domain for Λ_1)
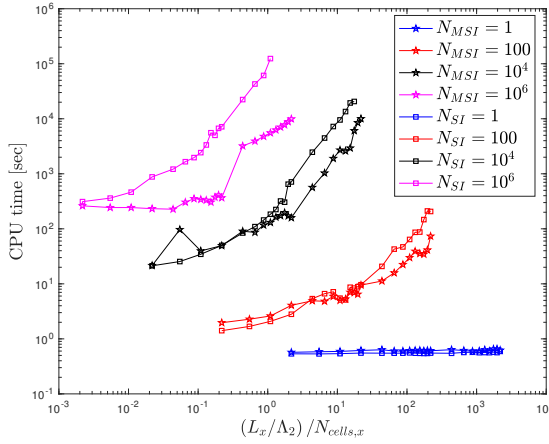
Figure 4.7: CPU time vs. cell size (in MFP per geometric domain for Λ_2)
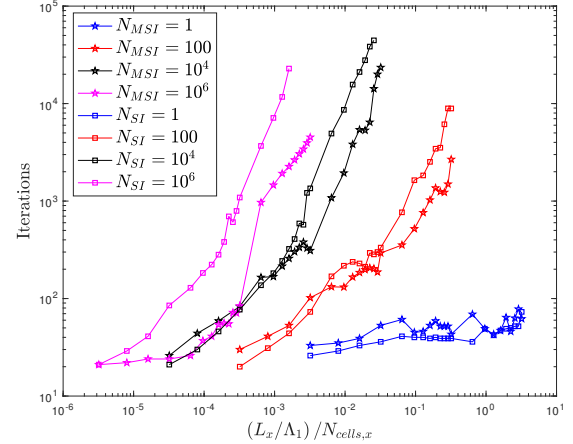
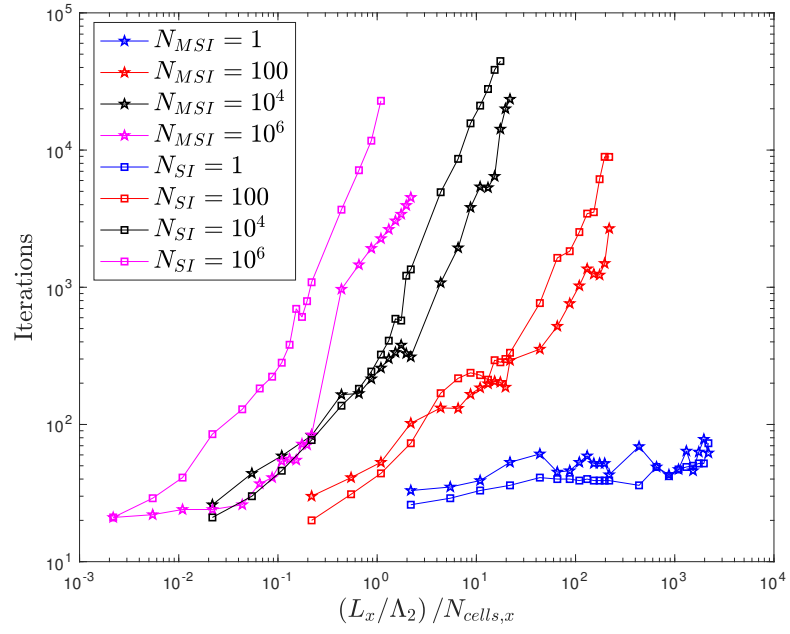Figure 4.8: Iterations vs. cell size (in MFP per geometric domain for Λ_1)

Figure 4.9: Iterations vs. cell size (in MFP per geometric domain for Λ_2)

Table 4.2: 2-group: ζ_g, iterations, $\mathbf{q}_{\text{avg.}}^{\text{SI}}/\mathbf{q}_{\text{avg.}}^{\text{MSI}}$. Case: S_8, $N = 100$

L [nm]	ξ_1	ξ_2	Its$_{\text{SI}}$	Its$_{\text{MSI}}$	$\mathbf{q}_{\text{avg.}}^{\text{SI}}/\mathbf{q}_{\text{avg.}}^{\text{MSI}}$
10	0.003	2.2	20	30	0.9871
25	0.008	5.5	31	41	0.9359
50	0.016	11	44	53	0.8442
100	0.032	22	73	102	0.7405
200	0.064	44	169	132	0.6830
300	0.096	66	217	131	0.6724
400	0.128	87	238	166	0.6724
500	0.160	109	229	185	0.6759
600	0.192	131	212	198	0.6806
700	0.224	153	294	206	0.6860
800	0.256	175	284	203	0.6916
900	0.289	197	300	187	0.6957
1000	0.321	218	333	293	0.7025
2000	0.641	437	767	354	0.7500
3000	0.96	655	1637	520	0.7822
4000	1.28	873	1832	761	0.8050
5000	1.60	1092	2525	1025	0.8238
6000	1.92	1310	3442	1363	0.8390
7000	2.24	1528	3526	1249	0.8514
8000	2.56	1747	6133	1228	0.8625
9000	2.89	1965	8928	1492	0.8706
10000	3.21	2183	8912	2678	0.8793

4.4.2   Test Problem B

Problem B is setup as follows: 2D geometric domains varying between 10 nm and 10 μm, with continuous finite element spatial discretizations of 1, 10, 50, and 100 QUAD4 finite elements in the x and y direction, yielding a total element count of 1, 100, 2500, and 10000 equally spaced cells per mesh, respectively. The angular quadratures were varied between S_4, S_8, and S_{16} discrete ordinates, which involve 12, 40, and 144 angular ordinates respectively. All four phonon groups were used in this simulation. The iterative convergence criteria is $\varepsilon = 10^{-6}$, with a temperature difference imposed by boundary temperatures of $T_L = 301$K and $T_R = 300$K. Scalar flux and equilibrium radiance in each group are initialized to 1. The goal of this effort to to understand the performance of the method as the spatial mesh cells change size, angular discretization varies, and the mean free path of the phonons per cell changes between all the groups. We also have broader coupling in this problem, which should help characterize performance against the two-group problem. Table 4.3 shows overall acoustic thickness of the problem for each group, for each domain size. As size increase, the problem becomes more acoustically thick and requires more iterations to converge. The MSI algorithm outperforms SI for a the four group problem, requires less iterations and less CPU time to converge. MSI has the most benefit at larger acoustic thicknesses, but performs consistently against SI when the problems are acoustically thin, as well.

Overall, the iterative performance of the MSI method is better than traditional SI for the four-group problem, with CPU times and iterations for all domain sizes and all three angular discretizations shown in Figs. 4.10 – 4.15. This is due to the inter-group coupling, where ballistic phonons feel the effects of diffuse phonons, and conversely diffuse phonons get encouraged by ballistic phonons. This result follows

similar trends from the two-group problem.

The total average heat flux (Figs. 4.16 – 4.18) and the per-group average heat fluxes (Figs. 4.19 – 4.30) are in general, slightly higher in MSI than in SI, but this behavior is expected as MSI simulates more realistic physics; because of coupling and feedback, heat fluxes in each group are influenced by every other group. In SI there is no coupling whatsoever, and the data in each group are the same for SI as in MSI; SI converges slower and does not represent phonon transport physics as well as MSI.
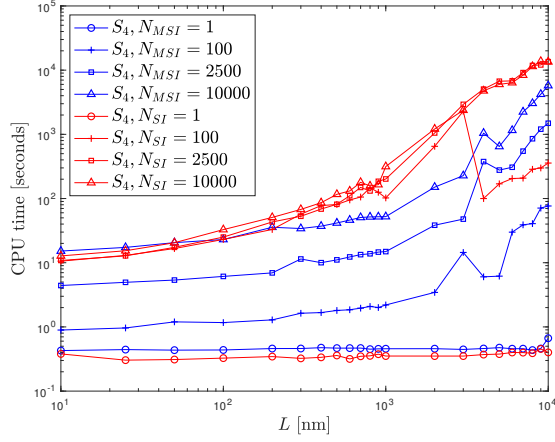
Figure 4.10: CPU time versus domain size for all S_4 cases.
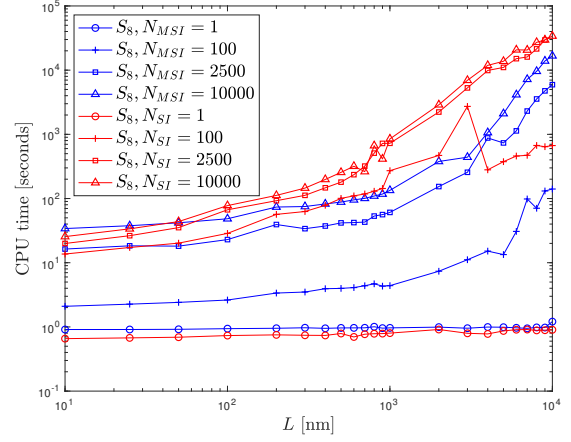
Figure 4.11: CPU time versus domain size for all S_8 cases.
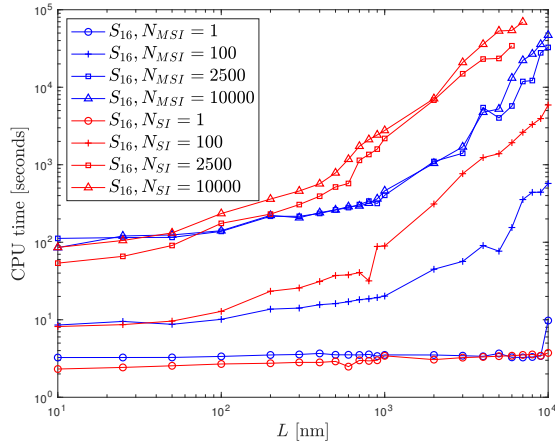
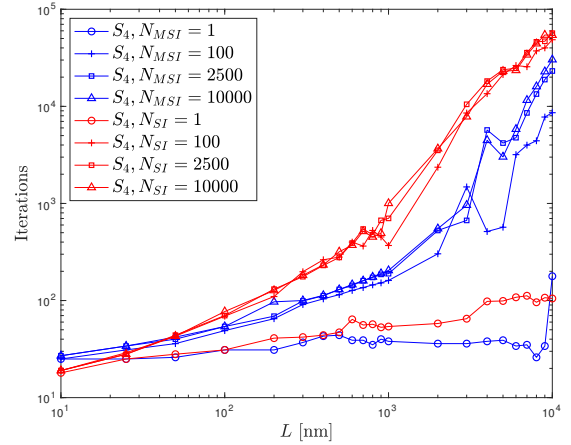Figure 4.12: CPU time versus domain size for all S_{16} cases.

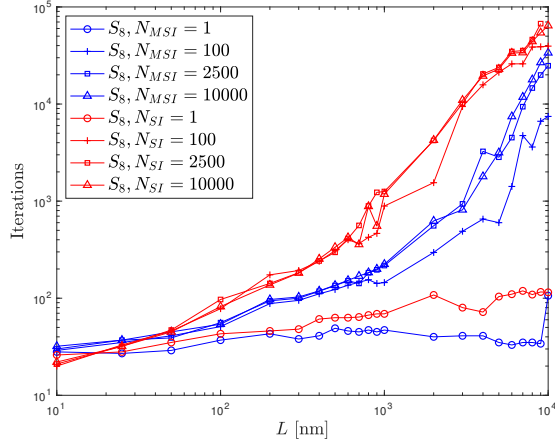Figure 4.13: Iterations versus domain size for all S_4 cases.

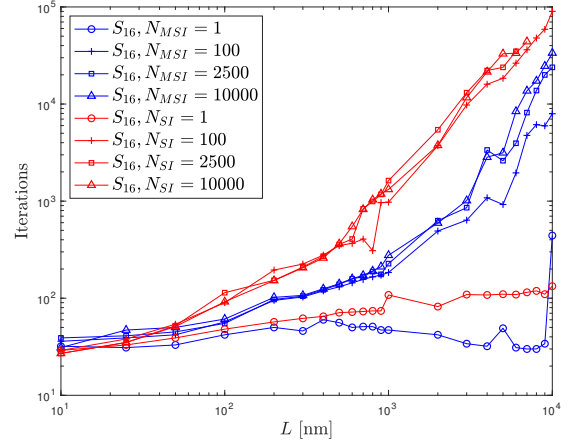Figure 4.14: Iterations versus domain size for all S_8 cases.

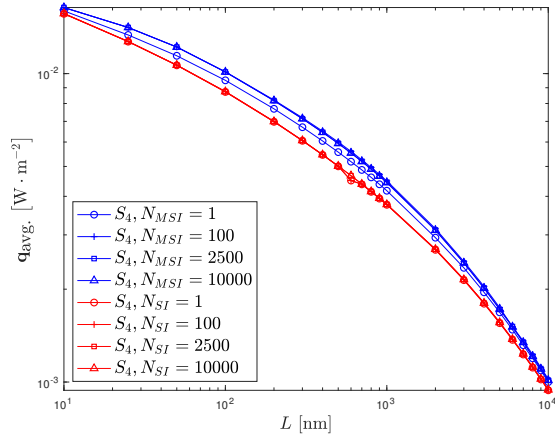Figure 4.15: Iterations versus domain size for all S_{16} cases.

Figure 4.16: Average total heat flux versus domain size for S_4 case.
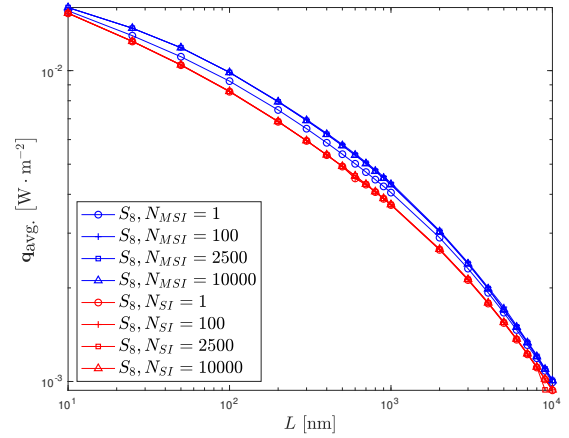
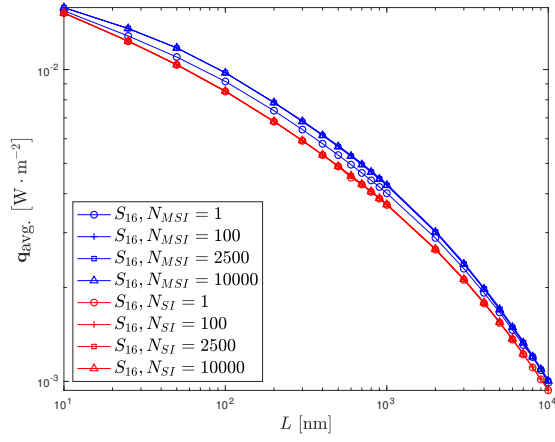Figure 4.17: Average total heat flux versus domain size for S_8 case.

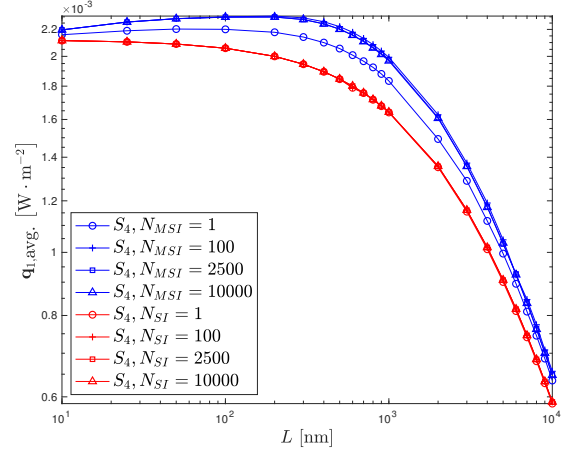Figure 4.18: Average total heat flux versus domain size for S_{16} case.

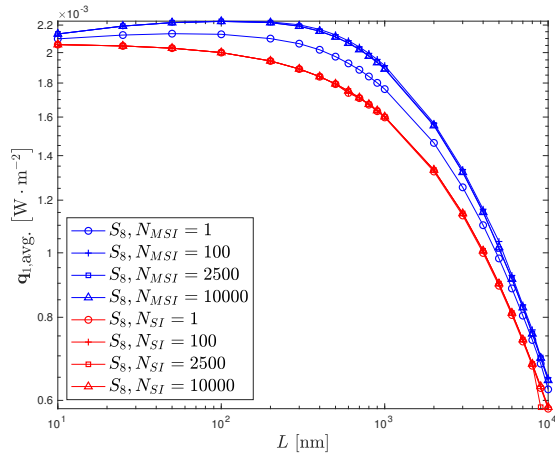Figure 4.19: Average heat flux in group 1 versus domain size for S_4 case.

Figure 4.20: Average heat flux in group 1 versus domain size for S_8 case.

Figure 4.21: Average heat flux in group 1 versus domain size for S_{16} case.

Figure 4.22: Average heat flux in group 2 versus domain size for S_4 case.

Figure 4.23: Average heat flux in group 2 versus domain size for S_8 case.

Figure 4.24: Average heat flux in group 2 versus domain size for S_{16} case.

Figure 4.25: Average heat flux in group 3 versus domain size for S_4 case.

Figure 4.26: Average heat flux in group 3 versus domain size for S_8 case.

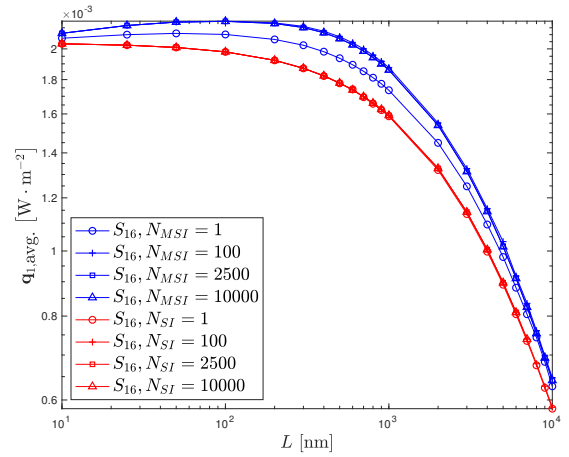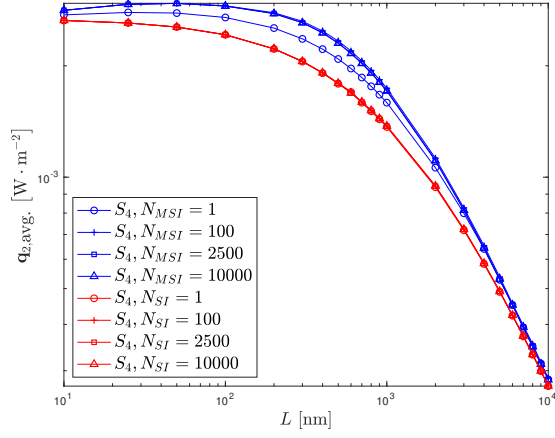Figure 4.27: Average heat flux in group 3 versus domain size for S_{16} case.
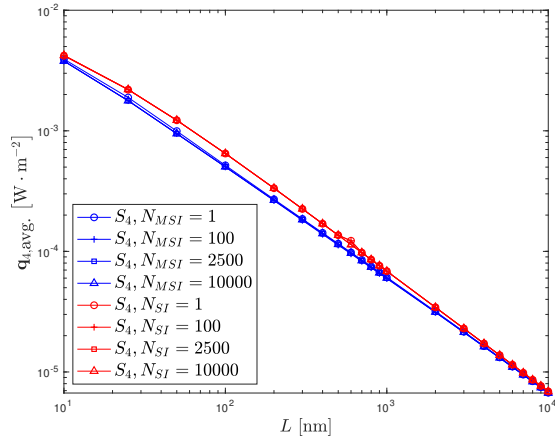
Figure 4.28: Average heat flux in group 4 versus domain size for S_4 case.

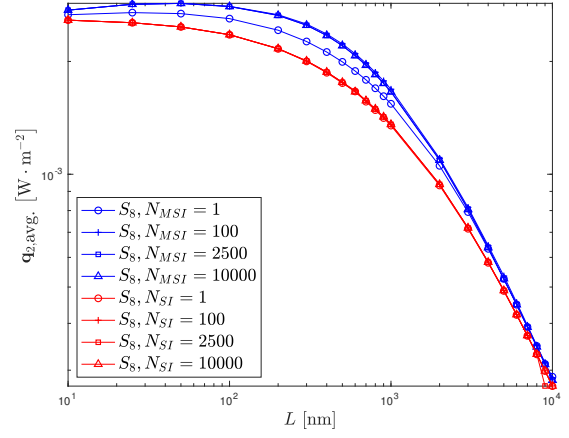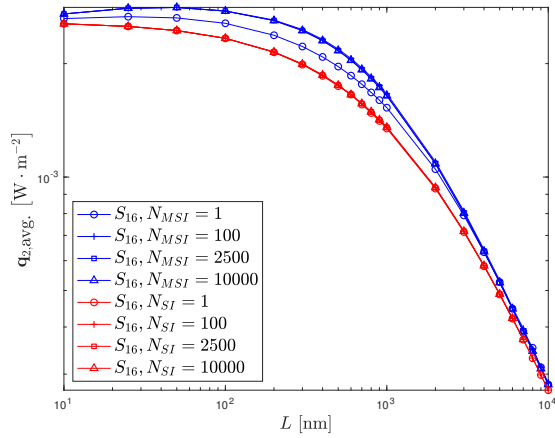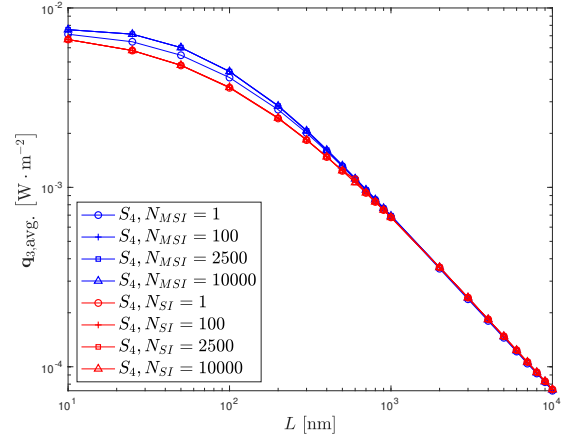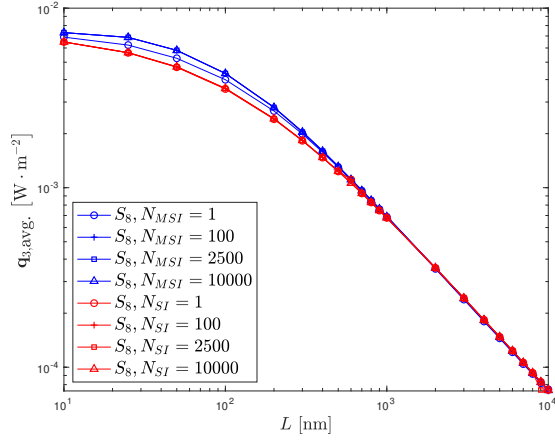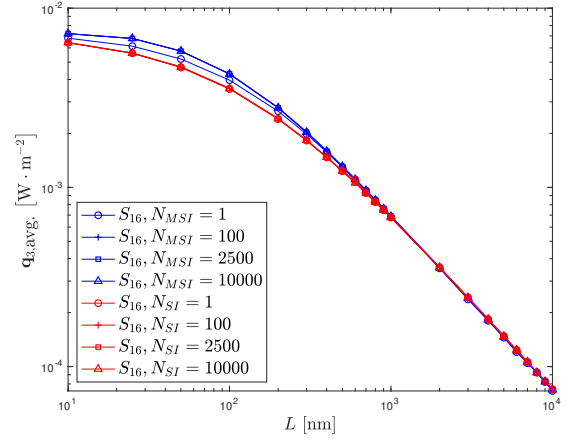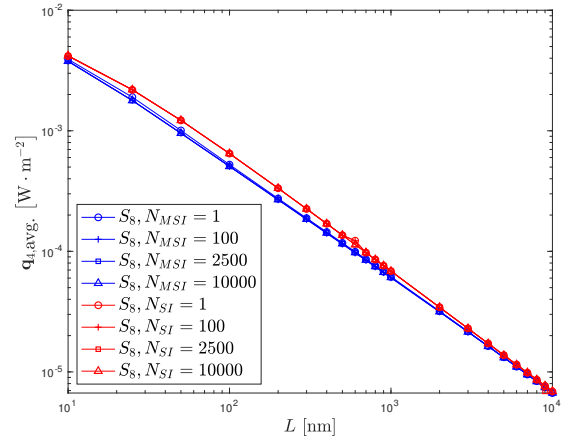Figure 4.29: Average heat flux in group 4 versus domain size for S_8 case.
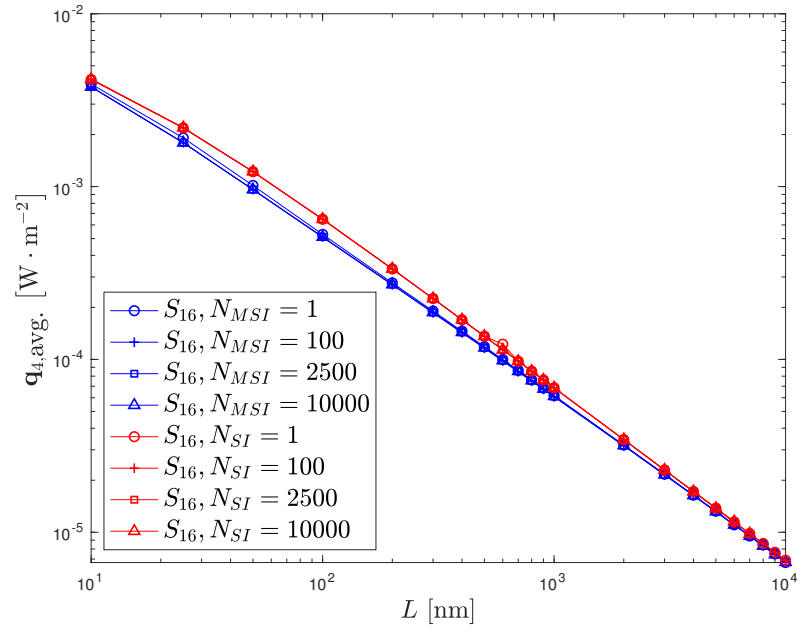
Figure 4.30: Average heat flux in group 4 versus domain size for S_{16} case.

Table 4.3: 4-group: ζ_g and iterations for SI and MSI. Case: S_8, $N = 10000$

L [nm]	ξ_1	ξ_2	ξ_3	ξ_4	Its$_{\text{SI}}$	Its$_{\text{MSI}}$
10	0.0032	0.011	0.13	2.2	22	32
25	0.008	0.028	0.31	5.5	32	37
50	0.016	0.056	0.63	11	45	45
100	0.032	0.111	1.26	22	82	54
200	0.064	0.222	2.5	44	137	97
300	0.096	0.334	3.77	66	182	103
400	0.128	0.445	5.03	87	254	119
500	0.16	0.556	6.29	109	335	136
600	0.192	0.668	7.54	131	422	153
700	0.224	0.78	8.8	153	358	169
800	0.256	0.89	10	175	883	184
900	0.289	1.002	11	197	554	200
1000	0.321	1.11	13	218	1181	224
2000	0.64	2.22	25	437	4250	625
3000	0.96	3.34	38	655	10968	814
4000	1.28	4.5	50	873	19466	1793
5000	1.6	5.6	63	1092	22917	3161
6000	1.92	6.7	75	1310	33507	7443
7000	2.24	7.8	88	1528	33874	11805
8000	2.56	8.9	101	1747	44133	17852
9000	2.89	10	113	1965	54256	26799
10000	3.21	11	126	2183	64213	33732

4.5 Conclusions

We have compared the performance of traditional SI applied to an uncoupled spectral phonon transport solver to the new, coupled MSI method, and found the iterative performance of MSI to be superior. MSI converges more rapidly than SI in acoustically thick domains, for all cases. The coupling introduced by MSI not only allows the system of equations to converge faster, the coupling between phonon groups better models the physics of phonon transport. Problems involving acoustically thick materials still suffer from slow iterative convergence, and acceleration techniques may be valuable to achieve greater efficiency.

4.6 Acknowledgments

5   Conclusions

In this research, we investigated deterministic phonon transport in real media. We developed and implemented the diffuse mismatch model in 3D geometries for capturing the physics of phonon interfacial transport, in a thermal conductivity simulation for UO_2 bulk with Xe impurities. We developed a fully coupled method for simulating spectral thermal transport in real media, using a coupled temperature to generate equilibrium phonon distributions, and derived a new closure term for the BTE to conserve energy. We performed convergence studies to test the efficiency of the new method, and compared against the uncoupled SAAF method. We discuss the conclusions for each of these separately in the following sections. We discuss some future work in Sec. 5.4.

5.1   Interface Physics

Interfacial physics effects in phonon transport is still an open research topic. There is much that is unknown about the true physical effects which phonons experience as they scatter from one material into another [108]. The DMM we implemented in a 3D general geometry, and used in a heterogeneous, one group simulation of Xe bubbles in UO_2 confirmed that the presence of Xe degrades thermal conductivity of UO_2 by approximately a factor of 4 [117]. Though we followed the trends of Du *et al.*, we did not exactly match their results [3]. However, this is acceptable in the sense that there is not a unified, accepted model for resolving interfacial scattering physics.

We found that the presence of Xe bubbles decreases local heat flux by providing additional geometric scattering centers – the two phenomena are inversely proportional. As phonon scattering increases, heat flux decreases, especially in the

vicinity of the bubble. While generating material properties of Xe, we found that Xe undergoes a phase change at a temperature threshold when held at a pressure of 3 GPa. This is consistent with other simulations in the literature; however, it is difficult to experimentally predict or observe this phenomenon in Xe contained with UO_2, as other researchers have commented on this as well [44–46].

5.2   Spectral Phonon Transport

We developed a new method for simulating deterministic, spectral phonon transport to predict heat flux, thermal conductivity, and temperature distributions in dielectric and insulating materials [140]. This method is unique in that all the spectral phonon groups are coupled through a local average material temperature, and a new term, β, was derived to conserve the fraction of total phonon energy lost in the exchange between the transport and equilibrium systems. This method predicts thermal conductivity trends in materials spanning geometric domain sizes from nanometer to micrometer, and exhibits the correct asymptotic behavior in heat flux as domain size increases.

We observed β to be the most influential at smaller domain sizes, where equilibrium is difficult to establish due to the proximity of the boundary phonon sources; as domain size increased, β reduced in size, and nearly vanished at the maximum domain size of 10 μm. This further makes the case to perform BTE simulations for nano- to micro-meter heat transfer, as the Fourier law will not accurately capture the heat transfer in such small domain sizes, e.g., thermoelectric devices, heat transfer around defects and heterogeneities in reactor fuel.

As domain size increases, the regimes of phonon scattering shift from a mixture of ballistic and agnostic scattering events to primarily diffuse, increasing the acoustic

thickness of the simulation. In turn, these problems converge slower. The coupling between the groups distributes effects from the ballistic and diffuse carriers into every group, and so ballistic phonons are throttled by the presence of diffuse phonons. Conversely, diffuse phonons are "encouraged" (positively interfere) by the presence of ballistic phonons, and these groups have their convergence properties improved somewhat.

5.3   Convergence Study

From our convergence studies, we found that the new method, a modified source iteration (MSI) with coupling and feedback, is more efficient than traditional, uncoupled source iteration (SI). For both a 2- and 4- frequency group problem, we found that required iterations were reduced by a factor of 4 to 10, depending on the spatial, angular, and frequency discretization of the problem. Not only does MSI solve the problem more efficiently, it also yields more physical results due to the coupling of the phonon groups through a local temperature. The uncoupled SI method does not incorporate any coupling, and is less efficient.

5.4   Future Work

The work performed in this dissertation is only a small contribution to the complex, multiphysics challenge of predicting thermal conductivity in on-line nuclear reactors. There are more research areas that could be addressed.

Introducing an uncertainty quantification (UQ) step into the workflow. Every computational simulation needs to include some sort of UQ analysis, because of the many areas in the overall organizational flow of the process that may introduce some uncertainty. Specifically, we would want to analyze at the uncertainty in

the group velocity and phonon lifetimes, as these have the highest impact on the solutions. We performed a UQ analysis for the grey-transport case [56] using a polynomial chaos expansion method, but this was limited to a single mean free path in homogeneous silicon. The number of statistical configurations increases quite drastically with the number of uncertain variables (specifically, Λ). It may be possible to leverage RAVEN [142] (an uncertainty quantification code in the MOOSE framework) to perform this task.

Coupling phonon transport to phase field simulations would take us away from creating static meshes to simulate our physical domain. Through the use of microstructural evolution simulations, we could create a seed cell of UO_2 in which we could simulate fission to model the nucleation and migration of xenon bubbles. This could be done by coupling to MARMOT, another code in the MOOSE family [28]. Because the Xe bubbles would no longer be static (as we have approached this in previous work), we could see how conductivity might change locally in an operational cycle of a reactor. As we hope to expand our simulation domain to fuel pins, we could couple the temperature gradients generated from phonon transport to neutron transport simulations in Rattlesnake to include temperature feedback in neutron cross sections. This may be challenging to implement, as the timescales of nucleation and material diffusion are many orders of magnitude larger than phonon scattering events.

Developing a transient scheme which uses a first law balance relation to the internal energy, and so naturally includes a temperature dependence due to a decaying heat flux. This will change how we approach the problem and force us to solve time dependent equations. This could be useful in the modeling and simulation of certain types of experiment, such as Time Domain Thermoreflectance

(TDTR), used to measure thermal conductivity by heating a sample and measuring the change in the reflectance at a surface over time, which could predict thermal properties [111].

Nano- and micro-scale thermal transport are a critical area of study. Modern computational infrastructures possess the resources to run these detailed simulations to try and predict and understand the underlying physics which govern heat transport at such small length scales. It is clear that relying on Fourier's law for mesoscale heat transfer fails to account for the wealth of detail hidden in microstructure of materials. By developing methods to simulate microscale heat transport, specifically to determine thermal conductivity and temperature distributions in real materials with defects, we may be able to increase our understanding, and the safety, of nuclear fuels and reactors.

BIBLIOGRAPHY

[1] B. YILBAS and S. BIN MANSOOR, "Phonon Transport in Two-Dimensional Silicon Thin Film: Influence of Film Width and Boundary Conditions on Temperature Distribution," *European Physical Journal B*, **85** (2012).

[2] J. BATES, *HIGH-TEMPERATURE THERMAL CONDUCTIVITY OF ROUND ROBIN URANIUM DIOXIDE.*, OSTI (Jan 1970).

[3] S. DU ET AL., "A molecular dynamics study of anisotropy and the effect of Xe on UO_2 thermal conductivity," Tech. rep., Los Alamos National Laboratory (2011).

[4] J. DUDERSTADT and L. HAMILTON, *Nuclear Reactor Analysis*, John Wiley & Sons, 1st ed. (1976).

[5] J. LAMARSH, *Introduction to Nuclear Reactor Theory*, Addison-Wesley (1983).

[6] N. TODREAS and M. KAZIMI, *Nuclear Systems*, vol. 1, CRC Press (2012).

[7] D. D. FRANK INCROPERA ET AL., *Introduction to Heat Transfer*, John Wiley & Sons, Inc., 5th ed. (2007).

[8] J. B. ET AL., "Thermal Conductivity of Uranium Dioxide," Tech. rep., International Atomic Energy Agency (1966).

[9] P. M. ET AL., "Thermophysical properties database of materials for light water reactors and heavy water reactors," Tech. rep., International Atomic Energy Agency (2005).

[10] S. POPOV, J. CARBAJO, V. IVANOV, and G. YODER, "Thermophysical Properties of MOX and UO$_2$ Fuels Including the Effects of Irradiation," Tech. rep., Oak Ridge National Laboratory (2000).

[11] J. ZIMAN, *Electrons and Phonons: The Theory of Transport Phenomena in Solids*, Oxford University Press (2001).

[12] C. KITTEL, *Introduction to Solid State Physics*, John Wiley & Sons, 8th ed. (2005).

[13] G. SRIVASTAVA, *The Physics of Phonons*, Taylor & Francis Group, 1st ed. (1990).

[14] N. W. ASHCROFT and N. D. MERMIN, *Solid State Physics*, Mystery, 1st ed. (1976).

[15] V. TENNERY, "Review of Thermal Conductivity and Heat Transfer in Uranium Dioxide," Tech. rep., Oak Ridge National Laboratory (1959).

[16] M. AMAYA, T. KUBO, and Y. KOREI, "Thermal Conductivity Measurements on UO$_{2+x}$ from 300 to 1,400 K," *Journal of Nuclear Science and Technology*, **33** (1996).

[17] A. MAJUMDAR, "Microscale Heat Conduction in Dielectric Thin Films," *Journal of Heat Transfer*, **115**, 7–16 (1993).

[18] M. DUSIC, "Safety margins of operating reactors: Analysis of uncertainties and implications for decision making," Tech. rep., International Atomic Energy Agency (2003).

[19] L. DRESNER, *Resonance absorption of neutrons in nuclear reactors*, Ph.D. thesis, University of Arizona (1959).

[20] "Sigma: ENDF Retrieval & Plotting," http://www.nndc.bnl.gov/sigma/ (2016).

[21] P. SHARMA and M. F. ROSE, "Three-Phonon Scattering Processes and Their Role in Phonon Thermal Conductivity of Silicon," *Journal of Solid State Chemistry*, **73**, 92–97 (1988).

[22] Y. JOSHI and D. SINGH, "Thermal Resistivity due to Three-Phonon Normal Processes," *Physica*, **81** (1975).

[23] H. CATALDO, E. HERNANDEZ, and C. DORSO, "Dynamical Aspects of Phonon-phonon Coupling in Collective Mode Damping," *Physica*, **142** (1987).

[24] T. FENG and X. RUAN, "Quantum mechanical prediction of four-phonon scattering rates and reduced thermal conductivity of solids," *Physical Review B*, **93** (2016).

[25] X. M. BAI, M. R. TONKS, Y. ZHANG, and J. D. HALES, "Multiscale Modeling of Thermal Conductivity of High Burnup Structures in UO_2 Fuels," *Journal of Nuclear Materials*, **470**, 208–215 (2016).

[26] B. SCHMIDT, R. CARLSON, and L. BLYUDAYA, "NEAMS: The Nuclear Energy Advanced Modeling and Simulation Program," Tech. rep., Argonne National Laboratory (2013).

[27] B. SCHMIDT, R. CARLSON, and L. BLYUDAYA, "NEAMS Update: Quarterly report for April-June 2013," Tech. rep., Argonne National Laboratory (2013).

[28] D. SCHWEN, P. CHAKRABORTY, L. K. AAGESEN, Y. ZHANG, K. AHMED, D. A. ANDERSSON, and C. MATTHEWS, "Assessment of

marmot release 1.1: A mesoscale fuel performance code," Tech. rep., Idaho National Laboratory (2016).

[29] J. H. ET. AL, "BISON Users Manual," Tech. rep., Idaho National Laboratory (2016).

[30] K. GOFRYK, S. DU, C. STANEK, J. LASHLEY, X.-Y. LIU, R. SCHULZE, J. SMITH, D. SAFARIK, D. BYLER, K. MCCLELLAN, B. UBERUAGA, B. SCOTT, and D. ANDERSSON, "Aniosotropic thermal conductivity in uranium dioxide," *Nature Communications* (2014).

[31] L. DE SOUSA OLIVEIRA, "Thermal resistance from irradiation defects in graphite," *Computational Materials Science*, **103** (2015).

[32] S. DU, K. GOFRYK, D. ANDERSSON, X.-Y. LIU, and C. STANEK, "A molecular dynamics study of anisotropy and the effect of Xe on UO_2 thermal conductivity," Tech. rep., Los Alamos National Laboratory (2013).

[33] G. T. M. COLBERT and F.RIBEIRO, "Theoretical study of xenon adsorption in UO_2 nanoporous matrices," *Journal of Physics: Condensed Matter* (2014).

[34] J. OH, Y. KOO, J. CHEON, B. LEE, and D. SOHN, "Molecular dynamics simulation of the pressure-volume-temperature data of xenon for a nuclear fuel," *Journal of Nuclear Materials* (2008).

[35] G. KRESSE and J. HAFNER, "Ab initio molecular dynamics for liquid metals," *Physical Review B*, **47**, 222–229 (1993).

[36] G. KRESSE and J. HAFNER, "Ab initio molecular-dynamic simulation of the liquid-metal-amorphous-semiconductor transition in germanium," *Physical Review B*, **49**, 14251 (1994).

[37] G. KRESSE and J. FURTHMULLER, "Efficiency of ab-initio total energy calculations for metals and semiconductors using a plane-wave basis set," *Computational Materials Science*, **6**, 15–50 (1996).

[38] G. KRESSE and J. FURTHMULLER, "Efficient iterative schemes for ab initio total-energy calculations using a plane-wave basis set," *Physical Review B*, **54**, 11169 (1996).

[39] A. TOGO and I. TANAKA, "First principles phonon calculations in materials science," *Scripta Materialia*, **108**, 1–5 (2015).

[40] A. TOGO, L. CHAPUT, and I. TANAKA, "Distributions of phonon lifetimes in Brillouin zones," *Physical Review B*, **91** (2015).

[41] R. LESAR, *Introduction to Computational Materials Science*, Cambridge University Press (2013).

[42] S. PLIMPTON, "Fast Parallel Algorithms for Short-Range Molecular Dynamics," *Journal of Computational Physics*, **117**, 1–19 (1995).

[43] C. MATTHEWS, *Fission Gas Bubble Behavior in Uranium Carbide*, Ph.D. thesis, Oregon State University (2015).

[44] T. XIAO-FENG, L. CHONG-SHENG, Z. ZHENG-HE, and G. TAO, "Molecular Dynamics simulation of collective behaviour of Xe in UO_2," *Chinese Physics B* (2010).

[45] O. SIFNER and J. KLOMFAR, "Thermodynamic Properties of Xenon from the Triple Point to 800 K with Pressures up to 350 MPa," *Institute of Thermomechanics* (1992).

[46] S. SASAKI, N. WADA, and H. T. KUME, "High-pressure Brillouin study of the elastic properties of rare-gas solid xenon at pressurs up to 45 GPa," *Journal of Raman Spectroscopy* (2009).

[47] E. SWARTZ and R. POHL, "Thermal boundary resistance," *Reviews of Modern Physics*, **61** (1989).

[48] E. LANDRY and A. MCGAUGHEY, "Thermal boundary resistance predictions from molecular dynamics simulations and theoretical calculations," *Physical Review B*, **80** (2009).

[49] K. FILIPPOV and A. BALANDIN, "Thermal Boundary Resistance and Heat Diffusion in AlGaN/GaN HFETs," Tech. rep., University of California - Riverside (2003).

[50] D. SINGH, X. GUO, A. ALEXEENKO, J. Y. MURTHY, and T. S. FISHER, "Modeling of subcontinuum thermal transport across semiconductor-gas interfaces," *Journal of Applied Physics*, **106** (2009).

[51] S. B. MANSOOR and B. YILBAS, "Phonon radiative transfer in silicon-aluminum thin films: Frequency dependent case," *International Journal of Thermal Sciences*, **57**, 54–62 (2012).

[52] S. B. MANSOOR and B. YILBAS, "Phonon transport in silicon-silicon and silicon-diamond thin films: Consideration of thermal boundary resistance at interface," *Physica B*, **406** (2011).

[53] R. YANG and G. CHEN, "Thermal conductivity modeling of periodic two-dimensional nanocomposites," *Physical Review B*, **69** (2004).

[54] A. MINNICH, G. CHEN, S. MANSOOR, and B. YILBAS, "Quasiballistic heat transfer studied using the frequency-dependent Boltzmann transport equation," *Physical Review B*, **84**, 235207 (2011).

[55] J. HARTER, P. A. GREANEY, and T. PALMER, "Characterization of Thermal Conductivity using Deterministic Phonon Transport in Rattlesnake," *Transactions of the American Nuclear Society*, **112**, 829–832 (2015).

[56] J. HARTER, P. A. GREANEY, and T. PALMER, "Quantifying the Uncertainty in Deterministic Phonon Transport Calculations of Thermal Conductivity using Polynomial Chaos Expansions," *Transactions of the American Nuclear Society*, **115**, 611–614 (2016).

[57] P. ALLU and S. MAZUMDER, "Hybrid ballistic-diffusive solution to the frequency-dependent phonon Boltzmann Transport Equation," *International Journal of Heat and Mass Transfer*, **100**, 165–177 (2016).

[58] C. HUA and A. J. MINNICH, "Semi-analytical solution to the frequency-dependent Boltzmann transport equation for cross-plane heat conduction in thin films," *Journal of Applied Physics*, **117**, 175306 (2015).

[59] P. ALLU, *A Hybrid Ballistic-Diffusive Method to Solve the Frequency Dependent Boltzmann Transport Equation*, Master's thesis, Ohio State University (2016).

[60] S. MAZUMDER and A. MAJUMDAR, "Monte Carlo Study of Phonon Transport in Solid Thin Films Including Dispersion and Polarization," *Journal of Heat Transfer*, **123**, 749–759 (2001).

[61] C. ZHANG, Z. GUO, and S. CHEN, "An implicit kinetic scheme for multiscale heat transfer problem accounting for phonon dispersion and polarization," *International Journal of Heat and Mass Transfer*, **130**, 1366–1376 (2019).

[62] A. MCGAUGHEY and A. JAIN, "Nanostructure thermal conductivity prediction by Monte Carlo sampling of phonon free paths," *Journal of Applied Physics*, **100** (2012).

[63] A. CHERNATYNSKIY and S. R. PHILLPOT, "Phonon Transport Simulator (PhonTS)," *Computer Physics Communications*, **192** (2015).

[64] W. LI, J. CARRETE, N. A. KATCHO, and N. MINGO, "ShengBTE: A solver of the Boltzmann transport equation for phonons," *Computer Physics Communications*, **185** (2014).

[65] J. DUDERSTADT and W. MARTIN, *Transport Theory*, John Wiley & Sons, Inc. (1979).

[66] Y. WANG, H. ZHANG, and R. MARTINEAU, "Diffusion Acceleration Schemes for Self-Adjoint Angular Flux Formulation with a Void Treatment," *Nuclear Science and Engineering*, **176** (2014).

[67] Y. WANG, "Nonlinear Diffusion Acceleration for the Multigroup Transport Equation Discretized with S_N and Continuous FEM with Rattlesnake," in "Proceedings to the International Conference on Mathematics, Computational Methods & Reactor Physics (M&C 2013)," (2013).

[68] J. HARTER, *Predicting Thermal Conductivity in Nuclear Fuels using Rattlesnake-Based Deterministic Phonon Transport Simulations*, Master's thesis, Oregon State University (2015).

[69] J. MOREL and J. MCGHEE, "A Self-Adjoint Angular Flux Formulation," *Nuclear Science and Engineering*, **3**, 312–325 (1999).

[70] D. GASTON ET AL., "MOOSE: A Parallel Computational Framework for Coupled Systems of Nonlinear Equations," *Nuclear Engineering and Design*, **239**, 1768–1778 (2009).

[71] Y. SAAD and M. SCHULTZ, "GMRES: A Generalized Minimal Residual Algorithm for Solving Nonsymmetric Linear Systems," *SIAM Journal of Scientific Computing*, **7**, 856–869 (1986).

[72] J. MOREL, B. T. ADAMS, T. NOH, J. MCGHEE, T. EVANS, and T. UR-BATSCH, "Spatial discretizations for self-adjoint forms of the radiative transfer equations," *Journal of Computational Physics*, **214**, 12–40 (2006).

[73] Y. WANG, S. SCHUNERT, B. A. BAKER, and V. LABOURE, *Rattlesnake User Manual*, Idaho National Laboratory, 2525 Fremont Ave., Idaho Falls, ID 83402 (2019).

[74] E. LEWIS and W. MILLER, *Computational Methods of Neutron Transport*, Wiley-Interscience (1993).

[75] E. LARSEN, "Unconditionally Stable Diffusion-Synthetic Acceleration Methods for the Slab Geometry Discrete Ordinates Equations. Part I: Theory," *Nuclear Science and Engineering*, **82**, 47–63 (1982).

[76] ASME, *Non-gray Phonon Transport using a Hybrid BTE-Fourier Solver* (2009).

[77] J. LOY, *An acceleration technique for the solution of the phonon Boltzmann transport equation*, Master's thesis, Purdue University (2010).

[78] C. ZHANG, S. CHEN, Z. GUO, and L. WU, "A fast synthetic iterative scheme for the stationary phonon Boltzmann transport equation," *arXiv e-prints*, arXiv:1812.06405 (Dec 2019).

[79] J. DUDERSTADT and L. HAMILTON, *Nuclear Reactor Analysis*, Wiley (1976).

[80] M. MEYER ET AL., "Irradiation Performance of U-Mo Monolithic Fuel," *Nuclear Engineering and Technology*, **46**, *2* (2014).

[81] B. SZPUNAR and J. SZPUNAR, "Thermal Conductivity of Uranium Nitride and Carbide," *International Journal of Nuclear Energy*, **2014** (September 2014).

[82] J. MOREL and J. MCGHEE, "A Self-Adjoint Angular Flux Equation," *Nuclear Science and Engineering*, **3**, *12* (1999).

[83] Y. WANG, "Nonlinear Diffusion Acceleration for the Multigroup Transport Equation Discretized with S_N and Continuous FEM with Rattlesnake," in "Proceedings to the International Conference on Mathematics, Computational Methods & Reactor Physics (M&C 2013)," Sun Valley, Idaho (May 2013).

[84] J. HARTER, P. A. GREANEY, and T. PALMER, "Characterization of Thermal Conductivity using Deterministic Phonon Transport in Rattlesnake," *Transactions of the American Nuclear Society*, **112** (2015).

[85] A. MAJUMDAR, "Microscale heat conduction in dielectric thin films," *Journal of Heat Transfer*, **115** (1993).

[86] D. KNOLL and D. KEYES, "Jacobian-free Newton-Kryloc methods: a survey

of approaches and applications," *Journal of Computational Physics*, **193** (2004).

[87] P. ALLU and S. MAZUMDER, "Hybrid ballistic-diffusive solution to the frequency dependent phonon Boltzmann Transport Equation," *International Journal of Heat and Mass Transfer*, **100** (2016).

[88] W. LI ET AL., "ShengBTE: A solver of the Boltzmann transport equation for phonons," *Computer Physics Communications*, **185**, *6* (2014).

[89] L. DE SOUSA OLIVEIRA, "Thermal resistance from irradiation defects in graphite," *Computational Materials Science*, **103** (2015).

[90] A. CHERNATYNSKIY and S. R. PHILLPOT, "Phonon Transport Simulator (PhonTS)," *Computer Physics Communications*, **192** (2015).

[91] R. MORRIS, *CUBIT 14.1 User Documentation*, Sandia National Laboratory (2015).

[92] Y. SAAD and M. SCHULTZ, "GMRES: A Generalized Minimal Residual Algorithm for Solving Nonsymmetric Linear Systems," *SIAM Journal of Scientific Computing*, **7** (1986).

[93] Y. SAAD, *Iterative Methods for Sparse Linear Systems*, Society for Industrial and Applied Mathematics, 2nd ed. (2003).

[94] T. XIAO-FENG, L. CHONG-SHENG, Z. ZHENG-HE, and G. TAO, "Molecular Dynamics simulation of collective behaviour of Xe in UO_2," *Chinese Physics B*, **19**, *5* (2010).

[95] M. COLBERT, G. TRÉGLIA, and F. RIBEIRO, "Theoretical study of xenon adsorption in UO_2 nanoporous matrices," *Journal of Physics: Condensed Matter*, **26**, *48* (2014).

[96] S. SASAKI, N. WADA, and H. T. KUME, "High-pressure Brillouin study of the elastic properties of rare-gas solid xenon at pressures up to 45 GPa," *Journal of Raman Spectroscopy*, **40**, *2009* (2008).

[97] A. TOGO, F. OBA, and I. TANAKA, "First-principles calculations of the ferroelastic transition between rutile-type and CaCl 2-type SiO 2 at high pressures," *Physical Review B*, **78**, *13*, 134106 (2008).

[98] G. KRESSE and J. HAFNER, "Ab initio molecular-dynamics simulation of the liquid-metal–amorphous-semiconductor transition in germanium," *Physical Review B*, **49**, *20*, 14251 (1994).

[99] G. KRESSE and J. FURTHMÜLLER, "Efficiency of ab-initio total energy calculations for metals and semiconductors using a plane-wave basis set," *Computational Materials Science*, **6**, *1*, 15–50 (1996).

[100] G. KRESSE and J. FURTHMÜLLER, "Efficient iterative schemes for ab initio total-energy calculations using a plane-wave basis set," *Physical Review B*, **54**, *16*, 11169 (1996).

[101] J. P. PERDEW and A. ZUNGER, "Self-interaction correction to density-functional approximations for many-electron systems," *Physical Review B*, **23**, *10*, 5048 (1981).

[102] B.-T. WANG, P. ZHANG, R. LIZÁRRAGA, I. DI MARCO, and O. ERIKSSON, "Phonon spectrum, thermodynamic properties, and pressure-

temperature phase diagram of uranium dioxide," *Physical Review B*, **88**, *10*, 104107 (2013).

[103] S. PLIMPTON, "Fast Parallel Algorithms for Short-Range Molecular Dynamics," *Journal of Computational Physics*, **117** (1995).

[104] R. KUBO, M. YOKOTA, and S. NAKAJIMA, "Statistical-Mechanical Theory of Irreversible Processes. II. Response to Thermal Disturbance," *Journal of the Physical Society of Japan*, **12**, *11*, 1203–1211 (1957).

[105] P. LINSTROM and W. MALLARD, *NIST Chemistry WebBook, NIST Standard Reference Database Number 69*, National Institute of Standards and Technology (2017).

[106] S. B. MANSOOR and B. YILBAS, "Phonon radiative transport in silicon-aliuminum thin films: frequency dependent case," *International Journal of Thermal Sciences*, **57** (2012).

[107] S. B. MANSOOR and B. YILBAS, "Phonon transport in silicon-silicon and silicon-diamond thin films: Consideration of thermal boundary resistance at interface," *Physica B*, **406**, *11* (2011).

[108] E. SWARTZ and R. POHL, "Thermal boundary resistance," *Reviews of Modern Physics*, **61**, *3* (1989).

[109] I. THOMAS and G. SRIVASTAVA, "Theory of interface and anharmonic phonon interactions in nanocomposite materials," in "IOP Conf. Series: Materials Science and Engineering," (2014).

[110] M. COOPER, C. STANEK, and D. ANDERSSON, "Simulations of thermal conductivity reduction due to extended Xe-vacancy clusters and defining

requirements for modeling spin-phonon scattering," Tech. rep., Los Alamos National Laboratory (2017).

[111] A. MINNICH, "Advances in the measurement and computation of thermal phonon transport properties," *Journal of Physics: Condensed Matter*, **27** (2015).

[112] T. FENG and X. RUAN, "Prediction of Spectral Phonon Mean Free Path and Thermal Conductivity with Applications to Thermoelectrics and Thermal Management: A Review," *Journal of Nanomaterials*, **2014**, 206370–1–25 (2014).

[113] J. CARRETE, B. VERMEERSCH, A. KATRE, A. VAN ROEKEGHEM, T. WANG, G. K. MADSEN, and N. MINGO, "AlmaBTE: A solver of the space–time dependent Boltzmann transport equation for phonons in structured materials," *Computer Physics Communications*, **220**, 351–362 (2017).

[114] W. LI, J. CARRETE, N. A. KATCHO, and N. MINGO, "ShengBTE: a solver of the Boltzmann transport equation for phonons," *Comp. Phys. Commun.*, **185**, 1747–1758 (2014).

[115] G. ROMANO and A. M. KOLPAK, "Diffusive Phonons in Nongray Nanostructures," *Journal of Heat Transfer*, **141** (2017).

[116] G. ROMANO and J. GROSSMAN, "Heat Conduction in Nanostructured Materials Predicted by Phonon Bulk Mean Free Path Distribution," *Journal of Heat Transfer*, **137** (2015).

[117] J. HARTER, L. DE SOUSA OLIVEIRA, A. TRUZSKOWSKA, T. PALMER, and P. A. GREANEY, "Deterministic Phonon Transport Prediction of Ther-

mal Conductivity in Uranium Dioxide With Xenon Impurities," *Journal of Heat Transfer*, **140**, *5*, 051301 (2018).

[118] M. P. ADAMS, M. L. ADAMS, W. D. HAWKINS, T. SMITH, L. RAUCHW-ERGER, N. M. AMATO, T. S. BAILEY, R. D. FALGOUT, A. KUNEN, and P. BROWN, "Provably Optimal Parallel Transport Sweeps on Semi-Structured Grids," *arXiv e-prints*, arXiv:1906.02950 (Jun 2019).

[119] M. ADAMS and E. LARSEN, "Fast Iterative Methods for Discrete-Ordinates Particle Transport Calculations," *Progress in Nuclear Energy*, **40**, 3–159 (2002).

[120] E. LARSEN, "A Grey Transport Acceleration Method for Time-Dependent Radiative Transfer Problems," *Journal of Computational Physics*, **78**, 459–480 (1987).

[121] V. E. HENSON and U. M. YANG, "BoomerAMG: A parallel algebraic multigrid solver and preconditioner," *Applied Numerical Mathematics*, **41**, 155–177 (2002).

[122] Y. SAAD, *Iterative Methods for Sparse Linear Systems*, Society for Industrial and Applied Mathematics, 2nd ed. (2003).

[123] J. CHEN, G. ZHANG, and B. LI, "Molecular Dynamics Simulations of Heat Conduction in Nanostructures: Effect of Heat Bath," *Journal of the Physical Society of Japan*, **79**, *7*, 074604 (2010).

[124] D. CHAKRABORTY, S. FOSTER, and N. NEOPHYTOU, "Monte Carlo simulations for phonon transport in silicon nanomaterials," (2019).

[125] D. LEE and H. JOO, "Coarse Mesh Finite Difference Acceleration of Discrete Ordinate Neutron Transport Calculation Employing Discontinuous Finite Element Method," *Nuclear Engineering and Technology*, **46**, 783–796 (2014).

[126] M. WILLATZEN and Z. L. WANG, "Unified treatment of coupled optical and acoustic phonons in piezoelectric cubic materials," *Physical Review B*, **92**, 224101 (2015).

[127] E. STOCK ET AL., "Acoustic and optical phonon scattering in a single In(Ga)As quantum dot," *Physical Review B*, **83**, 041304(R) (2011).

[128] J.-C. HSU, T.-Y. LU, and T.-R. LIN, "Acousto-optic coupling in phoxonic crystal nanobeam cavities with plasmonic behavior," *Optics Express*, **23**, 25814–25825 (2015).

[129] A. MAJUMDAR, "Effect of Interfacial Roughness on Phonon Radiative Heat Conduction," *Journal of Heat Transfer*, **113**, 797–805 (1991).

[130] I. MIHAI, C. SUCIU, and L. PATULEANU, "Modeling of heat transfer in microchannels of a CPU-heat sink cooling system," in "Advanced Topics in Optoelectronics, Microelectronics, and Nanotechnologies VI," International Society for Optics and Photonics, SPIE (2012), vol. 8411.

[131] M. P. ANANTRAM, M. S. LUNDSTROM, and D. E. NIKONOV, "Modeling of Nanoscale Devices," *arXiv e-prints*, pp. cond–mat/0610247 (Oct 2006).

[132] R. HE, G. SCHIERNING, and K. NIELSCH, "Thermoelectric Devices: A Review of Devices, Architectures, and Contact Optimization," *Advanced Materials Technologies*, **3**, *4*, 1700256 (2018).

[133] K. KUKITA and Y. KAMAKURA, "Monte Carlo simulation of phonon transport in silicon including a realistic dispersion relation," *Journal of Applied Physics*, **114** (2013).

[134] Y. CHEN, D. LI, J. LUKES, and A. MAJUMDAR, "Monte Carlo Simulation of Silicon Nanowire Thermal Conductivity," *Journal of Heat Transfer*, **127** (2005).

[135] V. JEAN, S. FUMERON, K. TERMENTZIDIS, S. TUTASHKONKO, and D. LACROIX, "Monte Carlo simulations of phonon transport in nanoporous silicon and germanium," *Journal of Applied Physics*, **115** (2014).

[136] D. LACROIX, K. JOULIN, and D. LEMMONIER, "Monte Carlo transient phonon transport in silicon and germanium at nanoscales," *Physical Review B*, **72** (2005).

[137] H. ZHANG, C. HUA, D. DING, and A. J. MINNICH, "Length Dependent Thermal Conductivity Measurements Yield Phonon Mean Free Path Spectra in Nanostructures," *Scientific Reports*, **5** (2015).

[138] S. KUMAR, A. MAJUMDAR, and C. TIEN, "The Differential-Discrete-Ordinate Method for Solutions of the Equation of Radiative Transfer," *Journal of Heat Transfer*, **113** (1990).

[139] S. B. MANSOOR and B. YILBAS, "Radiative phonon transport in silicon and collisional energy transfer in aluminum films due to laser short-pulse heating: Influence of laser pulse intensity on temperature distribution," *Optics & Laser Technology*, **44** (2012).

[140] J. R. HARTER, A. HOSSEINI, T. PALMER, and P. A. GREANEY, "Prediction of thermal conductivity in dielectrics using fast, spectrally-resolved phonon transport simulations," *International Journal of Heat and Mass Transfer*, **144**, 118595 (2019).

[141] E. LARSEN, "A Grey Transport Acceleration Method for Time-Dependent Radiative Transfer Problems," *Journal of Computational Physics*, **78**, 459–480 (1988).

[142] C. R. ET AL., "RAVEN Beta 1.0 Release," Tech. rep., Idaho National Laboratory (2016).